Carlos Sánchez Mendoza

Image Processing in Medicine

Advances for Phenotype Characterization, Computer-Assisted Diagnosis and Surgical Planning

Ph.D. Thesis, March 2011

Image Processing in Medicine
Advances for Phenotype Characterization, Computer-Assisted Diagnosis and Surgical Planning

This report was prepared by
Carlos Sánchez Mendoza

Supervisors
Carmen Serrano Gotarredona
Begoña Acha Piñero

Signal Processing and Communications Department
School of Engineering
University of Seville
Camino de los Descubrimientos s/n
41092 Sevilla
Spain

http://departamento.us.es/dtsc/
Tel: (+34) 954 487 291
Fax: (+34) 954 487 341
E-mail: secreteseycoesi.us.es

Release date: March 2011
Comments: This report is part of the requirements to achieve the Ph.D. in Electronics, Signal Processing and Communications at the University of Seville.

Acknowledgments

First of all I would like to express my gratitude to my Thesis supervisors Dr. Acha and Dr. Serrano. Their guidance and support has been capital to the completion of this work.

Dr. Serrano is at the root of my motivation in pursuing a research career, and had she not sparked me with the curiosity for "always being on the tip of the iceberg" I would probably be confined in some boring office job.

Both my supervisors have been not only a scientific, but also an ethical reference in my coming of age as a young researcher. I am sure that, no matter what pathways my life will follow, we will be able to keep alive the wonderful moments we have spent together, both in science and in life.

I would like to thank also our colleagues at Fundación Reina Mercedes. Especially Cristina Suárez and Carlos Parra for whom I hold the greatest respect, and who have honored me with their trust and endless enthusiasm.

To Tomás Gómez Cía, for his excellence and commitment, his never-ending trust and support, I would like to say thank you. I am aware of his efforts and hope to be worthy of his collaboration for the years to come.

I host special feelings of gratitude towards Dr. San José, who has supervised me during my two summer visits to the Applied Chest Imaging Lab, in Brigham and Women's Hospital - Harvard Medical School. Not only has he led me to produce better scientific work but he has also been an inspiring mentor figure and a supporting friend, providing all kinds of advice so necessary for a young disoriented student. To the other members of ACIL who have participated our emphysema study. James Ross, Dr. Díaz and most especially Dr. Washko, who have been supportive, enthusiastic, trusting, inspiring to me during the last two summers. To Katie D'Aco, who has been an optimistic friend in difficult times, thank you and good luck in all your plans for the future. Thank you all for your hard work that has led to the emphysema characterization study presented in this Thesis.

In these acknowledgments, I would also like to thank my supervisors during my summer visit to the Surgical Planning Lab, in Brigham and Women's Hospital - Harvard Medical School. It was such a wonderful opportunity to work under the mentorship of two highly prestigious scientists as brilliant as Dr. Pieper

and Dr. Kikinis. I really appreciated their proximity to a simple first year Ph.D. student like myself, and how diligently they supported and encouraged my learning goals despite their higher responsibilities.

I would like to thank everyone involved in the development of 3DSlicer platform, the paradigm of collaboration in my opinion. All of them, even the ones I have not had the pleasure to meet, own a little part of my work.

To everyone in the department of Signal Processing and Communications, in my University of Seville. Thank you for providing such a nice work environment. Very special thanks to my colleagues in the image processing group. Aurora, light of the morning, the very light of my days in this department. José Antonio, whose optimism and pragmatism have made him my emotional savior so many times. Irene, for her inspiring strength and personality. Francisco (Kiko) for his friendship. Antonio and Nacho for their cheerfulness and their invaluable contributions to the CT segmentation framework presented in this Thesis.

To the Vice-Rectorship of Research of University of Seville, whose funding has been indispensable for every achievement I have made in the last years. Many special thanks to Emilio Leal for his diligence and availability for all management regarding funding for summer interns and permanent position applications.

Finally, I would like to express my gratitude towards my friends (in Seville as in Boston) and family, especially to my father, for their faith, love and emotional care. Thank you for making my issues and difficulties yours. Thank you for sharing my accomplishments too. It is by you that I know my place in the world.

Abstract

In this Thesis we present our contributions to the state-of-the-art in medical image processing, articulating our exposition around the three main roles of medical imaging: disease prevention, diagnosis and treatment.

Disease prevention can sometimes be achieved by proper characterization of disease phenotypes. Such characterization is often attained from the standpoint of imaging. We present our work in characterization of emphysema from high-resolution computed-tomography images via quantification of local texture. We propose to fill the gap between current clinical practice and sophisticated texture approaches by the use of local intensity distributions as an adequate descriptor for the degree of tissue destruction in the emphysematous lung. Interesting results are presented from the analysis of several hundred datasets of lung CT for varying disease severity, suggesting both the correctness of our hypotheses and the pertinence of fine emphysema quantification for understanding of chronic obstructive pulmonary disease.

Medical image processing can also assist in the diagnosis and detection of disease. We introduce our contributions to this field, consisting of segmentation and quantification techniques in application to dermatoscopy images of skin lesions. Segmentation is achieved via a novel active contour algorithm that fully exploits the color content of the images, via cross-bin histogram dissimilarity maximization. Texture quantification in the context of melanocytic lesions is performed using modelization of the pigmentation patterns via Markov random fields, in an effort to embrace the emerging trend in dermatology: malignancy assessment based on texture irregularity analysis. Experimental results for both, the segmentation and quantification proposed techniques, will be validated on a significant set of dermatoscopy images, suggesting interesting pathways towards automatic detection and diagnosis of malignant melanoma.

Once disease has occurred, image processing can assist in therapeutical planning and image-guided intervention. Therapeutical planning, exemplified by virtual reality surgical planning, is tackled by our work in segmentation of bone/fat/muscle in CT images for plastic surgery planning. Using an interactive, incremental approach, our system is able to provide accurate segmentations based on a couple of mouse-clicks for a wide variety of imaging conditions and abnormal anatomies. We present our methodology, and provide profuse experimental validation based on manual segmentations and subjective assessment,

and refer the reader to related work reporting on the clinical benefits obtained using the virtual reality platform hosting our algorithm.

As a conclusion we present a final dissertation on the significance of our results and the probable lines of future work towards fully benefitting healthcare using medical image processing.

Resumen en Español

En esta Tesis presentamos nuestras contribuciones al estado del arte en procesamiento digital de imágenes médicas, articulando nuestra exposición en torno a los tres principales objetivos de la adquisición de imágenes en medicina: la prevención, el diagnóstico y el tratamiento de las enfermedades.

La prevención de la enfermedad se puede conseguir a veces mediante una caracterización cuidadosa de los fenotipos propios de la misma. Tal caracterización a menudo se alcanza a partir de imágenes. Presentamos nuestro trabajo en caracterización del enfisema pulmonar a partir de imágenes TAC (Tomografía Axial Computerizada) de tórax en alta resolución, a través del análisis de las texturas locales de la imagen. Nos proponemos llenar el vacío existente entre la práctica clínica actual, y las sofisticadas pero costosas técnicas de caracterización de regiones texturadas disponibles en la literatura. Lo hacemos utilizando la distribución local de intensidades como un descriptor adecuado para determinar el grado de destrucción de tejido en pulmones enfisematosos. Se presentan interesantes resultados derivados del análisis de varios cientos de imágenes para niveles variables de severidad de la enfermedad, sugiriendo tanto la corrección de nuestras hipótesis, como la pertinencia de este tipo de análisis para la comprensión de la enfermedad pulmonar obstructiva crónica.

El procesado de imágenes médicas también puede asistir en el diagnóstico y detección de enfermedades. Presentamos nuestras contribuciones a este campo, que consisten en técnicas de segmentación y cuantificación de imágenes dermatoscópicas de lesiones de la piel. La segmentación se obtiene mediante un novedoso algoritmo basado en contornos activos que explota al máximo el contenido cromático de las imágenes, gracias a la maximización de la discrepancia mediante comparaciones "cross-bin". La cuantifiación de texturas en lesiones melanocíticas se lleva a cabo utilizando un modelado de los patrones de pigmentación basado en campos aleatorios de Markov, en un esfuerzo por adoptar la tendencia emergente en dermatología: la detección de la malignidad mediante el análisis de la irregularidad de la textura. Los resultados para ambas técnicas son validados con un conjunto significativo de imágenes dermatológicas, sugirirendo líneas interesantes para la detección autoática del melanoma maligno.

Cuando la enfermedad ya está presente, el tratamiento digital de imágenes puede asistir en la planififcación quirúrgica y la intervención guiada por imagen.

La planificación terapeútica, ejemplificada por la planificación de cirugía plástica usando realidad virtual, se aborda en nuestro trabajo en segmentación de hueso/grasa/músculo en imágenes TAC. Usando una abordaje interactivo e incremental, nuestro sistema permite obtener segmentaciones precisas a partir de unos cuantos clics de ratón para una gran variedad de condiciones de adquisición y frente a anatomías anormales. Presentamos nuestra metodología, y presentamos validación experimental profusa basada tanto en segmentaciones manuales como en valoraciones subjetivas de los usuarios, e indicamos referencias al lector que detallan los beneficios obtenidos con el uso de la plataforma de planificación que utiliza nuestro algoritmo.

Como conclusión presentamos una disertación final sobre la importancia de nuestros resultados y las líneas probables de trabajo futuro hacía el objetivo último de mejorar el cuidado de la salud mediante técnicas de tratamiento digital de imágenes médicas.

Contents

List of Figures

List of Tables

Nomenclature

Abbreviations:

CT	X-ray Computed Tomography
COPD	Chronic Obstructive Pulmonary Disease
MRI	Magnetic Resonance Imaging
CAD	Computer-Assisted Detection and Diagnosis
CADe	Computer-Assisted Detection
CADx	Computer-Assisted Diagnosis
PFT	Pulmonary Function Test
HRCT	High Resolution Computed Tomography
HU	Hounsfield Units
NT	Normal Tissue
CL1	Mild Centrilobular Emphysema
CL2	Moderate Centrilobular Emphysema
CL3	Severe Centrilobular Emphysema
PL	Panlobular Emphysema
PS	Paraseptal Emphysema
ROI	Region Of Interest
LBP	Local Binary Pattern
$\mathbf{LBP}^{\mathbf{ri}}$	Rotation Invariant Local Binary Pattern
PDF	Probability Density Function
CDF	Cumulative Distribution Function
EMD	Earth Mover's Distance
kNN	*k*-Nearest Neighbors Classifier
RCA	Relative Class Area
GOLD	Global Initiative on Obstructive Lung Disease severity level
GE	General Electrics
LBPINT	Sørensen's LBP-Intensity Joint Histograms
AB	Adaptive Binning Histograms
KDE	Kernel Density PDF Estimation
LAA%	Percentage of Low Attenuation Area
FEV1%	Forced Expiratory Volume in 1 second (percentage)
GT	Gas Trapping

MDC	Maximal Discrepancy Criterion
I	Inside
O	Outside
CIELAB	International Illumination Consortium $L^*a^*b^*$ color space
H-MDC	Hierarchical MDC
FSCM	Finite-Symmetric Conditional Model
MRF	Markov Random Field
ABCD	Asymmetry, Border irregularity, Color variation, Diameter greater than 6 mm or growing
PCT	Principal Component Transform
ML	Maximum Likelihood
MAP	Maximum A Posteriori
SNR	Signal-to-Noise Rate
Sn	Sensitivity
Sp	Specificity
D	Dice Coefficient
J	Jaccard's Index
TP	True Positive
TN	True Negative
FP	False Positive
FN	False Negative
DIEP	Deep Inferior Epigastric Artery Perforator

Vectors are written with an arrow.

$\bar{f}$	Mean intensity
$\beta_{s,t}$	A FSCM correlation coefficient parameter for location s and displacement t
$\delta(\cdot)$	Kronecker delta function
η_g	A FSCM neighborhood displacement
κ	Contour curvature
μ	Regularizer weight
μ_s	Mean of the FSCM model at a given location s
ω_i	Class label i
$\phi(\cdot,\cdot)$	Level-set function
Σ	Gaussian covariance matrix
σ	Variance of intensity
$\tilde{B}$	Bhattacharyya energy
$\vec{M}$	Gaussian vector of means
$\vec{m}$	Cluster centroid

$\vec{N}$	Normal vector
$\vec{x}$	A spatial set of coordinates in image domain
$\{s\}$	Signature
$A_{I/O}$	Area inside/outside
B	Bhattacharyya distance
$C(t)$	Evolving contour
$C_i(\cdot)$	Charting function for cluster i
$cdf_x(\cdot)$	Cumulative distribution function of pixel values
$D(\cdot,\cdot)$	Minkowski-form distance $\mathscr{L}_1$
d_{uv}	Mass transportation cost from u to v
E	Energy functional
e_s	A Gaussian random variable
F	Force field
$f(\cdot)$	Intensity
f_{uv}	Mass transportation flow from u to v
$G(\cdot)$	A random field
g_s	A random field value at location s
$H(\cdot)$	Heaviside Function
I	Tolerance interval
$K_h(\cdot)$	Kernel function of bandwidth h
k_i	Sensitivity of Z with respect to the weight of cluster i
$N(\cdot)$	Gaussian or Normal density function
O_i	Segmentation output at iteration i
$O_i(\cdot)$	Contrast in iteration i
$p_x(\cdot)$	Probability density function of pixel values
S	Lung mask
$T(\cdot)$	Mapping transformation
w	Cluster weight
Z	Mass transportation work

Chapter 1

Introduction

The influence and impact of digital images on modern society, science, technology and art are tremendous. Image processing has become such a critical component in contemporary science and technology that many tasks would not be attempted without it. It is a truly interdisciplinary subject that draws from synergistic developments involving many disciplines and is used in medical imaging, microscopy, astronomy, computer vision, geology and many other fields.

The rapid and continuing progress in computerized medical image reconstruction, and the associated developments in processing methods have propelled medical imaging into one of the most important sub-fields in scientific imaging. This Thesis describes several contributions to the field of medical image processing.

From the perspective of image processing, our work includes advances in image segmentation and quantification of features extracted from the resulting regions.

Image *segmentation* refers to the separation of structures of interest from the background and from each other. It is an essential analysis function for which numerous algorithms have been developed in the field of image processing. Typically, segmentation of an object is achieved either by identifying all pixels or voxels that belong to the object (*region-based approaches*) or by locating those that form its boundary (*edge-based approaches*) [1]. The former is based primarily on the intensity of pixels, but other attributes, such as texture, that can be associated with each pixel, can also be used for segmentation. Techniques that locate boundary pixels typically use the image gradient, which has high values at the edges of objects. In medical imaging, automated delineation of different image components is used for analyzing anatomical structure and tissue types, spatial distribution of function and activity, and pathological regions.

Image *quantification* refers to the computational analysis of features extracted from image regions, usually after previous segmentation. Medical image analysis benefits significantly from the precise, fast, repeatable, and objective measurements made by computational resources. These quantitative measurements contribute to the analysis of structure and function in normal and abnormal cases

by addressing many aspects of the data, such as tissue texture, size, shape, and density.

The aim of our efforts, leading to this Thesis, has been to put our knowledge and experience in signal/image processing to service of healthcare. Benefitting from the availability of three-dimensional x-ray computed-tomography images (CT images), and optical images of the skin, we have been able to produce some relevant contributions.

In Chapter 2, we provide a review on state-of-the-art medical image processing literature, discussing how image processing is contributing to healthcare from the perspective of the three ultimate goals of medicine: disease prevention, diagnosis and treatment [2]. In the following paragraphs we introduce the three of them and point to the concerned Chapters.

As computational capabilities are exponentially increased there is an emerging trend for using image processing automatic approaches towards the goal of understanding complex disease phenotypes. After the milestone achievement of sequencing the human genome, some scientist are beginning to propose a new field of work: *phenomics*.

In Chapter 3, we present our work in characterization of emphysematous tissue using high resolution CT images of the lungs. Understanding of emphysema is favored by image quantification techniques applied to several hundred datasets of chronic obstructive pulmonary disease (COPD) patients. In the frame of the COPDGene initiative [3], an unprecedented multi-site effort involving the use of imaging and genetic data, our characterization of emphysema acts as an imaging correlate for genetic factors leading to COPD.

Beyond disease understanding, imaging in medicine has traditionally served the purpose of diagnosing illness conditions, both early and painlessly. In fact one of the first ambitions of medical image processing, *computer-assisted diagnosis* is today more alive than ever.

In Chapter 4 we introduce a novel segmentation algorithm for color images. Although being a general purpose framework, we present results on segmentation of color images of the skin, including dermoscopy imaging, which is the preferred modality for expert diagnosis of skin disease.

In Chapter 5 computer-assisted diagnosis of malignant melanoma in dermoscopy images is tackled via texture quantification of the segmented lesions. Following an emerging trend in dermatology - using texture irregularity to assess malignancy - we present a novel colored texture quantification scheme that might eventually lead to a computer-assisted diagnosis system for melanocytic lesions.

Once disease conditions have been detected, image processing can assist in therapy, reducing both morbidity and mortality. Sophisticated *surgical planning* tools based on visualization and simulation can be envisaged, bringing down the degree of uncertainty of surgical procedures and improving its outcome. *Image-guided therapy*, as a synergistic coupling of robotics and image processing, might improve the outcome of some of the more critical surgical procedures. This is especially true for therapeutical procedures in which an error of few millimiters can bring fatal results, as is the case for neurosurgery or radio-frequency tumor ablation.

In Chapter 6 we present our turn-key solution for solving one of the main bottlenecks in virtual reality surgical planning: segmentation of tissue classes of interest. Aiming at a preexisting plastic surgery planning platform, we have designed, implemented and integrated a segmentation framework that is capable of providing accurate segmentation of fat/muscle/bone in CT images in a wide variety of imaging conditions thanks to a smart compromise between flexibility and human-supervision requirements.

Finally, in Chapter 7 we will outline some conclusions derived from the work presented and devise future lines of work in order to keep broadening the number of applications sustained by medical image processing, as well as to achieve our ultimate goal of improving healthcare via concrete solutions.

Chapter 2

Role of Medical Image Processing

In this Chapter we would like to expose our own perception on the role of medical image processing towards delivering success to what we consider the main goals of healthcare: understanding of disease for its prevention, early and accurate diagnosis, and subsequent successful treatment. Similar classifications of medical image processing techniques have been proposed in the literature [2]. Furthermore, we provide a review of state-of-the-art medical image processing developments benefitting these goals.

2.1 Phenotype Characterization

A key goal of medical research is to understand phenotypic characteristics implied in health and disease. Phenotypic variation is produced through a complex web of interactions between genotype and environment, and such a 'genotype-phenotype' map is inaccessible without the detailed phenotypic data that allow these interactions to be studied. Despite this need, our ability to characterize phenomes - the full set of phenotypes of an individual - lags behind our ability to characterize genomes. Phenomics should be recognized and pursued as an independent discipline to enable the development and adoption of high-throughput and high-dimensional phenotyping [4].

Although far from being exahustive, partial phenotype characterization, together with bioinformatic techniques applied to genetic data, are already improving our understanding of the underlying mechanisms that make two genetic profiles be affected differently by the environment, and result in diverse phenotypic states. Altered phenotypes are among the most reliable manifestations of altered gene functions, and although research using systematic analysis of phenotype relationships to study human biology is still in its infancy [5], many efforts have already been started towards this goal.

One of the most powerful tools for acquiring massive phenotypic information about a certain illment is imaging [6]. Imaging is ideal for phenomic studies,

owing to the availability of many technologies that span molecular to organismal spatial scales, the intensive nature of the characterization and the applicability of generic segmentation techniques to data. Spatial or temporal data on many phenotype classes such as morphology, behaviour, physiological state, and locations of proteins and metabolites can be captured in intensive detail by imaging [6].

To attain this pursuit, fully-automatic image processing techniques must be developed, in the frame of multi-disciplinary efforts that must include image processing specialists, bioinformaticians, physicians and biologists.

The combination of modern imaging techniques and image analysis methods enables the quantification of a broad range of phenotypical alterations, the localization and dynamics of certain signaling events, and the correlation of multiple signaling events in the context of the spatial organization of the biological specimen [7].

Some efforts to characterize disease phenotypic profiles are already ongoing in the context of different health-compromising conditions. Examples include chronic obstructive pulmonary disease [3, 8], lipodistrophy [9], lung function by perfusion with magnetic resonance imaging (MRI) [10], bone architecture for diabetics [11], sleep apnea [12], drug-induced liver injury [13], or hereditary dopamine transporter deficiency syndrome [14].

2.2 Computer-Assisted Detection and Diagnosis

The roles of physicists and engineers in medical imaging have expanded over the years from the study of imaging systems and dose, to the assessment of image quality and perception, the development of image processing techniques, and the development of image analysis methods to assist in detection and diagnosis. The latter is a natural extension of medical physicists' goals in developing imaging techniques to help physicians acquire diagnostic information and improve clinical decisions. Studies indicate that radiologists do not detect all abnormalities on images that are visible on retrospective review, and they do not always correctly characterize abnormalities that are found [15].

Computer-Assisted Detection and Diagnosis (CAD) techniques and systems can broadly be categorized into two types: computer-aided detection (CADe) and computer-aided diagnosis (CADx). CADe implies that radiologists use computer outputs of the locations of suspect regions, leaving the characterization, diagnosis, and patient management to the radiologist. CADe is basically a detection task, i.e., a localization task. CADx extends the computer analyses to yield output on the characterization of a region or lesion, initially located by either a human or a computerized detection system. The computer might output mathematical descriptors to characterize the lesion and/or estimate the probability of malignancy (or other abnormality), leaving the final diagnosis and patient management to the physician.

There is strong synergy between CAD and quantitative image analysis. With continued growth in CAD techniques and the associated increase in accuracies,

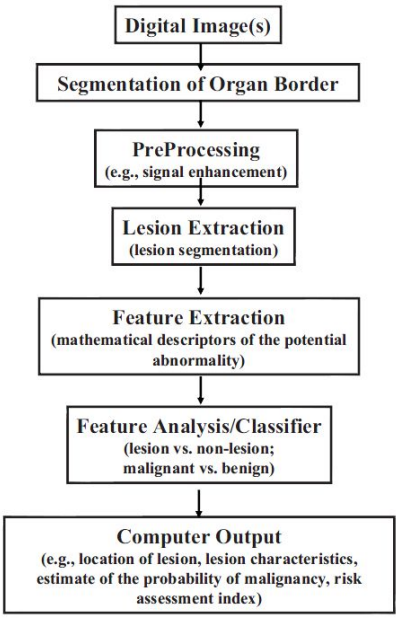

Figure 2.1: Components within a CAD system. (After [15])

quantitative image analysis is a natural extension of the new algorithmic methods to help extract quantitative features and absolute measures of morphology and function to improve medical diagnosis. Conversely, quantitative imaging accentuates the need for highly robust and efficient computer-assisted image analysis tools and stimulates the development of CADe and CADx for the new imaging applications [15].

Computer-aided detection entails the use of a computer output that only yields the location of suspect lesions. Characterization and diagnosis of the abnormality as well as patient management are left for the radiologist. Such systems are most beneficial in imaging examinations in which many cases need to be interpreted with most being normal -such as in screening programs- e.g., screening mammography, low-dose thoracic CT for smokers, and colon cancer screening.

Some of the most prolific application scenarios for CADe include: mammography (microcalcifications [16, 17], masses [18–21]…), thoracic imaging (interstitial disease [22, 23], pneumothorax [24], and lung nodules [25, 26]) or polyp detection in colon imaging [27–29].

Once a lesion is detected, for example, such as in a screening program, further imaging of the abnormality may be necessary in order to justify subsequent patient management such as invasive evaluations (e.g., a biopsy) and/or therapeutic interventions. Thus, the role of a CADx system is to aid in the characterization of an already-found lesion or other abnormality in terms of its morphological or functional attributes, and in the estimation of its probability of malignancy or other disease state.

As clinical CADe systems begin to give more information beyond just local-

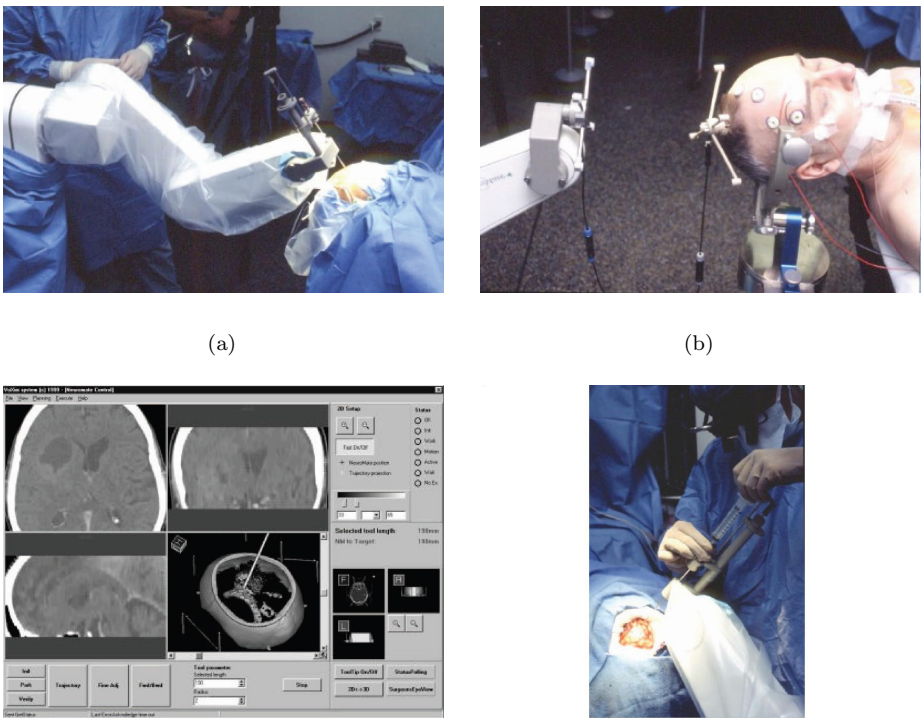

(a) (b)

(c) (d)

Figure 2.2: Robotic brain surgery. (a) The robotic arm holding an aspiration needle. (b) Robot-to-patient registration with optically tracked fiducials. (c) Screenshot from CT-based treatment planning. (d) Surgeon performing the aspiration. (After [36])

ization, CADx is slowly being introduced. Scenarios for application include malignancy of breast masses [30,31] and pulmonary nodules [32–34].

In Fig. 2.1 we highlight the main stages involved in a computer-assisted detection /diagnosis system. The main bottlenecks of the system correspond to the segmentation (organ and lesion) and feature extraction stages.

2.3 Image-Based Therapy

Medical image processing can be of assistance also when disease has already occurred. A large family of medical interventions can be planned ahead of time and executed in a reasonably predictable manner with the assistance of computerized methodology.

Two main aspects of medical intervention have been outlined as greatly facilitated by medical image processing: plannification and execution. As a consequence interventional planning and image-guided interventions arise [35].

Interventional planning, refers to procedures in which medical images, anatomical atlases, and other information are combined preoperatively to model an individual patient. The computer then assists the surgeon in planning and optimizing an appropriate intervention. Various computer programs that generate 3D representations of tomographic imaging data for surgical planning have been developed, and the most currently available image guidance systems offer surgical planning tools. In the field of craniofacial and plastic surgery, preoperative computer-generated models are emerging as a means of predicting the morphological characteristics after surgery. In orthopedic surgery, such software has been developed to plan bone and joint surgery, and in hepatic surgery, 3D software has been reported to improve surgical planning and training. For a review of medical applications benefitting from computer-based interventional planning see [37].

Image-guided intervention, on the other hand, refers to procedures in which real-time medical images and other sensor data are used to register the preoperative plan to the actual patient and the model and the plan are updated throughout the procedure. Often, this includes the physician performing the actual intervention with the assistance of the computer, using appropriate technology (robotics, mechatronics, optical guidance, perceptual guidance, etc.) for the intervention.

The following sequence of steps is typical for image-guided interventions using computer assistance [38]:

- Preoperative images are acquired (typically tomographic images);
- The surgical instruments are tracked using a localizer;
- The patient anatomy is registered to the preoperative image;
- The position of the surgical instruments is displayed on this image relative to the patient anatomy;
- The physician uses this virtual display to manipulate the instruments to accomplish the procedure;
- A confirming image is obtained upon procedure completion.

During the interventional planning phase, the preoperative images are processed, and a computational model of the patient is created and interactively visualized for the surgeon or practitioner. Often multiple imaging modalities are fused. Based on this patient-specific model, a surgical plan is created. The plan can be as simple as entry and target points for a biopsy, but it may be as delicately complex as an intensity-modulated radiation therapy plan. Next, the physician simulates the surgery by performing a virtual dry run, like a computer game. In some applications, such as maxillofacial surgical planning, various approaches are tried out before converging on the optimal plan.

Geometric relationships are fundamental for the extension of planning to actual image-guided procedure, and the registration of actors (robots, sensors, images, and the patient) is a traditional issue (e.g., [39, 40]). As the final goal of registration is to determine the position of a surgical tool relative to the pathology

targeted for intervention, it is desirable to perform the registration based on the image itself. When image-based registration is not practical or possible, external localization is applied. Typical external localizers are electromechanical, optical, electromagnetic, or ultrasonic, each with different pros and cons [39]. One example of external fiducials is shown in Fig. 2.2, in which the NeuroMate™ robot system (Integrated Surgical Systems, Davis, CA), a commercially available, image-guided, robotic-assisted system is used for a stereotactic procedure in neurosurgery [36].

Effective image-guided intervention requires that we integrate imaging and tracking devices into the robotic end effectors or surgical tools themselves to physically couple image and device coordinate frames, thus eliminating the traditionally greatest source of inaccuracy and operational hazard: misregistration. The ultimate goal is local imaging, local guidance, and local actuation, all in one device.

The clinical applications that have traditionally driven these technologies include:

- Percutaneous needle-based interventions: prostate brachytherapy [41] and abdominal biopsies [42];
- Transcutaneous interventions with x-ray radiation therapy [43] or high-intensity focused ultrasound [44] for tumor ablation;
- Intracavity interventions: transrectal needle biopsies [45, 46];
- Neurosurgery [36, 47–50];
- Orthopedic surgery: hip joint reconstruction [51, 52], knee surgery [53], and maxillofacial surgery [54];
- Cardiac surgery: stem cell implantation therapy [55, 56], ablation therapy [57, 58], coronary artery bypass grafting [59, 60], and intracardiac procedures [61–63].

Chapter 3

Advances for Phenotype Characterization: Quantification of CT Scans

Emphysema Characterization in Multi-scanner CT-Datasets Using Local Intensity Distributions

---

3.1 Introduction

Chronic obstructive pulmonary disease (COPD) is a major cause of chronic morbidity and mortality throughout the world. Many people suffer from this disease and die prematurely of it or its complications. COPD is defined as incompletely reversible obstruction of the airways during exhalation. Pathologic changes characteristic of this disease are found in the proximal airways, distal peripheral airways, the lung vasculature, and the lung parenchyma [64]. The presence of these changes are typically associated with tobacco smoke exposure and the disease is estimated to become the third leading cause of death by the year 2020 [65].

Standard clinical evaluation of patients with COPD includes spirometric measures of lung function, also known as pulmonary function tests (PFTs). While useful for offering a simple classification scheme for disease severity, such maneuvers are imperfect for the detection and characterization of the types of smoking related lung disease and their relative contributions to lung dysfunction and may fail in the diagnosis of early stages of disease [66] . Because of this, radiologic characterization of lung structure, specifically emphysematous destruction of the lung parenchyma and remodeling of the airways has become an area of intense research.

Emphysema is a chronic respiratory disorder, encompassed within COPD, which

is characterized with permanent, abnormal dilation of the distal airspaces. Its presence is associated to physical limitations and degraded quality of life. For years, evidence has been gathered about the suitability of computed tomography (CT) for assessing the severity and extension of emphysema in vivo, which allows for monitoring its progression and evaluating its response to therapy [67,68]. Visual interpretation of high-resolution computed tomography (HRCT) images of the chest and the patterns associated with emphysematous lung disease is time-consuming and operator dependent. Automatic quantification has extensively been investigated as an alternative approach that might reduce the inter-subject variability of such assessments, and allow for large scale analyses of CT scans in population studies. A standard technique employed for quantification of emphysema is called *densitometric* analysis [69]. This technique consists of choosing a Hounsfield Unit threshold in the lung mask that will delineate emphysema from non emphysematous tissue. The volume elements with Hounsfield units (HU) below the threshold are added up and divided by the total number of voxels in the lungs to provide a fraction of emphysema. Previous histopathologic correlation has determined that this threshold lies somewhere -910 and -960 HU based upon image acquisition and reconstruction parameters. Although the densitometry is very sensitive to noise and acquisition parameters [70], it represents the method of choice for most studies carried out in clinical settings and constitutes the preferred correlate for visual assessment in comparison studies [71]. This is likely based in part on its computational simplicity and its conceptual appeal to investigators.

Measures based on fixed thresholds disregard the information present in the morphology of the emphysema subtypes such as shape and size distribution of bullae [72]. For that reason, much of the work developed in the field of emphysema quantification in CT has attempted to enrich thresholding approaches by incorporating the spatial structure of density values, or *texture* [73]. Some of the methods brought forward from the computer vision literature into this particular problem include combinations of features extracted from co-occurrence matrices, run-length matrices and local histograms [74–83]. Others combine these with local spatial relations between intensity levels [82–84], multi-resolution features obtained from filter banks [77, 78, 80, 81], and even fractal dimension descriptions [73,74,79]. Most of these approaches introduce several disadvantages: low performance, poor understanding of the consequences of inter-scanner variability, and obscurity of physical meaning.

The justification for using texture approaches is usually founded on the spatial regularity inherent to the lung structure. Emphysema has previously been described at the level of secondary pulmonary lobule [85]. The secondary lobule is the smallest subunit of the lung with a central vessel-airway pair and circumscribed by connective tissue. Radiologic manifestations of disease at this level are often characteristic of unique pathologic processes. As emphysema progresses, the parenchymal tissue gradually dissapears until areas of low attenuation occupy the space of one or several secondary lobules.

There exist prototypic radiologic patterns of emphysematous involvement of the secondary lobule corresponding to centrilobular, paraseptal and panlobular disease [86]. Fig. 3.1 provides an abstract representation of the basic structure of the secondary pulmonary lobule displaying these distinct emphysema patterns.

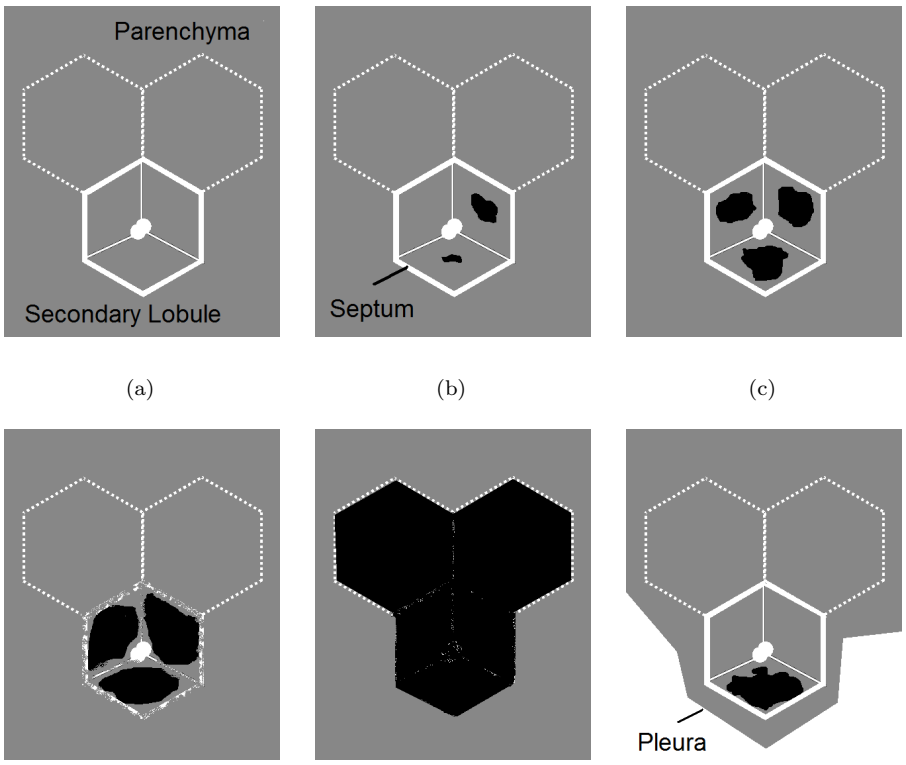

Figure 3.1: Figurative diagrams capturing the basic structures of the emphysema patterns under study. (a) Healthy tissue. (b) Mild centrilobular emphysema. (c) Moderate centrilobular emphysema. (d) Severe centrilobular emphysema. (e) Panlobular emphysema. (f) Paraseptal emphysema

Centrilobular emphysema (Figs. 3.1(b)-3.1(d)) describes secondary lobules that keep part of the connective tissue surrounding the lobe and the airway-vessel ensemble, so their spatial extent is distinguishable on HRCT. Panlobular emphysema (Fig. 3.1(e)) refers to low-attenuation areas with more general effacement of lung structures and destruction of several adjecent lobules. Finally, paraseptal emphysema (Fig. 3.1(f)) is characterized by low attenuation lesions in the secondary lobules adjecent to the pleural surface. The most common of this patterns is centrilobular emphysema which may be considered in subcategories such as mild, moderate and severe depending on the involvement of disease. This description ultimately leads to six emphysema patterns of interest: normal tissue (NT), paraseptal emphysema (PS), panlobular emphysema (PL) and mild/moderate/severe centrilobular emphysema (CL1/2/3). In Fig. 3.2 we provide actual CT examples of these patterns that may serve as a visual reference for their radiographic expression.

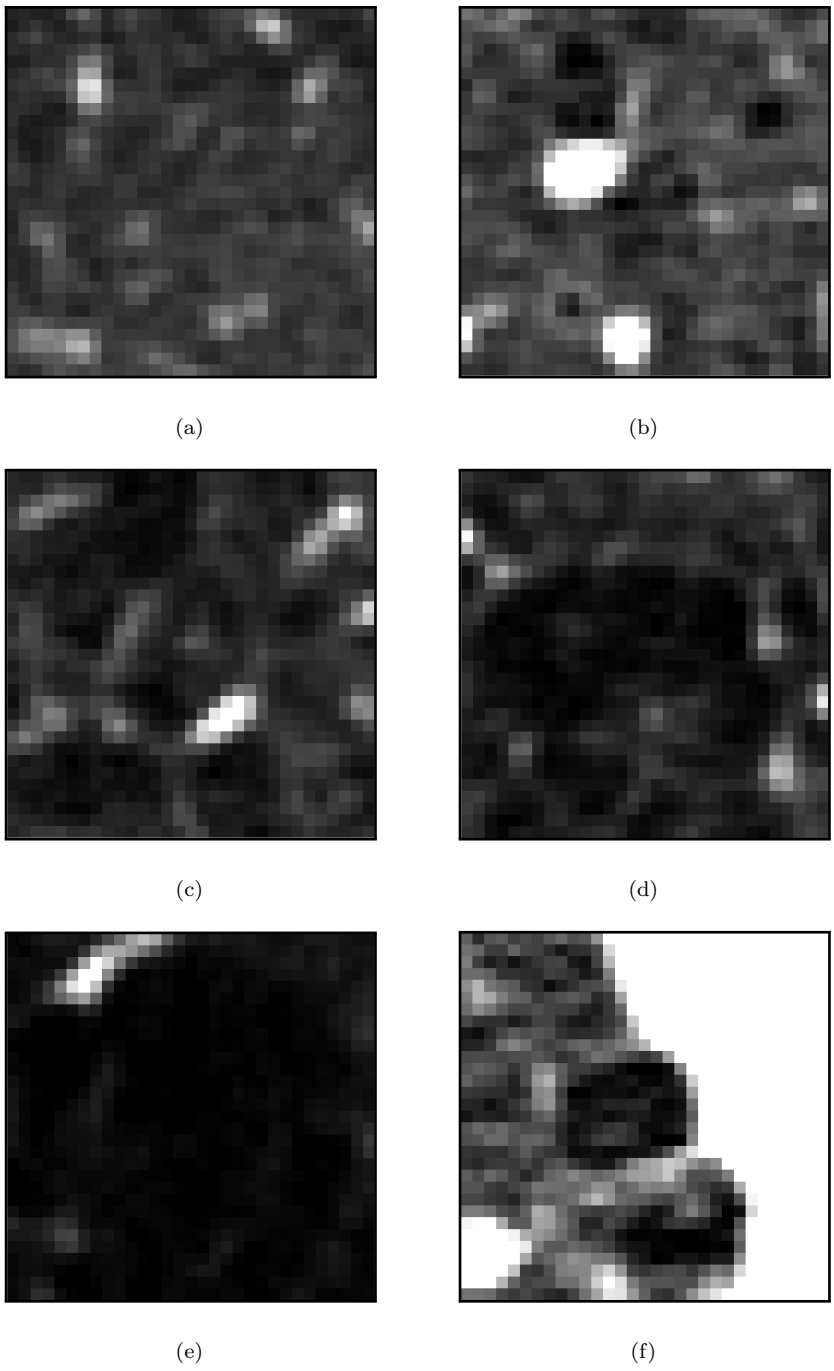

(a) (b) (c) (d) (e) (f)

Figure 3.2: Examples of emphysema regions of size 24.18×24.18 mm^2, extracted from real CT scans, in the window $[-1000, -500]$. (a) Healthy tissue. (b) Mild centrilobular emphysema. (c) Moderate centrilobular emphysema. (d) Severe centrilobular emphysema. (e) Panlobular emphysema. (f) Paraseptal emphysema

3.1.1 The Coupling of Local Texture and Local Intensity

In investigating the process of classifying the patterns of emphysema, we must ask ourselves what is the human observer considering for building their assessment. Based on our experience, we postulate that this pattern recognition problem is primarly based upon variations in local intensity rather than a recognition of spatial regularity (spatial statistics of order greater than one), thus filling the gap between current practices and existing sophisticated approaches. Interestingly, most texture approaches available in the literature suffer from what we have come to call the *coupling* of texture and intensity. Taking the example of classic Haralick [87] texture features, co-occurrence and run-length matrices, together with the local histogram, are built from a local region of interest (ROI).

First of all, these representations, are always obtained according to a given binning strategy with respect to the intensity levels. The reason for this is the sparsity of those matrices and the histogram itself when constructed from relatively scarcely populated regions. This problem grows more relevant as texture features (spatial statistics of order greater than two) get involved in the calculation, and coarser and coarser binnings become necessary for proper population of the matrices. Besides, most frequently the texture descriptors obtained from those representations indirectly contain intensity features, e.g. the mean. As a consequence it is often impossible to segregate local intensity features from spatial regularity features.

The same can be said about filter banks, morphological operators and also about methods which try to model the underlying random fields.

One fortunate exception to this difficulty resides in the work by Sørensen et. al. [84]. In their inspiring article, they retrieve one of the most robust approaches available in the texture literature, known as Local Binary Patterns (LBPs) [88, 89]. As outlined in Sect. 3.2, this descriptor is invariant to monotonic intensity range distortions. Its binary nature allows for full separation between textural features and intensity. Furthermore, as reported in their work, coupling of intensity and LBPs outperforms many previously proposed texture-intensity coupling descriptors, for this particular problem.

For this reason we use the methodology proposed in [84] to benchmark our local intensity descriptions, in an attempt to demonstrate our hypothesis of textural irrelevance.

3.1.2 Our Main Contributions

The main goal of our work has been to provide new insights on the true characteristics that allow the human expert to discern between emphysema patterns. In particular, we demonstrate that the use of full local intensity histograms convey as much significant information about emphysema stages as previously existing, much less efficient textural descriptions. Furthermore, we will be the first authors to outline the effects of applying emphysema pattern recognition techniques on data proceeding from different pieces of acquisition equipment, from different vendors and varying calibration states. To the best of our knowledge, no work on emphysema classification has ever been performed for more

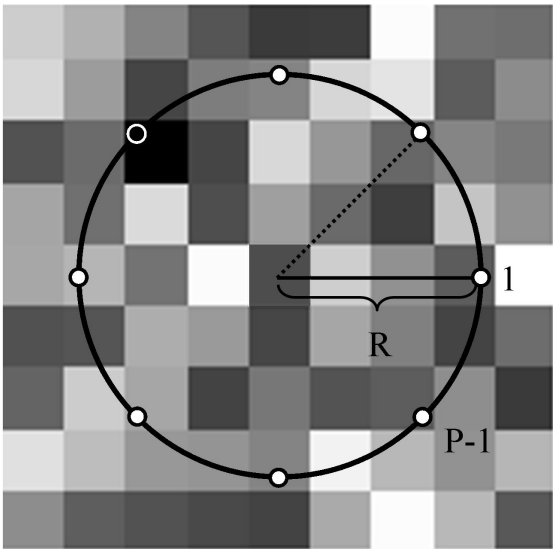

Figure 3.3: Example of LBP computation. In this case $P = 8$ and $R = 3.5$. The corresponding $\mathrm{LBP} = 239 =$'10111111' and $\mathrm{LBP}^{\mathrm{ri}} = 127 =$'01111111'.

than one physical device. Finally, under the light of our findings on the completeness of the local intensity description, we propose several techniques for dealing with the main inconvenience of this kind of approach: the sparsity of histogram description that occurs as a consequence to the relatively coarse sampling of the textures of interest in clinical imaging resolutions.

Ultimately, the validity of our results is strengthened by the size of our experimental dataset, the biggest one used to date for emphysema pattern discrimination (with a number of scans rising one order of magnitude above that of our main benchmark reference).

3.2 Methods

3.2.1 ROI Definition

The proposed emphysema quantification methodology is based in proper labeling of two-dimensional regions of interest that can be either sparse samples on a number of chest CT scans, or densely extracted regions from a single scan. The definition of the physical extent of such region of interest is critical to the success of the classification, since an ROI that is too small will not contain a whole secondary lobe, and an ROI that is too big will dim the boundaries between regions with different pattern classes. In [84] the authors perform a comparative analysis of several ROI sizes. They define their ROIs in pixels, disregarding physical units. This is valid because all the scans in their dataset display the same spatial resolution, thus establishing a fixed relation between image pixels and physical units.

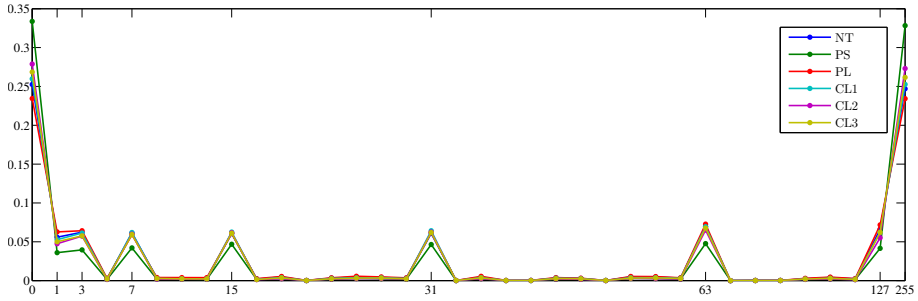

Figure 3.4: Average LBP code histograms for the six emphysema classes under study

Since secondary pulmonary lobes present sizes that are consistent, up to some extent, among patients, we can use the reported optimal size and spatial resolution of CT scans to arrive at a -reportedly- adequate physical scale of emphysema patterns: 24.18×24.18 mm^2.

It is worth noting that since our data proceeds from a variety of scanners, a previous normalization stage is required in order to compare ROIs that are equally populated and share the same physical extent. Thus, we proceed by resampling of the image domain with a spacing of 0.78 mm$\times$0.78 mm and end up with ROIs made up of 31×31 pixels with the aforementioned physical size. This resampling requires interpolation, and in all our experiments we have made use of bicubic interpolation as introduced by [90].

3.2.2 High Order Spatial Statistics: Local Binary Patterns

Local Binary Patterns (LBPs) were originally proposed by Ojala et. al. [88] for 3×3 neighborhood intensity relations, and later refined so they could exhibit the properties of rotation invariance and multi-resolution capabilities [89]. Their suitability for emphysema pattern discrimination has extensively been explored in [84]. We will provide here the basic formulation as employed in the latter. Please refer to the preceding references for further details. For every pixel, its LBP code can be obtained by means of thresholding its neighbors by the pixel's intensity. After thresholding, the pixel's neighbors can be either above or equal/below the threshold, so they are assigned binary values 1 and 0, respectively. This provides a binary word that encodes the local structure surrounding the pixel.

The definition of the neighbors involved in the formation of the binary word can be dependent on a certain distance from the center pixel, and can be taken in a given number as the circumference around the pixel is followed. If some rule is applied to the binary word, so that any circular shifts get lost, then rotation invariance can be obtained. One such rules could be the following: rotate the word until it is minimum.

Mathematically, let I be an image and $\vec{x}$ a given center pixel in its domain. If $\vec{x}_p = [-R\sin(2\pi p/P), R\cos(2\pi p/P)]^T - \vec{x}$ are P local samples taken at radius R

around $\vec{x}$, and $H(\cdot)$ be the Heaviside function. Then we define

$$\mathrm{LBP}(\vec{x};P,R) = \sum_{p=0}^{P-1} H(I(\vec{x}_p) - I(\vec{x}))2^p \quad . \tag{3.1}$$

In order to obtain the image values with sub-pixel precision, a proper image interpolation method needs to be employed. In all our experiments we have exploited bicubic interpolation as we did for image resampling (Sect. 3.2.1).

It can easily be observed that this representation is invariant to monotonic gray-scale transformations. In order to achieve rotation invariance, we retrieve the following rule, that will transform all rotations of a given binary word to a same transformed word:

$$\mathrm{LBP}^{\mathrm{ri}}(\vec{x};P,R) = \min_i(\mathrm{ROR}(\mathrm{LBP}(\vec{x};P,R),i)) \quad , \tag{3.2}$$

where $i = 0,...,P-1$ and $\mathrm{ROR}(b,i)$ performs i circular bit-wise right shifts on the P-bit binary number b.

After application of rotation invariance, not all possible 2^P binary codes are obtainable anymore, but only a small selection of them: those which happen to be minimal under all possible circular shifts. See Fig. 3.3 for an illustrative example of LBP for fixed values of P and R.

Once an LBP number has been assigned to every pixel in an ROI, LBP number normalized histograms can be constructed. Such representation captures the frequency of certain micro-structures like corners, edges and constant regions. This was discussed in detail both in the work by Ojala et al. [88, 89], and for the emphysema application scenario by Sørensen et al. [84].

One limitation of this intensity-invariant texture description has already been described by Tan et al. [91]. LBP numbers display low robustness at describing textures with constant-valued regions and certain levels of noise. In these circumstances LBP numbers take random values, thus obscuring the underlying constantness of the texture and accounting for micro structures that are actually but noise.

For the case of emphysema patterns, going back to Fig. 3.1, we might predict that as more connective tissue gets destroyed, the amount of textural features like edges and corners should decrease. Simultaneously, the amount of flat regions should increase as more and more of the sample pixels occur inside a low density region (air). But unfortunately, emphysema samples proceeding from CT scans, as can be seen in Fig. 3.2, contain significant amounts of noise. Therefore the suitability of the LBP description for the problem at hand needs to be further investigated.

In Fig. 3.4, we have represented the average LBP histogram for all samples belonging to the 6 classes under study: NT, PL, PS, CL1/2/3. As we will formalize in Sect. 3.3, it is extremely hard to separate the 6 classes according to LBP histograms, which will lead us to postulate other approaches. It is worth noting that although LBP histograms are intensity-deprived representations, in their work Sørensen et. al. [84] proposed a methodology based on the coupling

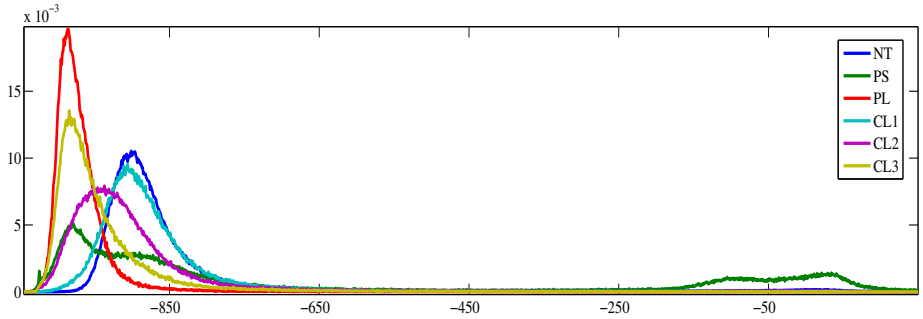

Figure 3.5: Average intensity histograms for the six emphysema classes under study

of LBPs and intensity histograms, obtaining remarkable classification success. It is one of our goals to investigate which part of that success is due to the intensity part of the description, and which part can be genuinely attributed to textural information.

3.2.3 First Order Spatial Statistics: Local Intensity

One of the main postulates of our work is the sufficiency of local intensity distributions for emphysema pattern discrimination. We intend to demonstrate that these first-order spatial statistics are indeed enough to characterize the nature of our tissue classes. As a first intuitive approach we show in Fig. 3.5 the average intensity histograms for the six classes under study. These estimates were built from all the available pixel intensities in our training ROIs. Compare the apparent separability of this intensity description with that of LBP description as depicted in Fig. 3.4. The intensity probability function of a given tissue class is a complete description of its first-order spatial statistics. In parametric approaches, the underlying probability function for a given tissue class can be established in terms of a model distribution and a number of statistical moments of sample histograms. This is partially exploited in some texture approaches like Haralick descriptors [87]. As opposed to this, non-parametric approaches do not assume any model distributions, and do not require parameter estimation. Instead, all the available first-order intensity information available in a sample is employed for estimating the probability density function for its corresponding class. We propose here the use of non-parametric descriptions of the intensity distribution for tissue classes. Our non-parametric estimation of the underlying probability function is based on histograms.

The main difficulty for this approach resides in the sparsity of intensity histograms when obtained from relatively small tissue samples. In this case, we are building histograms that take values for several hundred intensity levels from samples that contain only hundreds of pixels. This can be rephrased into saying that histograms extracted from small ROIs are too rough as estimations of the underlying intensity distributions. Sparsity can incur on increasing the error when comparing histograms, which is actually our preferred technique for comparing the underlying statistical distributions. We show in Fig. 3.6 the histograms for the six tissue examples in Fig. 3.2 in comparison with average

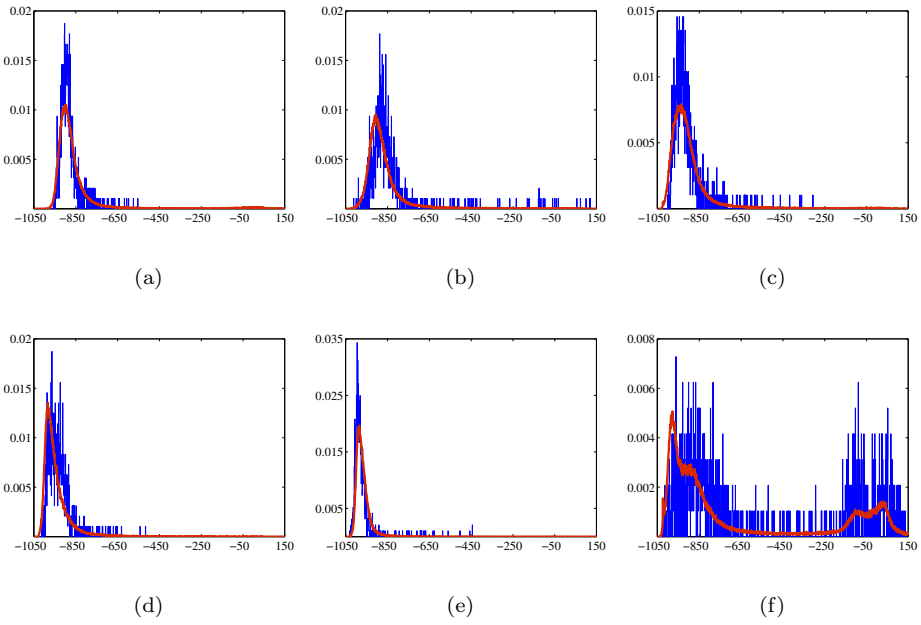

Figure 3.6: Comparison of mean histograms (red) for each class and example histograms (blue) for emphysema regions in Fig. 3.2. (a) Healthy tissue. (b) Mild centrilobular emphysema. (c) Moderate centrilobular emphysema. (d) Severe centrilobular emphysema. (e) Panlobular emphysema. (f) Paraseptal emphysema

histograms across all samples.

Several techniques can be envisaged, which can deal with our histogram sparsity issue.

3.2.3.1 Adaptive Binning

This consists of reducing the number of bins in the histogram in such manner as to increase the population of every resulting bin. As proposed in [88], a good way to perform this quantization is one in which the original distribution of intensity values is taken into account. In particular, we want to produce a variable bin-size representation, such that the total feature distribution across all ROIs in the training set is made approximately uniform under the new representation.

This binning can be obtained by equalizing the histogram of all intensities in our dataset. In fact the obtained intensity transformation can be used to map the original binning P onto the adaptive one P''. Such procedure has been described in the context of image processing as a *palette* change.

Consider a collection x of pixel values from all available scans, let n_i be the number of those pixel values equal to i. Then the global probability that any

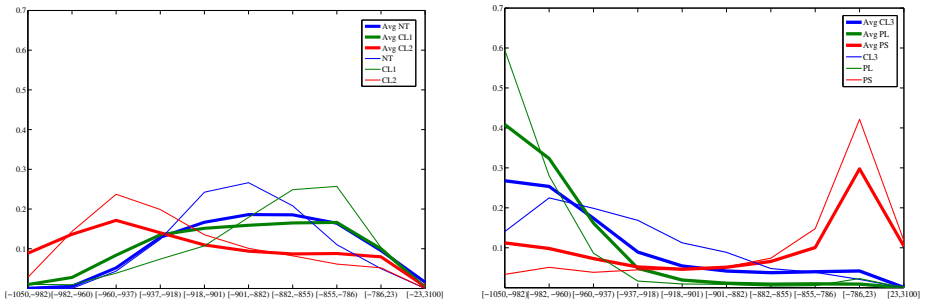

(a) (b)

Figure 3.7: Comparison of mean histograms (thick lines) for each class and example histograms (fine lines) for emphysema regions in Fig. 3.2 after transforming to adaptive binning with $N = 10$. (a) Healthy tissue, mild centrilobular emphysema and moderate centrilobular emphysema. (b) Severe centrilobular emphysema, panlobular emphysema and paraseptal emphysema.

pixel takes value i is:

$$p_x(i) = p(x = i) = \frac{n_i}{n}, \quad 0 \leq i < L \ , \tag{3.3}$$

L being the total number of gray levels in our representation domain and n being the total number of pixels in the whole dataset. It is known that the cumulative distribution function corresponding to p_x is:

$$cdf_x(i) = \sum_{j=0}^{i} p_x(j) \ , \tag{3.4}$$

which is the dataset's accumulated normalized histogram. We would like to create a transformation of the form $y = T(x)$ to produce a new image dataset y, such that its CDF will be linearized across the value range, i.e. $cdf_y(i) = i/I_{max}$. The properties of the CDF allow us to perform such a transform; it is defined as

$$y = T(x) = cdf_x(x) \ . \tag{3.5}$$

If we then uniformly quantify the intensities y to N levels we can obtain a new palette P'. The operation that must be applied to obtain the adaptive binning can be expressed in terms of P' and T. If we define the new binning as

$$P'' = T^{-1}(P') \ , \tag{3.6}$$

then histogram equalization is implemented as a palette change, and the equalized histograms can be obtained by a fixed transformation that can be applied separately to histograms of any sample in the dataset without altering intensity levels. To perform this operation for discrete histograms, it is equivalent to divide the total number of pixels by the desired number of quantization levels N, and iteratively -from left to right or from right to left- select quantization levels so that the obtained fraction of pixels are contained in every quantization level.

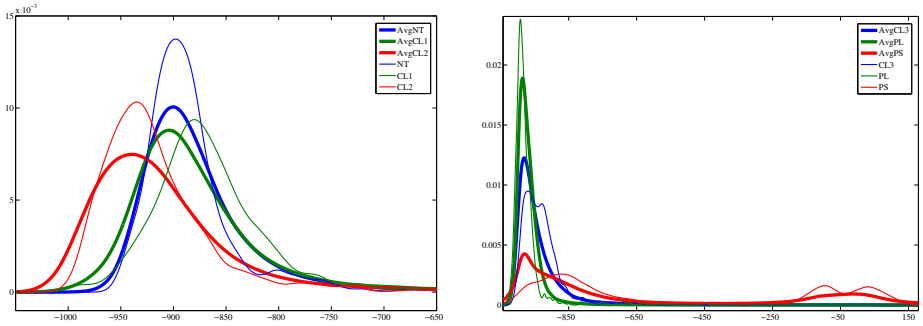

(a) (b)

Figure 3.8: Comparison of mean histograms (thick lines) for each class and example histograms (fine lines) for emphysema regions in Fig. 3.2 after computing their kernel density estimates. (a) Healthy tissue, mild centrilobular emphysema and moderate centrilobular emphysema. (b) Severe centrilobular emphysema, panlobular emphysema and paraseptal emphysema.

Compare Fig. 3.7 with Fig. 3.6. Notice how the sparsity problem is solved at the cost of decreased intensity range resolution.

3.2.3.2 Kernel Density Estimation

Instead of using histograms as sparse representations of the underlying intensity probability distributions, the distributions can be estimated using the method known as *kernel density estimation* or *Parzen window* method. Let $(x_1, x_2, \ldots, x_n)$ be an independent and identically distributed sample drawn from some distribution with an unknown density f. We are interested in estimating the shape of this function f. Its kernel density estimator is known to be

$$\hat{f}_h(x) = \frac{1}{n}\sum_{i=1}^{n} K_h(x - x_i) = \frac{1}{nh}\sum_{i=1}^{n} K\Big(\frac{x - x_i}{h}\Big), \tag{3.7}$$

where $K(\cdot)$ is the kernel -a symmetric but not necessarily positive function that integrates to one- and $h > 0$ is a smoothing parameter called the *bandwidth*. Very often standard Gaussian kernels are used due to its convenient mathematical properties. The bandwidth of the kernel is a free parameter which exhibits a strong influence on the resulting estimate. In all our results we use the methodology described in state-of-the-art work by Botev et al. [92], to determine the value of the bandwidth parameter. See Fig. 3.8 for a plot of the density estimates averaged for the six classes under study and for the six samples in Fig. 3.2.

3.2.3.3 Cross-Bin Histogram Distance Measures

When histogram sparsity stands as a difficulty for comparing histograms in a pattern classification scenario, using cross-bin histogram distance measures can

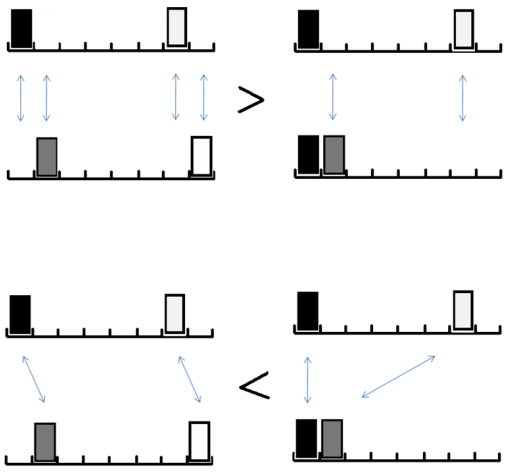

Figure 3.9: Example illustrating the significance of cross-bin distance measures for histogram comparison. In the upper section of the figure bin-to-bin comparison results in perceptual mismatch, which is solved when cross-bin interactions are considered like in the lower section. The inequality sign refers to greater/lower measured distances.

circumvent the problem in a non-parametric natural way. As opposed to bin-to-bin histogram distances, cross-bin histogram distances do not only account for dissimilarity across overlapping bins but model also the interactions among all bins. This provides improved robustness against sources of variability that can affect the histogram in unpredictable but bounded ways. Moreover, cross-bin distances can more closely match perceptual dissimilarity as perceived by the human visual system. To illustrate this fact we include in Fig. 3.9 a toy example in which bin-to-bin comparison is clearly in disagreement with subjective assessment, while cross-bin comparison is more appropriate. For a survey on histogram distance measures we recommend the introductory sections of [93] and [94].

Several cross-bin distances have been proposed in the literature. Relevant examples include heuristic *Quadratic Form Distance* [95], and especially a version of Wasserstein metric known as the *Earth Mover's Distance* (EMD) [94].

Under this latter paradigm, the distance between histograms is the amount of work needed to reconfigure, in an optimal manner, one into the other as if they were piles of dirt and the explicit distances between populated locations were known. One unit of work corresponds to moving one unit of dirt over unit ground distance. This corresponds to a very well-know linear programming problem: The Monge-Kantorovich transportation problem. Unfortunately this optimization problem has $O(n^3 \log n)$ complexity in the general case. Approximations have been envisaged resulting in the so-called *Diffusion Distance* [96], and the *Match Distance*, which stands for the analytic solution of the EMD when ground distances equal bin distances in one-dimensional normalized histograms [97]. The match distance between such histograms equals the $\mathscr{L}_1$ distance between their corresponding cumulative histograms, as described in Subsect. 3.2.5. See

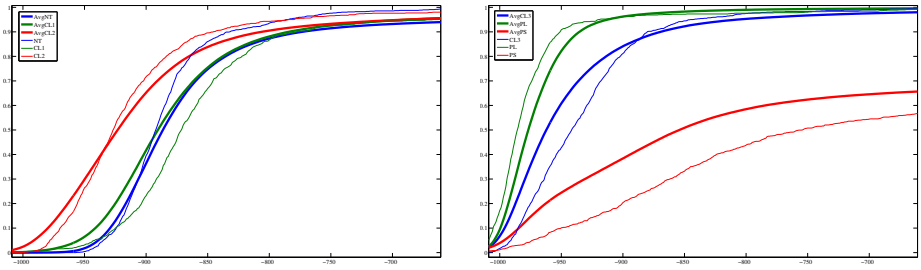

(a) (b)

Figure 3.10: Comparison of mean cumulative histograms (thick lines) for each class and example cumulative histograms (fine lines) for emphysema regions in Fig. 3.2. Cross-bin EMD is equivalent to a bin-to-bin comparison between these cumulative histograms. (a) Healthy tissue, mild centrilobular emphysema and moderate centrilobular emphysema. (b) Severe centrilobular emphysema, panlobular emphysema and paraseptal emphysema.

Fig. 3.10 for a comparison between average cumulative histograms and example cumulative histograms for the six classes under study. Notice how histogram sparsity has been naturally dealt with by using this improved distance measure without the need for explicit probability distribution estimation.

3.2.4 Benchmark Descriptors: Sørensen's LBPs

In order to support our hypothesis that previous approaches considering higher order spatial statistics are over-descriptive, we will benchmark our proposed methodology against state-of-the-art work by Sørensen et al. [84]. Their description is based on the coupling of intensity and LBPs in a two-dimensional histogram. Using adaptive binning for intensities, and rotation-invariant LBPs their two-dimensional representation accounts for intensity and micro-structure for every pixel in the ROI. We have tried to reproduce exactly their technique, but for further details we refer the reader to their original work. Although developed for distinguishing only three emphysema patterns, for comparison purposes we show in Fig. 3.11 average joint histograms for the six classes under study.

3.2.5 Classifier

All previously described histograms (LBP, intensity, joint) are taken as representation of a given ROI. In order to classify unseen ROIs we make use of the *kNN* classifier [98]. This classifier is the natural choice when working in a distance representation of objects, it is non-parametric and it is also the classifier employed in the LBP literature [88, 89]. As in [84], we will use Minkowski-form

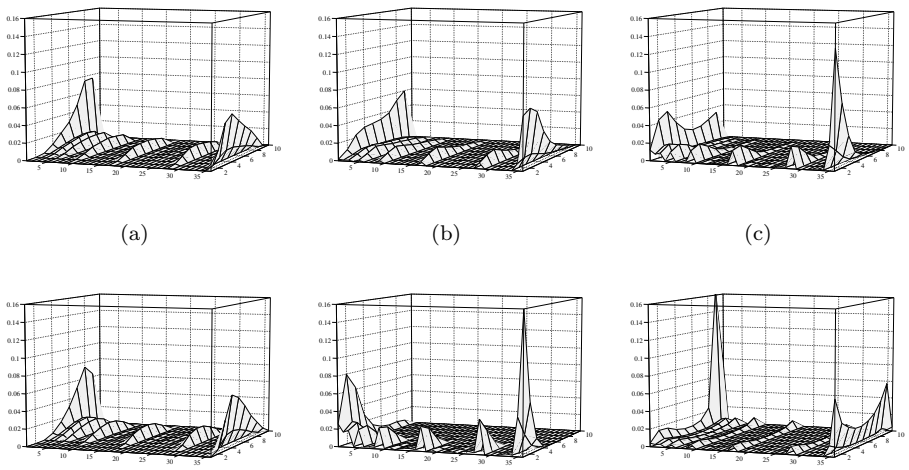

(a) (b) (c)

(d) (e) (f)

Figure 3.11: Comparison of mean Sørensen's two-dimensional histograms for each class. (a) Healthy tissue. (b) Mild centrilobular emphysema. (c) Moderate centrilobular emphysema. (d) Severe centrilobular emphysema. (e) Panlobular emphysema. (f) Paraseptal emphysema

distance $\mathscr{L}_1$:

$$D(X,Y) = \sum_i \left| f(i;x) - f(i;y) \right| \ . \tag{3.8}$$

This distance is computed from a test sample to every training sample and then we classify it using the most frequent class label among the k closest samples in the training set.

3.2.6 Full-Lung Quantification

To extend the analysis of isolated ROIs to emphysema quantification in full lungs we need to extract ROIs from the lung parenchyma. Therefore, lung segmentations are required for analyzing the lung field. We want to exclude airways and vessels from our analysis, so we want to rely on lung, vessel and airway segmentations. These were obtained using the system described in [99]. Centering and classifying an ROI at a given location provides a label for that location. Only segmented locations should be considered for the classification. But since we do want to allow for out-of-lung, vessel and airway pixels to be present in ROIs, we do not have to worry about segmentations once the ROI has been located. This matches the approach demonstrated in [84].

Once every segmented voxel has been classified as belonging to one of the six classes under study, we need a certain criterion to transform that labeling into a global measure. Soft and hard fusion strategies have been proposed [81]. In [84] a thorough comparison arrived on the conclusion that no improvement was achieved for soft fusion, so in our work we adopt the more intuitive hard

Table 3.1: Sample distribution across scan models (P64 = Philips 64 slice, S64 = Siemens Sensation-64, SD = Siemens Definition, G64 = General Electrics VCT-64, SAS = Siemens Definition AS+, G16 = General Electrics LS 16, P40 = Philips 40 slice, S16 = Siemens Sensation-16, SF = Siemens Definition Flash).

	P64	S64	SD	G64	SAS	G16	P40	S16	SF
NT	9	147	136	56	6	94	0	1	0
CL1	0	52	75	29	20	32	2	3	4
CL2	5	87	109	30	4	28	3	21	0
CL3	2	21	91	17	0	43	0	4	0
PL	0	8	63	21	6	32	6	12	0
PS	6	62	104	29	1	34	2	7	1

Table 3.2: Average Classification Success for $k = 5$

Method	Avg. Classification Success
LBP	0.3034
LBPINT	0.6497
AB	0.6539
KDE	**0.6641**
EMD	0.6258

fusion approach. This is articulated into a measure called *Relative Class Area* (RCA). If $|S|$ is the number of voxels in lung mask S, $\omega(\vec{x}_i)$ is the label assigned to voxel $\vec{x}_i$, and ω_i is one of the six emphysema classes, then

$$\mathrm{RCA}_{\omega_i} = \frac{1}{|S|} \sum_{x_i \in S} \delta(\omega_i - i) \ , \tag{3.9}$$

with $\delta(\cdot)$ the Kronecker delta function.

3.3 Experimental Results

3.3.1 Data

All data used in this work is part of the COPDGene Study [3], which is one of the largest studies ever to investigate the underlying genetic factors of Chronic Obstructive Pulmonary Disease or COPD. The COPDGene Study employs CT imaging to allow for accurate diagnosis of lung disease. 342 CT scans were randomly selected from the COPDGene cohort with 50 scans each from smokers with Global Initiative on Obstructive Lung Disease severity level (GOLD) 0 to 4 and GOLD U plus 50 non-smoking controls. For each of these scans clinical phenotype data, extent and severity of emphysema, gas trapping and airway wall

Table 3.3: Confusion Matrices for $k = 5$. Row indicates true label, and column indicates obtained classification

(a) LBPINT

	NT	PS	PL	CL1	CL2	CL3
NT	396	5	1	45	2	0
PS	2	202	12	6	10	14
PL	2	0	111	0	2	33
CL1	89	0	0	87	41	0
CL2	10	5	4	54	169	45
CL3	0	0	28	2	67	81

(b) KDE

	NT	PS	PL	CL1	CL2	CL3
NT	406	3	1	33	6	0
PS	1	210	9	8	10	8
PL	0	1	114	1	9	23
CL1	92	0	0	81	43	1
CL2	4	5	8	46	182	42
CL3	0	1	30	0	67	80

thickness and genomic data were available (after the blind qualitative readings were completed).

The 342 CT scans were acquired at 16 sites hosting scanners by 3 vendors and a total of 9 specific models, namely: GE Light Speed 16, GE VCT 64, Siemens Definition, Siemens Definition AS+, Siemens Definition Flash, Siemens Sensation 64, Siemens Sensation 16 Philips 40 slice and Philips 64 slice.

3.3.2 Trainning set

A training set of ROIs for each tissue class was selected from a subset of 267 CT scans. In these scans, samples from the six classes under study were selected by an experienced pulmonologist by clicking on locations surrounded by the desired type of tissue, which after proper ROI extraction according to Subsect. 3.2.1 add up to a total of 1525 samples. This is one of the largest set of scans ever used for validation of texture approaches for emphysema detection. It is worth noting that, although all scans were acquired using standard reconstruction kernels (from different vendors) and acquisition parameters typical of chest imaging, no inter-site calibration or setup has been performed. See Table 3.1 for an exhaustive description of sample distribution across scan models.

Table 3.4: Reduced Classification Success

(a) LBPINT (Avg. Success 0.8134)

	NT	PS	PL	CL
NT	396	5	1	47
PS	2	202	12	30
PL	2	0	111	35
CL	99	5	32	546

(b) KDE (Avg. Success 0.8307)

	NT	PS	PL	CL
NT	406	3	1	39
PS	1	210	9	26
PL	0	1	114	33
CL	96	6	38	542

3.3.3 Parameter Selection

Most of the methodological parameters have been tuned according to previous findings. ROI size (24.18×24.18 mm^2), LBP parameters ($R = 1$, $P = 8$) and size of adaptive histograms ($N = 10$) have been chosen according to [84]. The intensity range for full histograms has been established according to the minimum and maximum intensity levels available in the complete dataset. The value of k for the *kNN* classifier was determined empirically to be optimal in terms of classification success for $k = 5$ when chosen among $k \in \{1,3,5,7,9\}$.

3.3.4 Leave-One-Subject-Out Sample Classification

We evaluate the performance of the proposed descriptions by leave-one-subject-out classification success estimation using the manually selected samples. We make a comparison for LBP histograms, Sørensen's LBPs (LBPINT), and full histograms reconstructed via adaptive binning (AB) and kernel density estimation (KDE) using $\mathscr{L}_1$. Finally we perform direct application of the EMD on sparse histograms. This results in 5 classification experiments. In each leave-out trial, all ROIs from one subject are held out and designated for testing, and subsequently, the ROIs in the test set are classified using all the remaining ROIs as prototypes in the classifier.

Several conclusion can be drawn from Table 3.2. Notice how when depriving LBPINT from the LBP component (thus transforming it into AB), we obtain a slight improvement in classification success, thus confirming our hypothesis of texture irrelevance (at least for our multi-scanner scenario). Furthermore, when a more refined technique (KDE) is employed, the local intensity-only part is even more discriminant.

In Table 3.3 we show the confusion matrix for the best method and the benchmark method. Notice how KDE performs better than LBPINT for most classes. Furthermore, if we group together CL1,2 and 3 into a single class CL, we obtain the classiffication success rates shown in Table 3.4.

Table 3.5: Confusion Matrix for Hierarchical Approach

	NT	PS	PL	CL1	CL2	CL3
NT	403	6	1	35	4	0
PS	10	160	19	0	34	23
PL	0	0	114	0	11	23
CL1	107	0	0	68	41	1
CL2	11	3	7	48	172	46
CL3	0	0	32	0	65	81

3.3.5 Full-lung analysis

For further validation we proceed by full-lung classification of 342 of the CT scans from the aforementioned workshop. As described in Subsect. 3.2.6, regularly sampling and classifying the lung field results in an approximation of the percentage of every tissue class for a given scan. The classification methods were computed at a fixed sampling grid with spacing $10 \times 10 \times 20$ pixels. The rest of voxels were classified using a nearest-neighbor interpolator.

We perform classification of the grid locations using the manually gathered samples (excluding those coming from the subject under study) according to our benchmark methodology [84] and to the developed methodology, that spares information concerning higher-order spatial statistics. In Fig. 3.12 we represent, for every tissue class, the percentage of ROIs that have been classified as belonging to that class for every CT scan. This is done for both methodologies in a two-dimensional plot. Regression lines are computed for every tissue class. The proximity of the obtained regressions to the identity function further demonstrates our conjecture of texture irrelevance. We systematically obtain results that are consistent with this state-of-the-art texture-including approach. In Fig. 3.13 we show the labelings obtained using both the benchmark methodology (LBPINT) and the propose method (KDE), over-imposed on the concerned CT slice. Although consistent between methodologies, these labelings systematically over-estimate the presence of PL in the proximity of the pleura across the lung fields. This happens for both methodologies, and although not discussed in [84], points to the fact that trying to detect PS using the presence of high-intensity pixels in the ROI results in PS over-estimation in the vicinity of high-intensity areas.

This problem does not arise in the leave-one-subject-out classification experiments, and this is probably due to the spatial incompleteness of the testing set of samples. Since most of the samples of classes different from PS are usually provided well inside the lung field, then we do not obtain many classification errors. When real lung fields are analyzed, many samples that occur near the pleura are classified as PS, only because they match the (high)-intensity pattern of the PS training samples. This clearly suggests that the conceptual nature of PS is not connected to only a given degree of tissue destruction, but also includes a notion of location.

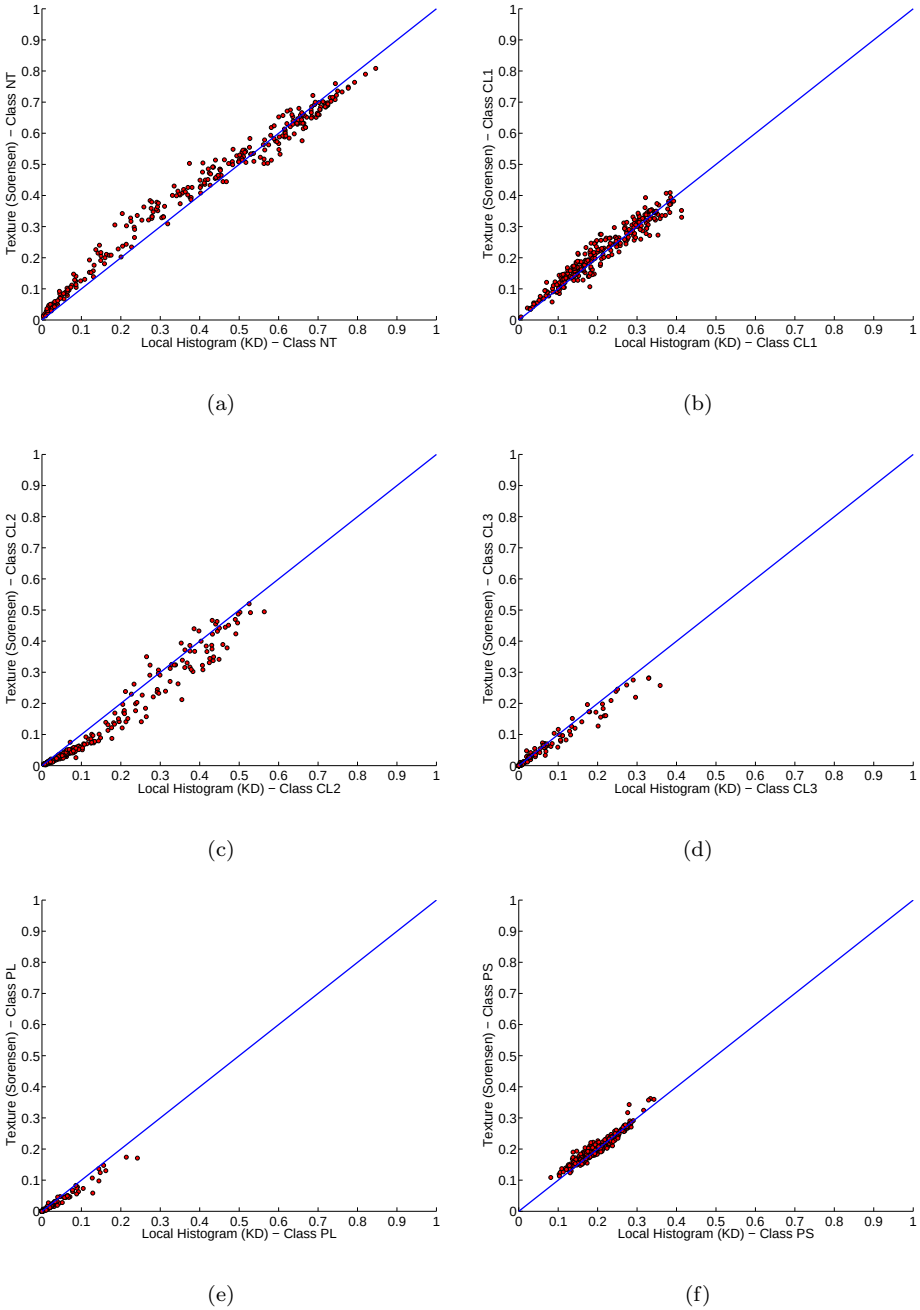

Figure 3.12: Scatter plot that shows the percentage of a given tissue class obtained using the texture-including benchmark methodology and out texture-free methodology. We obtain one point of the plot for every one of the 342 scans. (a) Healthy tissue. (b) Mild centrilobular emphysema. (c) Moderate centrilobular emphysema. (d) Severe centrilobular emphysema. (e) Panlobular emphysema. (f) Paraseptal emphysema

Figure 3.13: Classification results for three stages of disease severity using the methodologies under study. (Top row) axial and coronal slices for the original CTs. (Middle row) Classification results for KDE. (Botton row) Classification results using LBPINT (NT=red, CL1=yellow, CL2=cyan, CL3=purple, PL=blue, PS=green).

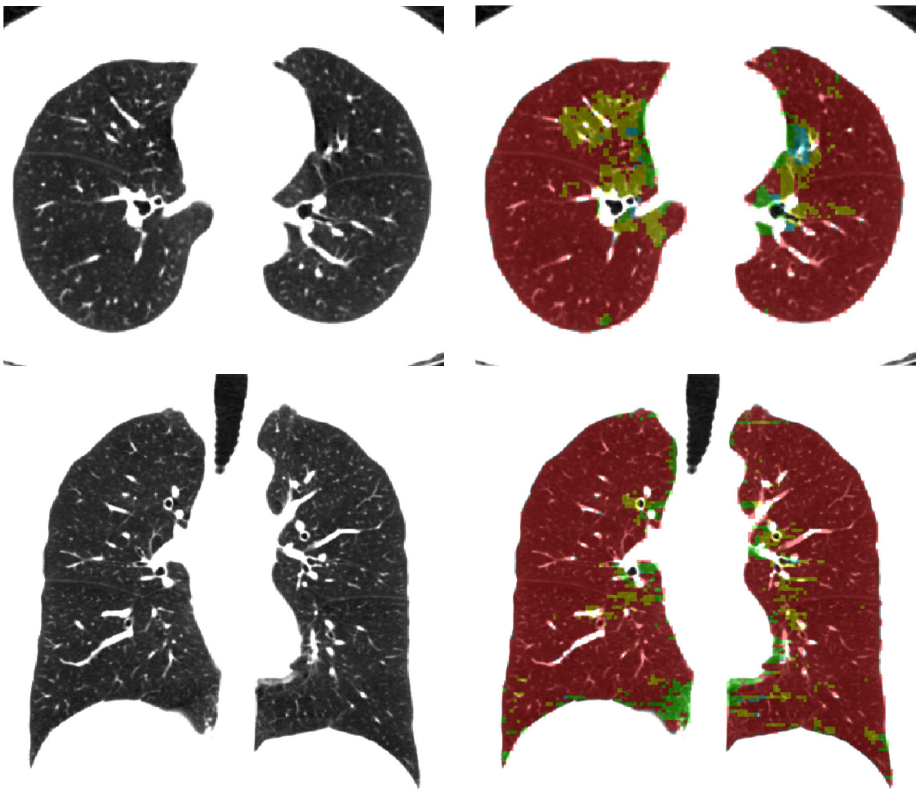

Figure 3.14: Classification results for the mild disease case shown in Fig. 3.13 using the KDE hierarchical approach.

Although pending for deeper study, this issue has been circumvented in the results following in this article. Since PS is defined as any kind of emphysema occurring near the pleura, we decided to adapt the range of intensity values for the histograms and retain only values below -650 HU. Since the problem of high-intensity prevalence affects only ROIs near the pleura, and by definition these ROIs can only be classified as NT or PS, then the classification success for reduced histograms is expected to be very close to that obtained using the full histogram. See Table 3.5 for the confusion matrix of this new approach.

Once the ROI has been classified into NT/CL1/CL2/CL3/PL, then if its low-intensity component gets classified as either CL1/CL2/CL3/PL, then if the percentage of high-intensity pixels surpasses the mean of this percentage for the PS training samples, it is classified as PS. Otherwise it is considered NT. This *ad hoc* adjustment results in worsening the classification success of class PS for the leave-one-subject-out experiment, since some of the testing samples contain high-intensity pixel percentages below the referred mean.

According to this new hierarchical strategy, we show in Figs. 3.14, 3.15 and 3.16 the labelings for two slices from three illustrative CT subjects with different disease severity. Clearly the issue of PS over-estimation is reduced, but will require further investigation. Apart from this, notice the spatial consistency in

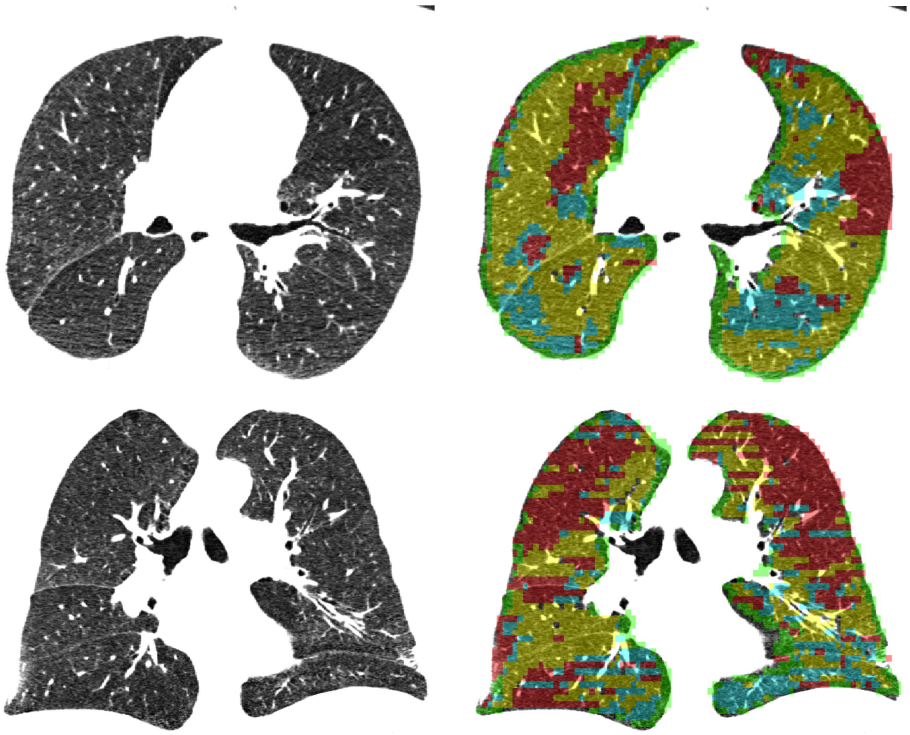

Figure 3.15: Classification results for the moderate disease case shown in Fig. 3.13 using the KDE hierarchical approach.

the class assignments with respect to Fig. 3.13.

To further validate the proposed approach, we compute the regression lines for scatter plots representing the percentage of a given tissue class versus lung function for every scan in the dataset. One such widely used lung function measures is LAA%. This quantity, deriving from traditionally preferred densitometric analysis, is the percentage of voxels in the lung field whose intensities lie under the commonly accepted threshold of -950 HU. We compute this indicator using the same lung masks as we did for the definition of the ROI grid used for quantifying the percentages of tissue classes according to our proposed methodology. LAA%, is known to correlate negatively with lung function measure FEV1% (Forced Expiratory Volume in 1 second), the most common of the Pulmonary Function Tests (PFTs) performed in ordinary emphysema diagnosis. It also correlates negatively with FEV1%-predicted, which is defined as FEV1% of the patient divided by the average FEV1%. In Fig. 3.17 we show tissue percentage versus LAA% in scatter plots for the six emphysema classes under study.

We proceed similarly for another CT-derived measure: Gas trapping percentage. Gas trapping (GT), is an abnormal retention of air in the lungs after expiration. It is observed in obstructive lung diseases such as asthma, bronchiolitis obliterants syndrome and chronic obstructive pulmonary disease, including emphysema. The cause is obstruction such that the patient is unable to expel air completely. Air trapping percentages can be obtained from expiratory CT scans

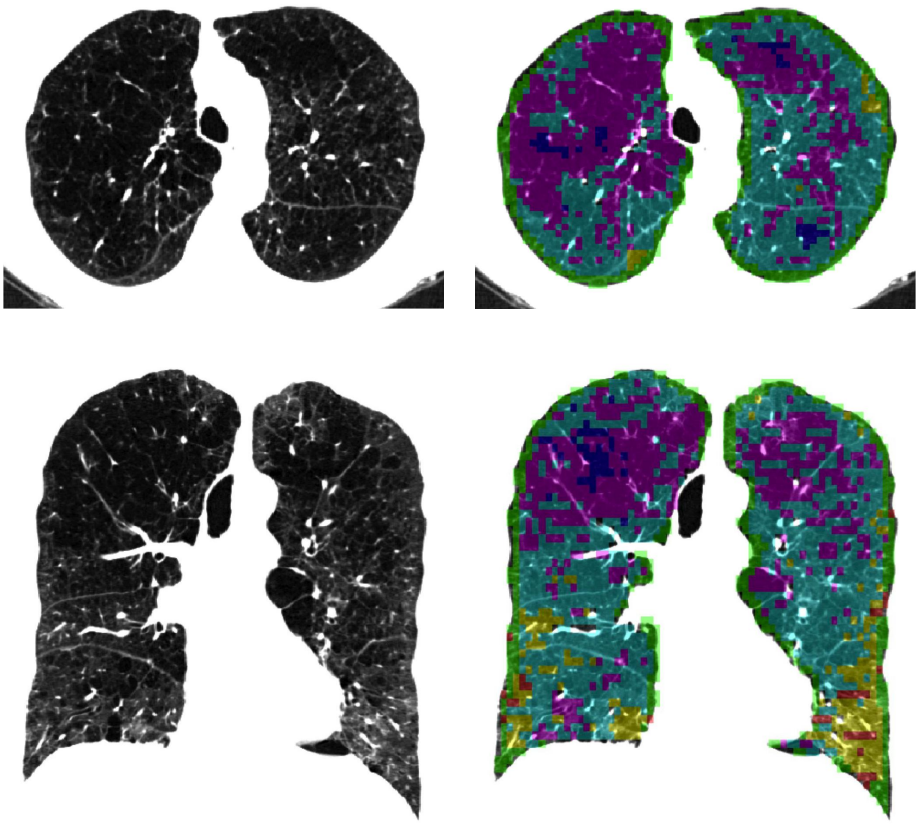

Figure 3.16: Classification results for the severe disease case shown in Fig. 3.13 using the KDE hierarchical approach.

by means of densitometry See in Fig. 3.18 how this image measure which is obtained from expiratory scans (all scans used for class percentage computations are inspiratory) correlates with our tissue percentages showing similar trends as those seen in Fig 3.17.

Finally, as the definitive validation of the obtained percentages, we present in Fig. 3.19 scatter plots for tissue percentages versus FEV1%-predicted itself. Notice that again the same trends arise, as long as the negative correlation between FEV1% and LAA% is kept in mind.

In all these plots, the same behavior can be outlined. Lung function correlates positively with the percentage of NT. It correlates positively (with a smaller slope) with percentages of CL1. For the rest of tissue percentages, the correlation is negative. More pronounced slopes occur for more severe medical conditions. For the percentages of PS the linear regression is also negative with a slope somewhere mid-way between CL2 and CL3. This behavior takes place consistently through different measures, in some cases even obtained from complementary scans (expiratory) not included in our study.

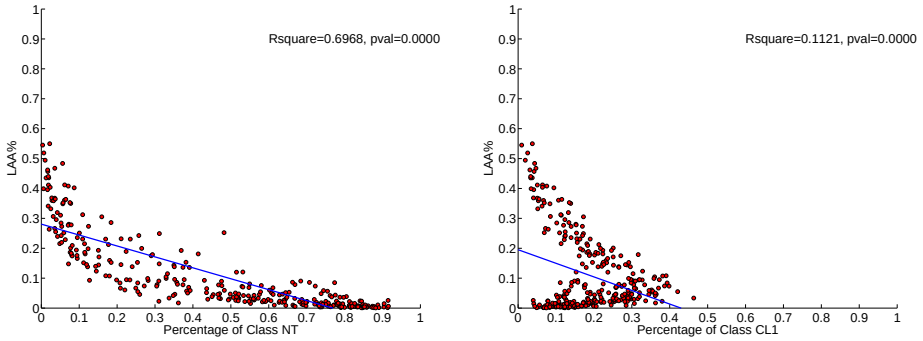

(a)

(b)

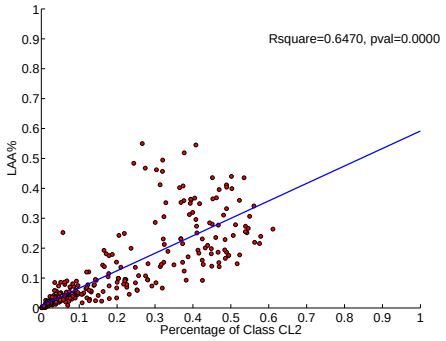

(c)

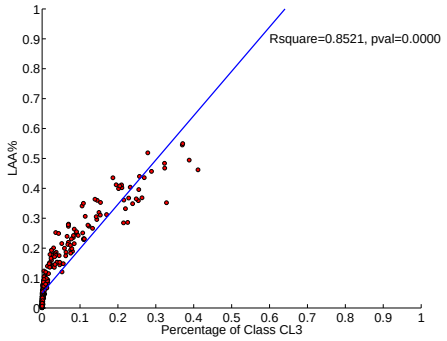

(d)

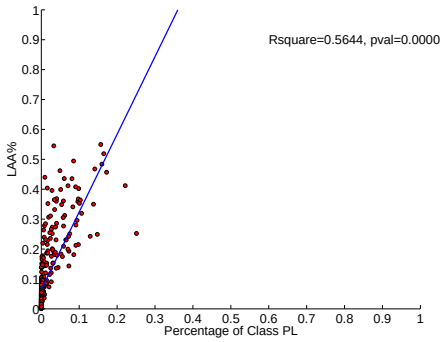

(e)

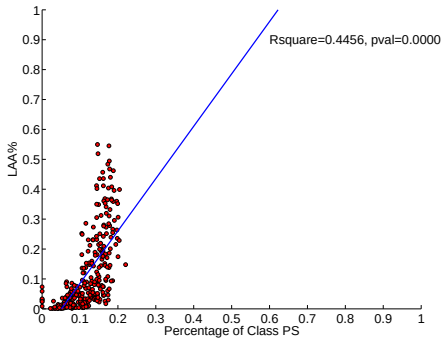

(f)

Figure 3.17: Scatter plot that shows the percentage of a given tissue class versus LAA%. We show one point for every one of the 350 scans. We show also the regression line for both measures. (a) Healthy tissue. (b) Mild centrilobular emphysema. (c) Moderate centrilobular emphysema. (d) Severe centrilobular emphysema. (e) Panlobular emphysema. (f) Paraseptal emphysema

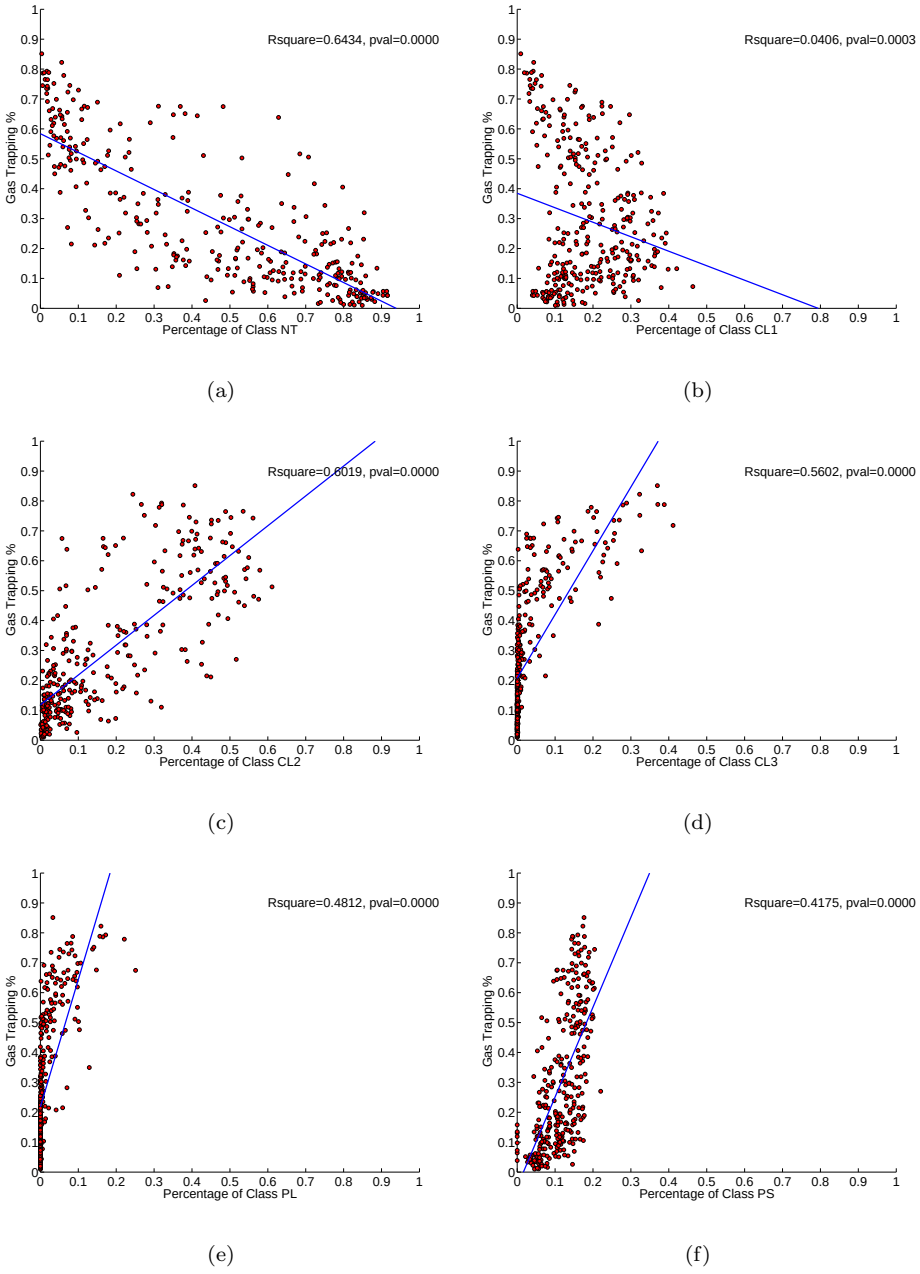

Figure 3.18: Scatter plot that shows the percentage of a given tissue class versus the GT percentage. (a) Healthy tissue. (b) Mild centrilobular emphysema. (c) Moderate centrilobular emphysema. (d) Severe centrilobular emphysema. (e) Panlobular emphysema. (f) Paraseptal emphysema

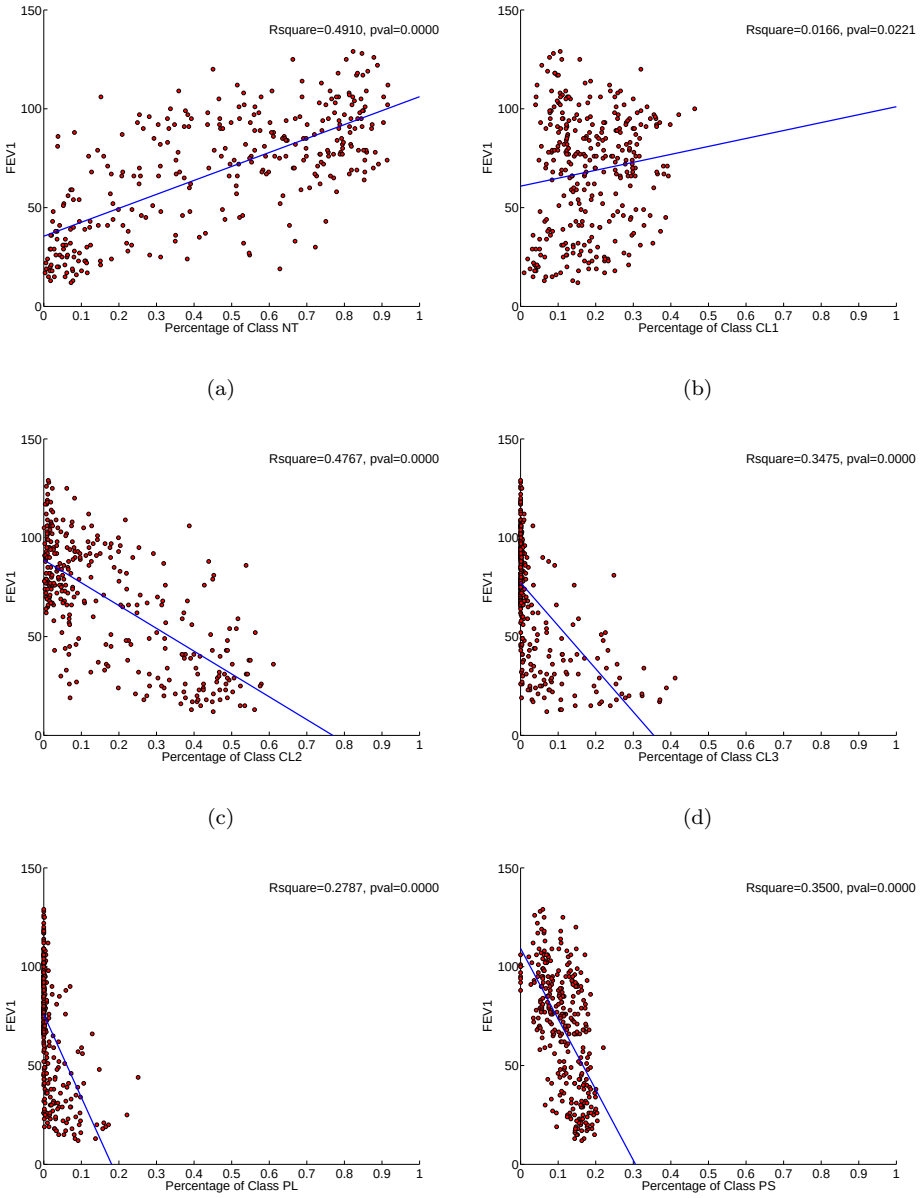

Figure 3.19: Scatter plot that shows the percentage of a given tissue class obtain using our methodology versus FEV1%. (a) Healthy tissue. (b) Mild centrilobular emphysema. (c) Moderate centrilobular emphysema. (d) Severe centrilobular emphysema. (e) Panlobular emphysema. (f) Paraseptal emphysema

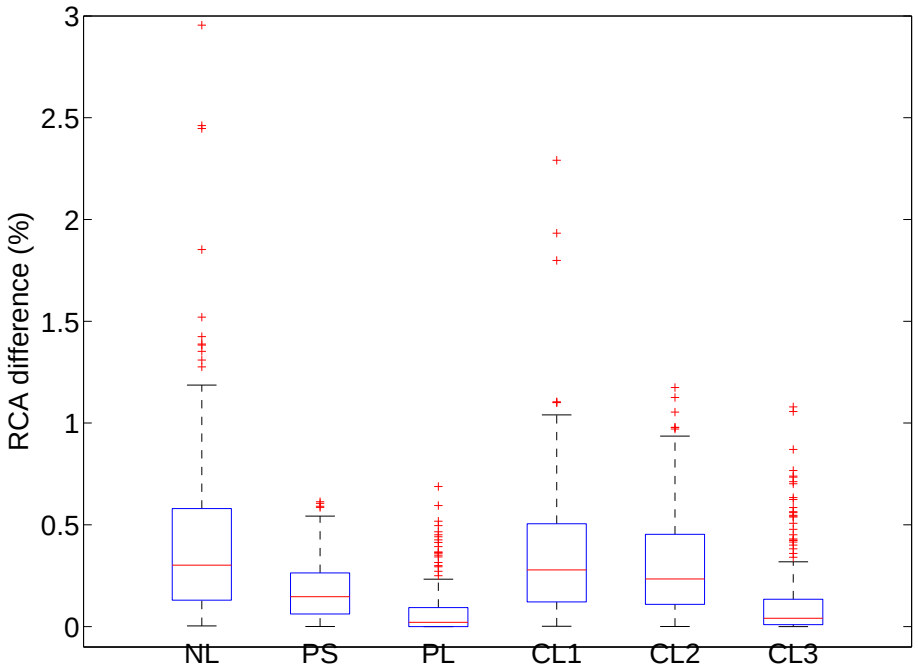

Figure 3.20: Difference in RCA scores for each tissue class between a high resolution and a low resolution sampling grid.

3.3.6 Sampling grid variability

A final set of experiments were carried out to assess the sensitivity of our classification algorithm to the underlying sampling grid that was chosen. Figure 3.20 shows box-plots for the RCA differences for each tissue class between the sampling grid that was used in our experiments ($10\times10\times20$ pixels) and a high-resolution sampling grid corresponding to $5\times5\times10$ pixels. The results show that the median difference is less than 1% for all the classes.

3.4 Conclusion

Under the light of our experiments we consider proven that the current gap between clinical-practice densitometry and impractical time-consuming texture analysis can be abridged by the use of local intensity distributions. The demonstrated approach is more intuitive, and since histogram sparsity is dealt with by non-parametric methods, it is well suited for emphysema analysis in complex multi-scanner scenarios like the one presented.

Although many authors have tried to study the characterization of emphysema patterns according to high-order spatial statistics of all sorts, many times the coupling of texture and intensity has obscured the true nature of emphysema ROIs.

It can be seen in our results, that new interesting lessons about emphysematous disease can be learnt using this simpler approach. And this can be done for hundreds or thousands of subjects in practical time-frames due to the technical simplicity of our technique, and its ability to deal with multi-scanner studies. We are already planning to do this with more than two thousand CT scans from the COPDGene cohort.

Ultimately, our technique is susceptible of being incorporated in clinical practice, once some minor aspect are taken care for, and further studies provide a model of the relation between tissue percentages and different PFTs or quality of life indicators. COPD patients can benefit from fully-automatic tissue percentage computations, which is much richer a description of the pulmonary condition than current densitometric approaches and can finely assess the response to therapy or the correlation with genetics.

Acknowledgment

This work has been supported by grants from University of Seville, Spain; and the National Institutes of Health (K25 HL104085 to Dr. San Jose Estepar; K23 HL089353, to Dr. Washko; U01 HL089897 and U01 HL089856, to COPDGene). The authors would like to thank to all the COPDGene Investigators for their contributions and the data that was used in the paper.

Chapter 4

Advances for CAD: Segmentation of Color Skin Images
Linearized Multi-dimensional Earth-Mover's-Distance Gradient Flows

4.1 Introduction

4.1.1 Active Contours and Energy Functionals

The success of any system aiming for computer-assisted detection and diagnosis of skin lesions depends strongly on the accuracy of lesion segmentation. This goal is pursued in our work in a framework of variational methods for image and video segmentation known as active contours. In active contour methods, a contour is usually associated with an energy that is minimal when the contour coincides with the real boundary of the segmented object. Widely used energy types depend on the smoothness of the boundary curve and on image features.

Image features may refer to the strength of edges, yielding edge-based active contours, or to the characteristics of the regions occupied by objects in the processed image, yielding region-based active contours.

The segmentation process starts with an initial contour obtained automatically or with the help of user interaction; this contour is evolved toward object boundaries under the action of forces derived from the energy, and energy minimization is often accomplished by gradient descent.

The first active-contour methods were edge-based. They used functionals that depended on the response of the image to an edge filter [100–105] such that the magnitude of motion forces derived from these functionals is small when the strength of the edge is large. Segmentation with an edge-based active contour is affected by problems of edge detectors. Weak or undetected perceptual edges cause an active contour to pass over real boundaries, while undesired strong edges stop the contour. Consequently, a classical drawback of edge-based active

contours is their small range of capture, which requires the initial contour to be placed in the close vicinity of objects to be segmented.

Intensity information gained from image regions delimited by a contour can be added to an edge-based energy functional in order to make active contours more robust [106, 107]; further results for energies based on a linear combination of edge and region terms can be found in [108] and [109]. Zhu and Yuille [110] assumed it to be sufficient to consider only the region information and designed a more general energy functional for the purpose of segmenting an image into regions.

4.1.2 Region Descriptors

For region-based energies, it is crucial to capture the information that best distinguishes between different objects. The information about a region is named region descriptor (in similarity with [111, 112]). An obvious region descriptor is one that characterizes the variation of color (intensity) within a region.

Recently, many other types of information have been included in the energy functional: a vector field, as the optical flow field [113, 114], motion detector output [115, 116], texture filter output [116–118], feature vector descriptors [119], shape similarity estimates [120, 121], or the geometry of the active contour [122].

Image features that describe a region usually vary within this region and the goal of a region descriptor is to formalize and measure the variation. This is commonly achieved by interpreting the varying values of a feature as realizations of a random variable with a probability density function (pdf) that needs to be determined. Some methods approximate region pdfs before the active contour segmentation is started: in [106, 108, 123], image intensities are modeled as a Gaussian mixture and its parameters are learned beforehand with an expectation maximization (EM) algorithm; in [124], the user selects image samples, thus making it possible to compute a mean and a variance for each region. Other methods [110, 125–127], approximate the parameters of the pdf at each evolution step, and for each region.

4.1.3 Histogram Distances

Arbitrary densities of real world objects can be approximated by nonparametric kernel density estimators (KDEs) [119, 128]. With an appropriate choice of kernel window width, nonparametric KDEs can describe the data closely, but because of this, new data points not present in the learning set may have low probabilities. When KDE is performed using the discrete Dirac delta function as kernel, then the resulting pdf is actually a histogram: a function relating sample values of a random variable with their sample frequencies. For details on KDE estimation see Sect. 3.2.3.2 in Chapter 3.

Two regions described nonparametrically may be compared in order to decide if they belong to the same object by computing a statistical divergence, like the Kullback-Leibler divergence or the Battacharya distance [129]. Both these pdf/histogram distance measures can be classified as bin-to-bin, in the sense that

only overlapping histogram locations discrepancies are considered. An alternative approach is using cross-bin histogram distance measures. Such measures explicitly incorporate the cost of elemental comparison between non-overlapping bins, so that not only bin-to-bin matching is performed, but also inter-bin simmilarities are considered.

One of the better trusted cross-bin distance measure available is Wasserstein Distance, also known as the Earth Mover's Distance (EMD) [94,130]. The EMD computes the dissimilarity of two distributions in terms of an optimization problem nuclear to the discipline of linear programming: the Monge-Kantorovich transportation problem [131]. Precisely, the EMD quantifies this dissimilarity as the amount of work needed to reconfigure one distribution into the other as if they were piles of dirt spread over space. If the elemental work required to move one unit of mass from one place to another (known as ground distance) is known, then an optimal way of performing this reconfiguration can be devised. Then, the EMD is the total work required to perform this optimal reconfiguration.

4.1.4 Histogram-Distance-Optimizing Gradient Flows

Development of gradient flows for histogram ditances require an explicit expression of the first variation of the distance with respect to contour variations, using calculus of variations. This was done for Bhattacharyya Distance and compared to Kullback-Leibler Divergence [132]. Although the EMD has been postulated to better correspond perceptual distribution comparison in the human visual system, its computation requires solving the transportation problem, and therefore the first variation with respect to the contour has no closed analytical expression. This is exceptionally false when dealing with one-dimensional distributions in which ground distances equal the distances between the corresponding bin locations. In that case an analytical solution for the EMD can be derived, and we obtain the expression for the so-called Match Distance [94]. The first variation of this expression is easily obtainable, allowing for EMD gradient flows when the above requirements are met. Concrete examples of this can be found in [133,134].

To this point, never a multi-dimensional EMD gradient flow has been envisaged. In this work, we will propose a framework for linearizing eventual solutions of the transportation problem so that an approximate gradient-descent equation for the evolving contour can be obtained. Using some results from [135], we will establish the sensitivity of multi-dimensional EMD against variations in the bin weights in multi-dimensional histograms of certain image feature.

Multi-dimensional histograms are often sparse representations of a random variable, especially as the number of dimensions grows. Introduced in [94] and further demonstrated in [136], the concept of signature comes into place in such situations. As opposed to histograms (fixed-size structures forcing a compromise between expressiveness and efficiency), a signature $\{s\} = \{s_u = (\vec{m}_u, w_u), u = 1 \dots N\}$ represents a set of feature clusters in space by cluster centroid ($\vec{m}_u$) and cluster relative mass (w_u). There are N clusters in this description, which can be obtained using any vector clustering technique, and the appropriate N itself can be estimated according to different cluster validity indexes. Notice that

histograms are a particular case of signatures where centroids feature space are evenly spaced. The reconcilement between expressiveness and efficiency in signature representations is necessary for the feasibility of our framework since the transportation problem to be solved at every gradient flow iteration depends on N with $O(N^3 \log N)$.

Either signatures or histograms can serve as the basis for the definition of energy functional depending on evolving contours. Such energies need to be derived from a given criterion that properly adjusts to the characteristics of the regions of interest for a certain segmentation problem. Maximal Discrepancy Criterion (MDC) energy is inversely proportional to the EMD between the distribution of features inside and outside the evolving contour [134]. Match-to-Template energy is proportional to the EMD between the pdf of a given image region and a predefined template. This criterion often requires the addition of balloon forces, whose relative influence is frequently difficult to tune, or alternatively the user might choose to stop the contour evolution as desired [134]. Another criterion, inspired by the Mumford and Shah functional [137], tries to minimize the discrepancy between local distributions as compared to a piecewise constant approximation of the image features [133].

Gradient descent can be performed either parametrically or implicitly. Parametric implementations compute a gradient descent equation for the evolving contour, and is dependent on parametrization of contours, in such a way that handling points may be a daunting task, especially when more image objects are to be detected or when the topology of the contour changes [100, 110, 138, 139]. The level-set method introduced by Osher and Sethian [140] is an alternative that can deal with these issues easily. The level-set method has thus become a very popular method for numerically evolving curves in the direction of their normal. By this paradigm, an evolving curve $C(t)$ can be embedded as the zero-level set of a function ϕ:

$$C(t) = \{(x,y) | \phi(x,y,t) = 0\} \quad \text{with} \quad \phi(x,y,0) = C_0 \ , \tag{4.1}$$

where C_0 is the initial curve. ϕ is very often a signed distance function taken to be positive on the inside and negative outside of the curve, or viceversa. The outward normal $\vec{n}$ of C and its curvature κ can be expressed in terms of the gradient $\nabla\phi$ of the new function. Then, under this representation, evolving a contour according to a force that acts in the normal direction is equivalent to the following level-set function gradient descent partial differential equation:

$$\phi_t = F|\nabla\phi| \ . \tag{4.2}$$

4.1.5 Contributions

In this work we provide the analytical framework allowing multi-dimensional EMD gradient flows. Also, one-dimensional arbitrary-ground-distances EMD gradient flows will be possible for the first time. We will provide analytical expressions for a maximal discrepancy criterion energy definition and will establish the relations between EMD, signature shape and contour evolution via calculus

of variations. This will require sensitivity analysis of the transportation problem in the space of feature signatures obtained from clustering of the features available in the image. Hierarchical application of the maximal discrepancy criterion will also be explored. Finally we will expose results obtained for the segmentation of natural images and images of the skin. Our implicit implementation is subsceptible of being solved using fast level-set evolution techniques (i.e. discrete-valued level-set functions). Experimental results will be compared with bin-to-bin distance gradient flows, precisely those based on the Bhattacharyya Distance [132]. We will prove several advantages (better convergence to global extrema, better perceptual significance) of using properly defined cross-bin histogram matching for evolving active contours.

4.2 Methods

4.2.1 The Transportation Problem

In this work we formulate the EMD in the context of comparisons between feature distributions that take values in certain regions left inside/outside (I/O) by the evolving contour. Considering histograms as a particular case of signatures, the EMD between distributions can be defined in terms of centroid locations and weights as long as a set of ground distances is available.

We consider signatures $s^I = \{s_u\}_{u=1,\ldots,N}$ and $s^O = \{s_v\}_{v=1,\ldots,N}$, each determined by a set of N cluster centroids and their relative weight as defined in Subsect. 4.1.4. Ground distances $\{d_{uv}\}_{u=1,\ldots,N,v=1,\ldots,N}$ need to be chosen between every pair of centroid locations, usually deriving from some distance metric between the locations. Computing the EMD requires devising an optimal mass transportation scheme, for varying mass flows $\{f_{uv}\}_{u=1,\ldots,N,v=1,\ldots,N}$ going from cluster u in s^I to cluster v in s^O, in terms of the available ground distances $\{d_{uv}\}$, for each of the N^2 combinations of centroids u and v in both signatures. Then, the optimal total work implied in the reconfiguration is the EMD between the two signatures.

Formally put, the optimization problem can be written as:

$$\mathrm{EMD}(s^I, s^O) = \operatorname*{argmin}_{f_{uv}} Z(f_{uv}, d_{uv}) \ , \tag{4.3}$$

where Z, as defined in [94], meets the following expression:

$$Z(f_{uv}, d_{uv}) = \sum_{u=1}^{N} \sum_{v=1}^{N} d_{uv} f_{uv} \ , \tag{4.4}$$

subject to the following constraints:

$$f_{uv} \geq 0,\ 1 \leq u \leq N, 1 \leq v \leq N \ , \tag{4.5}$$

$$\sum_{u=1}^{N} f_{uv} = w_v,\ 1 \leq v \leq N \ , \tag{4.6}$$

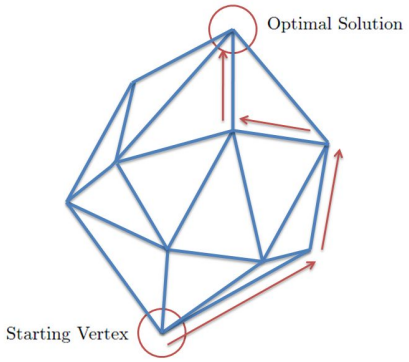

Figure 4.1: An illustration of the simplex method.

$$\sum_{v=1}^{N} f_{uv} = w_u,\ 1 \leq u \leq N \ , \tag{4.7}$$

$$\sum_{u=1}^{N}\sum_{v=1}^{N} f_{uv} = 1 \ . \tag{4.8}$$

The meaning of these constraints is immediate. A direction of mass transference must be chosen, for example from I to O, such that flows are positively defined in that direction. All the mass flowing from/into a bin must be equal to the initial/final available mass in that bin. The total mass being transported equals the mass of both normalized signatures.

4.2.2 Simplex Method and EMD Sensitivity Analysis

The above linear programming problem can be considered in geometric terms as finding an optimum in a closed convex polytope. In the problem presented in this work, the polytope is defined by intersecting $2N+1$ half spaces in an N^2-dimensional euclidean space. As illustrated in Fig. 4.1, the simplex method [141] essentially works by searching the vertices on the boundary of the polytope for an optimum. The simplex algorithm begins at a starting vertex and moves along the edges of the polytope until it reaches the vertex of the optimum solution.

Sensitivity analysis aims to obtain the derivatives of the optimum flows with respect to each of the variables on the right-hand side (RHS) of the constraints. Such derivatives allow for obtaining the sensibility of $Z(f_{uv}, d_{uv})$ with respect to the variations in the weights in 4.6 and 4.7, using 4.4 and the chain rule of derivatives. Intuitively, changing the RHS changes the intercept of the boundary lines. In the following, we express the linear programming problem in a matrix form and retrieve sensitivity analysis of the simplex method from [135].

Z	$\vec{f}_B$	$\vec{f}_{NB}$	RHS
1	$-(\vec{d}_B^T)^{(S)}$	$-(\vec{d}_{NB}^T)^{(S)}$	0
$\vec{0}$	$(\mathbf{H}_B)^{(S)}$	$(\mathbf{H}_{NB})^{(S)}$	$(\vec{b})^{(S)}$

Table 4.1: Starting Tableau

4.2.2.1 Simplex Method in Matrix Form

To perform the sensitivity analysis, the problem in 4.3 is first represented in a matrix form. The starting matrix is then transformed to an optimal form based on the simplex algorithm so that the change of EMD with respect to the changes of the cluster weights are expressed in an explicit way.

Specifically, since there are N^2 variables f_{uv} and N^2 constants d_{uv} in 4.4, we use column vectors $\vec{f}$ and $\vec{d}$, both of size N^2, to represent the set of flows and the ground distances as

$$\vec{f} = [f_{11} \cdots f_{1N} \cdots f_{N1} \cdots f_{NN}]^T \ ,$$

$$\vec{d} = [d_{11} \cdots d_{1N} \cdots d_{N1} \cdots d_{NN}]^T \ .$$

Stacking the first three equations of the equality constraints in 4.6, 4.7 and 4.8, the coefficients c_{uv} $(1 \le u \le N, 1 \le v \le N)$, which are either 0 or 1, can form a 2D matrix of $2N+1$ rows and N^2 columns. If

$$\mathbf{H} = \begin{pmatrix} c_{11} & 0 & \cdots & 0 & \cdots & c_{N1} & 0 & \cdots & 0 \\ & & & & \vdots & & & & \\ 0 & \cdots & 0 & c_{1N} & \cdots & 0 & \cdots & 0 & c_{NN} \\ c_{11} & & \cdots & c_{1N} & \cdots & 0 & & \cdots & 0 \\ & & & & \vdots & & & & \\ 0 & & \cdots & 0 & \cdots & c_{N1} & & \cdots & c_{NN} \\ c_{11} & & \cdots & c_{1N} & \cdots & c_{N1} & & \cdots & c_{NN} \end{pmatrix} \ ,$$

and

$$\vec{b} = [w_1^O \cdots w_N^O w_1^I \cdots w_N^I 1]^T \ ,$$

then we can obtain a matrix form of 4.4 as

$$\underset{\vec{f}}{\operatorname{argmin}} \, Z = \vec{d}^T \vec{f} \ , \tag{4.9}$$

subject to

$$\mathbf{H}\vec{f} = \vec{b} \ , \tag{4.10}$$

$$\vec{f} \ge \vec{0} \ . \tag{4.11}$$

According to the Simplex algorithm, since there are N^2 variables and $2N+1$ constraints in the problem, we can always formulate $2N+1$ basic variables (i.e.

Z	$\vec{f}_B$	$\vec{f}_{NB}$	RHS
1	0	$-\vec{d}_{NB}^T + \vec{d}_B^T \mathbf{H}_B^{-1} \mathbf{H}_{NB}$	$\vec{d}_B^T \mathbf{H}_B^{-1} \vec{b}$
$\vec{0}$	$\mathbf{I}$	$\mathbf{H}_B^{-1} \mathbf{H}_{NB}$	$\mathbf{H}_B^{-1} \vec{b}$

Table 4.2: Reformulated Optimal Tableau

variables of nonzero value), and $N^2 - (2N+1)$ nonbasic variables. Grouping all of the basic variables together and all of the nonbasic variables together, we split the flow vector $\vec{f}$ into $[\vec{f}_B^T \ \vec{f}_{NB}^T]^T$ where the subscript B denotes basic variables, and NB is for nonbasic variables. The ground distance vector $\vec{d}$ is similarly divided as $[\vec{d}_B^T \ \vec{d}_{NB}^T]^T$ and $[\mathbf{H}_B \ \mathbf{H}_{NB}]$. Thus the Simplex starting tableau is written as in Table 4.1. In this table, RHS denotes the right-hand side of the equations. The second row corresponds to the objective function of 4.9, and the third row is a vector representation of the constraints in 4.10 and 4.11. The superscript S denotes starting tableau.

Applying the simplex algorithm yields an optimal tableau, where the sets of basic variables and nonbasic variables change, and so are all their coefficients. After matrix transformations [135], the optimal tableau can be reformulated as shown in Table 4.2. This reformulated optimal tableau is important for the sensitivity analysis, as will be discussed shortly.

4.2.2.2 Sensitivity Analysis

Based on the reformulated optimal tableau, we analyze the sensitivity of the EMD to a change in the cluster weights of the signature. Note that sensitivity analysis is performed both on the w^I and the w^O parts, i.e., the cluster weights corresponding to the signature inside/outside of the contour.

From the second row of Table 4.2, we have $Z = \vec{d}_B^T \mathbf{H}_B^{-1} \vec{b}$. Let $\vec{b}$ be changed to $\vec{b}'$, where $\vec{b}' = \vec{b} + [0 \ldots 0 \Delta w_i^{I/O} 0 \ldots 00]^T$, i.e. one of the weights changes while the rest remain the same. Then

$$\begin{aligned} Z' = \vec{d}_B^T \mathbf{H}_B^{-1} \vec{b}' &= \vec{d}_B^T \mathbf{H}_B^{-1} \vec{b} + \vec{d}_B^T \mathbf{H}_B^{-1} [0 \ldots 0 \Delta w_i^{I/O} 0 \ldots 00]^T \\ &= \vec{d}_B^T \mathbf{H}_B^{-1} \vec{b} + k_i \Delta w_i^{I/O} \quad , \end{aligned} \tag{4.12}$$

$$\text{where } k_i = \sum_{l=1}^{2N} (\vec{d}_B)_l (\mathbf{H}_B^{-1})_{li} \quad , \tag{4.13}$$

$$i = 1, \ldots, 2N \quad . \tag{4.14}$$

Therefore,

$$\frac{\partial Z}{\partial w_v^O} = \lim_{\Delta w_v^O \to 0} \frac{\Delta Z}{\Delta w_v^O} = \frac{k_v \Delta w_v^O}{\Delta w_v^O} = k_v, \quad v = 1, \ldots, N \quad , \tag{4.15}$$

$$\frac{\partial Z}{\partial w_u^I} = \lim_{\Delta w_u^I \to 0} \frac{\Delta Z}{\Delta w_u^I} = \frac{k_{u+N} \Delta w_u^I}{\Delta w_u^I} = k_{u+N}, \quad u = 1, \ldots, N \quad . \tag{4.16}$$

This takes care of the change of Z due to EMD sensitivity. To incorporate the effect of subsequent normalization -as the sum of the cluster weights of either one of the signatures is 1- let us incorporate the change of weight in one cluster as the weights of the other clusters in the same signature change. Considering this constraint leads [135] to

$$\frac{\partial Z}{\partial w_v^O} = k_v - \sum_{j \neq v} k_j \frac{w_j^O}{\sum_{j \neq i} w_j^O}, \quad v = j = 1, \ldots, N \ , \tag{4.17}$$

$$\frac{\partial Z}{\partial w_u^I} = k_{u+N} - \sum_{k \neq u} k_{k+N} \frac{w_k^I}{\sum_{j \neq i} w_k^I}, \quad u = k = 1, \ldots, N \ . \tag{4.18}$$

4.2.3 Multi-dimensional EMD Gradient Flows

4.2.3.1 Maximal Discrepancy Criterion

A common criterion for segmenting with distributions is the Maximal Discrepancy Criterion (MDC), as was in fact the basis of the methodology in [134]. For a given contour, this criterion establishes an energy E inversely proportional to the EMD between the feature signatures inside (I) and outside (O) the contour,

$$E = -\text{EMD}(s^I, s^O) \ . \tag{4.19}$$

Minimization of this energy is equivalent to the following optimization problem

$$\underset{\phi(\vec{x})}{\text{argmax}} \ \text{EMD} \ , \tag{4.20}$$

where the contour is embedded as the zero level-set of the function $\phi(\vec{x})$ defined over the image domain Ω. For a given signature pair, we can model the variations of EMD with respect to the signature weights by linearizing the optimal Z and using $\frac{\partial Z}{\partial w_i}$ according to 4.17 and 4.18. The optimization problem becomes

$$\underset{\phi(\vec{x})}{\text{argmax}} \ \underset{f_{uv}(\phi(\vec{x}))}{\text{argmin}} \ Z(f_{uv}(\phi(\vec{x})), d_{uv}) \ , \tag{4.21}$$

and the derivative of the EMD with respect to the signature weights will be approximated for every eventual signature pair after solving the linear programming problem:

$$\frac{\partial \text{EMD}}{\partial w_u^I} \simeq \frac{\partial Z_{\min}}{\partial w_u^I} \ , \tag{4.22}$$

$$\frac{\partial \text{EMD}}{\partial w_v^O} \simeq \frac{\partial Z_{\min}}{\partial w_v^O} \ . \tag{4.23}$$

Then we can use the chain rule to write an expression of the first variation of the EMD with respect to ϕ,

$$\frac{\delta \text{EMD}}{\delta \phi} = \sum_{u=1}^{N} \frac{\partial \text{EMD}}{\partial w_u^I} \cdot \frac{\delta w_u^I}{\delta \phi} + \sum_{v=1}^{N} \frac{\partial \text{EMD}}{\partial w_v^O} \cdot \frac{\delta w_v^O}{\delta \phi} \ . \tag{4.24}$$

If $H(\cdot)$ is the Heaviside function, and $\phi(\vec{x})$ is positive/negative for $\vec{x}$ inside/outside the contour, we can write the signature weights in terms of $\phi(\vec{x})$ as

$$w_u^I(\phi(\vec{x})) = \frac{\int_\Omega C_u(\vec{x})H(\phi(\vec{x}))d\vec{x}}{\int_\Omega H(\phi(\vec{x}))d\vec{x}} \ , \tag{4.25}$$

$$w_v^O(\phi(\vec{x})) = \frac{\int_\Omega C_v(\vec{x})(1-H(\phi(\vec{x})))d\vec{x}}{\int_\Omega (1-H(\phi(\vec{x}))d\vec{x}} \ , \tag{4.26}$$

where $C_i(\vec{x})$ charts the membership of $\vec{x}$ to the i-th cluster in the signature:

$$C_i(\vec{x}) = \begin{cases} 1 & \text{if } \vec{x} \in s_i \\ 0 & \text{otherwise} \end{cases} \ . \tag{4.27}$$

Following [112] it is immediate to determine the first variation of the weights with respect to ϕ

$$\frac{\delta w_u^I}{\delta \phi} = -\frac{|\nabla(\phi)|}{A_I}\left(w_u^I - C_u(\vec{x})\right) \ , \tag{4.28}$$

$$\frac{\delta w_v^O}{\delta \phi} = \frac{|\nabla(\phi)|}{A_O}\left(w_v^O - C_v(\vec{x})\right) \ . \tag{4.29}$$

Notice $A_{I/O}$ are the areas of the regions left inside/outside of the contour. Finally, the contour evolution minimizing the energy can be obtained combining 4.19, 4.24, 4.28 and 4.29 to produce the first variation of the enrgy E with respect to ϕ, and plugging the result into a gradient descent scheme:

$$\begin{aligned} \phi_t = -\frac{\delta E}{\delta \phi} = \frac{\delta \text{EMD}}{\delta \phi} = \frac{|\nabla(\phi)|}{A_O}\sum_{v=1}^{N}\left(w_v^O - C_v(\vec{x})\right)\frac{\partial \text{EMD}}{\partial w_v^O} \\ - \frac{|\nabla(\phi)|}{A_I}\sum_{u=1}^{N}\left(w_u^I - C_u(\vec{x})\right)\frac{\partial \text{EMD}}{\partial w_u^I} \ . \end{aligned} \tag{4.30}$$

This gradient descent of ϕ affects its zero-level set according to the following contour evolution [125]:

$$\frac{\partial C}{\partial t} = F\vec{N} \ , \tag{4.31}$$

where

$$\begin{aligned} F = \frac{1}{A_O}\sum_{v=1}^{N}\left(w_v^O - C_v(\vec{x})\right)\frac{\partial \text{EMD}}{\partial w_v^O} \\ - \frac{1}{A_I}\sum_{u=1}^{N}\left(w_u^I - C_u(\vec{x})\right)\frac{\partial \text{EMD}}{\partial w_u^I} \ , \end{aligned} \tag{4.32}$$

and $\vec{N}$ stands for the contour's normal. This force will minimize energy E as long as we solve the linear programming problem for every time $t = t_0 + \Delta t$ in the discretization of the gradient descent equation, and update the values of $\frac{\partial \text{EMD}}{\partial w_u^I}$ and $\frac{\partial \text{EMD}}{\partial w_v^O}$ according to 4.22 and 4.23.

4.2.3.2 Hierarchical Maximal Discrepancy Criterion

As will be outlined in the following Section, sometimes the maximal-discrepancy functional does not capture a perceptually meaningful region of the image. In some cases the object of interest does not hold maximal discrepancy with the rest of the image and the gradient flow will tend to undersegment the object. This will especially be the case when the object's distribution is multimodal and one of the modes hold greater similarity to the distribution of the background than to the other modes in the distribution of the object.

For this eventuality we have designed a heuristic approach that can handle scenarios where these circumpstances occur. Its underlying assumption is that once maximal discrepancy has led to undersegmented objects the excluded part of the object is itself in maximal discrepancy with the background. This gives rise to a hierarchical approach in which the object can be fully segmented by iterative application of the maximal discrepancy criterion.

For a given undersegmented object O_i, the hierarchical maximal discrepancy criterion is applied to a special signature we will refer to as *remainder* signature. As the contour evolves and signature weights are updated in every iteration, the inside signature will be estimated from samples inside the contour, excluding samples inside O_i. Then, the whole region will be described as if this partial signature was the fully-computed one. The result of the maximal discrepancy criterion will then be O_{i+1}.

This process can be repeated until the user is satisfied with the resulting region. The suitability of our assumption will be validated in the following Section.

4.2.4 Contour Regularization

From the viewpoint of statistical estimation, the energy functional 4.19 can be thought of as accounting for the fidelity of estimation of the optimal level-set function to observed features in the enclosed regions. However, this cost function does not take into consideration some plausible properties of the optimal solution, and, as a result, minimizing 4.19 alone could be too sensitive to measurement noises and/or errors in the data. In order to alleviate this sensitivity, one can attempt to filter out the spectral components of the solution which belong to the noise subspace. For the case at hand, one can regularize the solution via constraining the length of the active contour [100], in which case the energy functional is given by

$$E = -\text{EMD}(s^I, s^O) + \mu\,\text{Length}(C) \quad , \tag{4.33}$$

where $\mu > 0$ is a regularization constant, which controls the compromise between fidelity and stability. Translating this into the level-set framework leads to the following optimization problem:

$$\underset{\phi(\vec{x})}{\text{argmax}} \left(\text{EMD}(\phi) - \mu \int_\Omega |\nabla H(\phi)| d\vec{x} \right) \quad . \tag{4.34}$$

The gradient flow associated with minimizing the cost functional in 4.34 can be

shown [125] to be equal to

$$\phi_t = \frac{\delta \mathrm{EMD}}{\delta \phi} - \mu \kappa |\nabla \phi| \ , \tag{4.35}$$

where κ is the contour curvature and meets

$$\kappa = \nabla \cdot \left(\frac{\nabla \phi}{|\nabla \phi|} \right) \ . \tag{4.36}$$

This is equivalent to contour evolution in the normal direction according to the force

$$F_{\mathrm{reg}} = F - \mu \kappa \ . \tag{4.37}$$

4.3 Experiments

It is our intention in this Section to provide some experimental evidence on the main advantages of our method. The main contribution of our work is the possibility of evolving active contours according to gradient flows that tend to optimize the widely preferred cross-bin histogram distance measure known as EMD. Although this concept had already been addressed [133, 134], only one-dimensional histograms were made available for active contour segmentation.

Cross-bin EMD has already been proven to better correlate with perception [94, 130], and in particular EMD gradient flows have been compared with bin-to-bin Bhattacharyya gradient flows [132], like in [134], where gray-level histograms are segmented under both paradigms.

Similarly we intend to make an analogous comparison for the case of natural color images, for which EMD active contours are unprecedented due to the three-dimensional nature of color.

Bhattacharyya gradient flows as presented in [132] are readily applicable to distributions in any dimensions expressed either as histograms or as signatures. Bhattacharyya distance does not account for any cross-bin interactions and therefore makes comparisons in a per-bin basis. Let us reproduce here for convenience the basic equations concerned.

Bhattacharyya distance maximization in the level-set formulation, brought into the signature description notation, is equivalent to the following optimization problem,

$$\underset{\phi(\vec{x})}{\operatorname{argmin}} \, \tilde{B}(\phi(\vec{x})) = \underset{\phi(\vec{x})}{\operatorname{argmin}} \sum_{i=1}^{N} \sqrt{w_i^I w_i^O} \ , \tag{4.38}$$

given that Bhattacharyya distance $B = -\log \tilde{B}$. Then, the contour evolution in the normal direction producing the gradient descent for such optimization corresponds [132] to the following force

$$F(\vec{x}) = -\frac{\tilde{B}}{2} \left(A_I^{-1} - A_O^{-1} \right) - \frac{1}{2} \left(A_O^{-1} \sqrt{\frac{\vec{w}^O \cdot \vec{C}(\vec{x})}{\vec{w}^I \cdot \vec{C}(\vec{x})}} - A_I^{-1} \sqrt{\frac{\vec{w}^I \cdot \vec{C}(\vec{x})}{\vec{w}^O \cdot \vec{C}(\vec{x})}} \right) \ , \tag{4.39}$$

where

$$\vec{C}(\vec{x}) = [C_1(\vec{x}), \ldots, C_N(\vec{x})]^T \ , \tag{4.40}$$

$$\vec{w}^{I/O} = [w_1^{I/O}, \ldots, w_N^{I/O}] \ . \tag{4.41}$$

Again, we can add a length regularizer, with positive sign this time since this is a minimizing scheme,

$$F_{\text{reg}} = F + \mu\kappa \ . \tag{4.42}$$

4.3.1 Modelization of Color Images

To illustrate the properties of our novel gradient flows, we propose a segmentation scenario previously untreatable with EMD (one-dimensional) gradient flows: color images. Image color is usually represented as a three-component vector after the tri-stimulus theory of human vision that models the frequency response of the three types of cone cells available in the human retina [142]. Several representation spaces have been devised including *RGB*, *HSV*, $L^*u^*v^*$ and $L^*a^*b^*$.

1976 CIE $L^*a^*b^*$ (CIELAB or *Lab* for simplicity) color space was designed according to perception experiments in a way such that Euclidean distances are proportional to the perceived simmilarity between colors [143]. Therefore, in a cross-bin simmilarity scheme like the one proposed it makes sense to work in a space where bins are layed out in a perceptually meaningful manner.

CIELAB values do not define absolute colors unless the white point is also specified. To work in the CIELAB color space we transform color images using the CIE standard illuminant D50 [144].

Although three-dimensional histograms can be constructed directly from the *Lab* components, this approach gives place to a tight compromise between expressiveness and efficiency. Bigger volumetric bins allow for a reduction of sparsity at the cost of reduced resolution in feature space. To circumvent this difficulty we propose the use of signatures, which, as outlined in Section 4.1.4, consists of translating the histogram into a set of clusters represented by their centroid and relative mass .

Clustering of the feature space is therefore necessary for signature construction. Many techniques for supervised and unsupervised clusterization are available in the literature. Here, we choose to make use of supervised k-means clustering [145], i.e. Euclidean-distance k-means with a an empirically fixed number of clusters. Then the EMD ground distances between cluster centroids - i.e. the work needed to transfer one unit of mass from one cluster to another - are made equal to their Euclidean distance in perceptually-uniform color space *Lab*.

We provide an example of color image modelization in Fig. 4.2. Notice how the signature representation conveys the color content of the image.

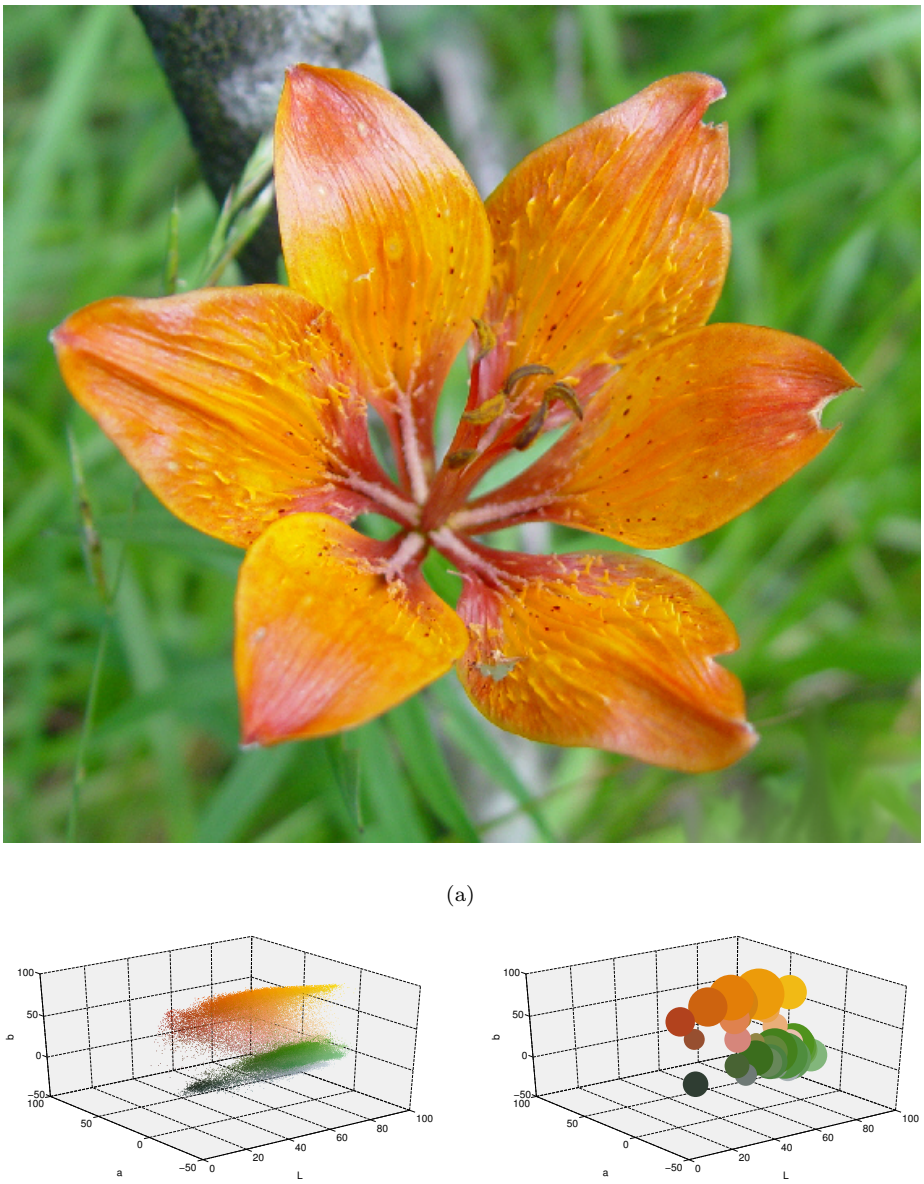

Figure 4.2: Example of color image modelization. (a) Original image. (b) Color distribution in *Lab* space. (c) Signature for $N = 30$.

4.3.2 Implementation

Since the bottleneck of our methodology occurs iteratively at EMD computation, we decided appropriate to make use of an approximate fast level-set framework to save time in the computation of the level-set function evolution once EMD sensitivity has been computed.

There has been numerous efforts to simplify gradient flow algorithms so that fast, discrete implementations become available [146–148]. We prefer the well-validated methodology in [147], mainly founded on the usage of integer values for the level-set function and move-in/move-out operations according to the sign of the force obtained from Eq. 4.32.

Due to the difficulty of approximating second-order derivatives of contour shape by discrete level-set functions, a separate approach is used for the length regularizer, which evolves with the curvature. The idea of using convolution operations to generate mean curvature motion was originally proposed by Merriman et al in their work on diffusion generated mean curvature motion [149]. In [147], this idea is further pursued. Their solution is to approximate curvature diffusion by convolving the characteristic function (binarization of the regions inside/outside of the contour) with Gaussian kernels and thresholding the result. As Gaussian σ becomes smaller, the approximation is better. This smoothing behavior, arising from approximations performed for computational efficiency, is different than what one obtains from standard level-set-based curvature motion. However, they argue that this thresholded type of smoothing regularization is actually more desirable in many practical image processing applications because it only eliminates small structures with high curvature while leaving coarse scale structures intact. For implementation details please see [147].

4.3.3 Maximal Discrepancy Results

We will now analyze some of the advantages introduced by the proposed technique. We will benchmark results in terms of state-of-the-art bin-to-bin Bhattacharyya gradient flows, analyzing the main benefits derived from cross-bin distance maximization for multi-dimensional features (color). Image segmentation using EMD has been explored for one-dimensional features in [133, 134].

Both methods will share the same model and approximative implementation. We will choose a fixed number of clusters $N = 30$ in *Lab* space. For the EMD case, ground distances will equal Euclidean distance in feature space.

We will compare results for synthetic/natural images, with different initializations (assisted and generic) under both schemes. For our proposed framework, we will study the influence of the weight of the regularizer and the number of clusters in the model. This will serve as a justification of the presented techniques. Later on, in Section 4.3.4, we will study the application of MDC and Hierarchical MDC (HMDC) to color images of the skin with the goal of lesion segmentation.

4.3.3.1 Comparison with Bhattacharyya Gradient Flows

In this first experiment we want to highlight the main advantages introduced by color EMD segmentation as compared to bin-to-bin Bhattacharyya segmentation. In Figs. 4.3-4.10 we show results for synthetic/natural images, initialized with a rectangle overlapping the object of interest (assisted initialization) or with a generic pattern of circular regions. For the referenced figures, $N = 30$ and the regularizer is implemented via Gaussian filtering of the characteristic

function ($\sigma = 3$). In all these examples we show the image under study, the signature of the whole image, the signature configuration for the initial contour and the final contours under both techniques, and two graphs showing EMD and B variation as the contour evolves both for EMD or Bhattacharyya methodologies.

Notice that EMD active contours produce better segmentations when maximal discrepancy takes place between the object and the background. See for example Figs. 4.3, 4.4 and 4.9. Despite misleading initializations, EMD active contours find a way towards maximal discrepancy regions reachable from the initial contour, and staying subject to the regularizer.

Bhattacharyya active contours suffer from the presence of more local extrema and get stuck in them often. We have conducted an experiment in which the 'Blue Flower' image is segmented by both methods using different initializations (grid of $N \times N$ evenly spaced circles with $N = 1, 2, \ldots 5$) and no regularizer (so that only EMD maximization effect is displayed). The standard deviation of final EMD value for varying initializations with our method was 0.0076 and the average overlap between solutions was 99.97%, and for the benchmark method the standard deviation of B was 0.2326 and the average overlap was 45.11%.

The reason for this profusion of local extrema, is that Bhattacharyya active contours do not *see* the location of the clusters but only consider the overlap of their weights, in a bin-to-bin manner. This suboptimality is more of a handicap when initialization is provided far away from the object of interest, as is the case for Figs. 4.5, 4.8, 4.9, and 4.10. This idea demonstrated by graphing the variation of B and EMD as both contours evolve. EMD active contours most often maximize B and EMD, better than Bhattacharyya active contours. EMD contours always find their way in feature space. The reason is that they incorporate information on the location of clusters.

The ultimate evidence can be gathered from observation of feature space configuration of cluster pertenence for both methodologies. Notice how EMD final configurations show much higher consistency in the space of features (although always subject to the initialization and regularization). On the other hand, B contours display no feature space consistency, again due to their ignorance about cluster location. This becomes most obvious for synthetic images, as in Figs. 4.6 and 4.10.

Even in cases where the maximal discrepancy criterion is meaningless (there is no connection between color discrepancy and semantics), like in Fig. 4.7, this consistency can be appreciated for EMD contours. At the same time, consistency in image space is imposed by the initialization (and the fact that level set evolution is approximated only on the contour), and by the regularizer.

4.3.3.2 Influence of the Regularizer

To illustrate the penalization set on contour length, we provide in Fig. 4.11 an example segmentation with varying regularization degree. Notice how contour length is reduced as the variance of the Gaussian filter is increased, at the cost of maximum EMD attained. As the regularizer gains weight in the optimization problem, the EMD part of the optimization suffers, and shorter contours occur.

4.3.3.3 Influence of the Number of Clusters

The number of cluster has critical importance in the performance of the algorithms. The computation of EMD sensitivity in every evolution iteration takes place with complexity $O(N^3 \log N)$ where N is the number of clusters in the signature. On the other hand, higher numbers for N result in closer representations of the underlying color distribution.

In Fig. 4.12 we provide segmentations for the 'Crayons' image with varying number of signature clusters. We use the same regularizer as for Figs. 4.3-4.10. Notice how, for a precise initialization over the orange part of the image, as the number of clusters increases the contour is more selective for the desired hues. When the number of clusters is too low, the underlying distribution is not faithfully conveyed, and therefore the contour is not capable of telling the difference between the different tints.

From all the results presented it seems obvious that bigger signatures allow precise color discrimination at the cost of greater computational expense.

4.3.4 Results on Skin Images

To further validate our technique we provide here some interesting results in application to skin lesion segmentation.

Images of skin lesions are usually pretty well suited to the maximal discrepancy paradigm. They usually display healthy skin as the background, and the object of interest exhibits some distinguishable color. In such cases MDC is enough to obtain lesion delineation for subsequent quantification (not addressed in this Chapter).

For some other cases (particularly for melanocytic or pigmented lesions), there might be several colored regions inside the lesion, usually showing some kind of radial simmetry in their distribution. For these cases, we have found useful for the time being, to apply hierarchical-MDC (H-MDC) as described in Sect. 4.2.3.2.

In Fig. 4.13 we provide segmentation initialization and MDC result for 15 images of skin lesions of different types. Notice we highlight the initial and final contours in red and green respectively. These results were obtained with the same regularizer as used for images in Figs. 4.3-4.10. $N = 10$ was chosen for signatures, since skin images display less variety of colors as compared to other natural images.

In Fig. 4.15 we include segmentations using H-MDC for the same set of parameters, with application to images of melanocytic skin lesions, which will be quantified in the following Chapter. The original images are provided in Fig. 4.14 for clarity.

See the initial contour in red and results for each iteration of H-MDC as green contours growing towards the outside of the lesion. As H-MDC is applied iteratively, results approach the desired contours. The exterior green contours are taken as final segmentation for all the lesions.

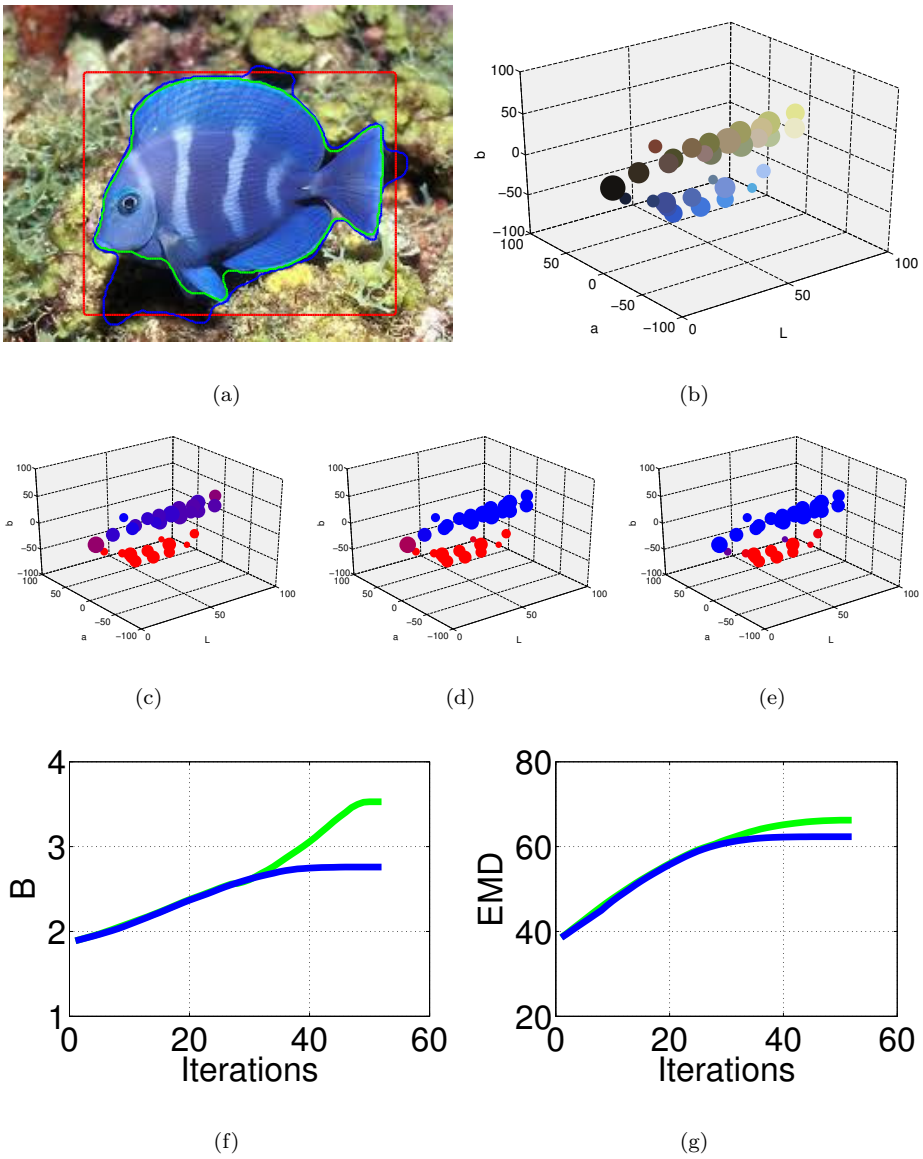

Figure 4.3: Segmentation for 'Blue Fish' Image. (a) Original image with contours overimposed (Red: Initialization, Blue: Bhattacharrya final contour, Green: EMD final contour). (b) Color distribution in *Lab* space. (c) Distribution inside (red) and outside (blue) the initial contour. Intermediate colors indicate partial pertenence. (d) Distribution inside/outside Bhattacharyya final contour. (e) Distribution inside/outside EMD final contour. (f) Evolution of Bhattacharyya Distance $B = -\log \tilde{B}$ as initial contour evolves under both schemes. (g) Evolution of EMD as initial contour evolves under both schemes.

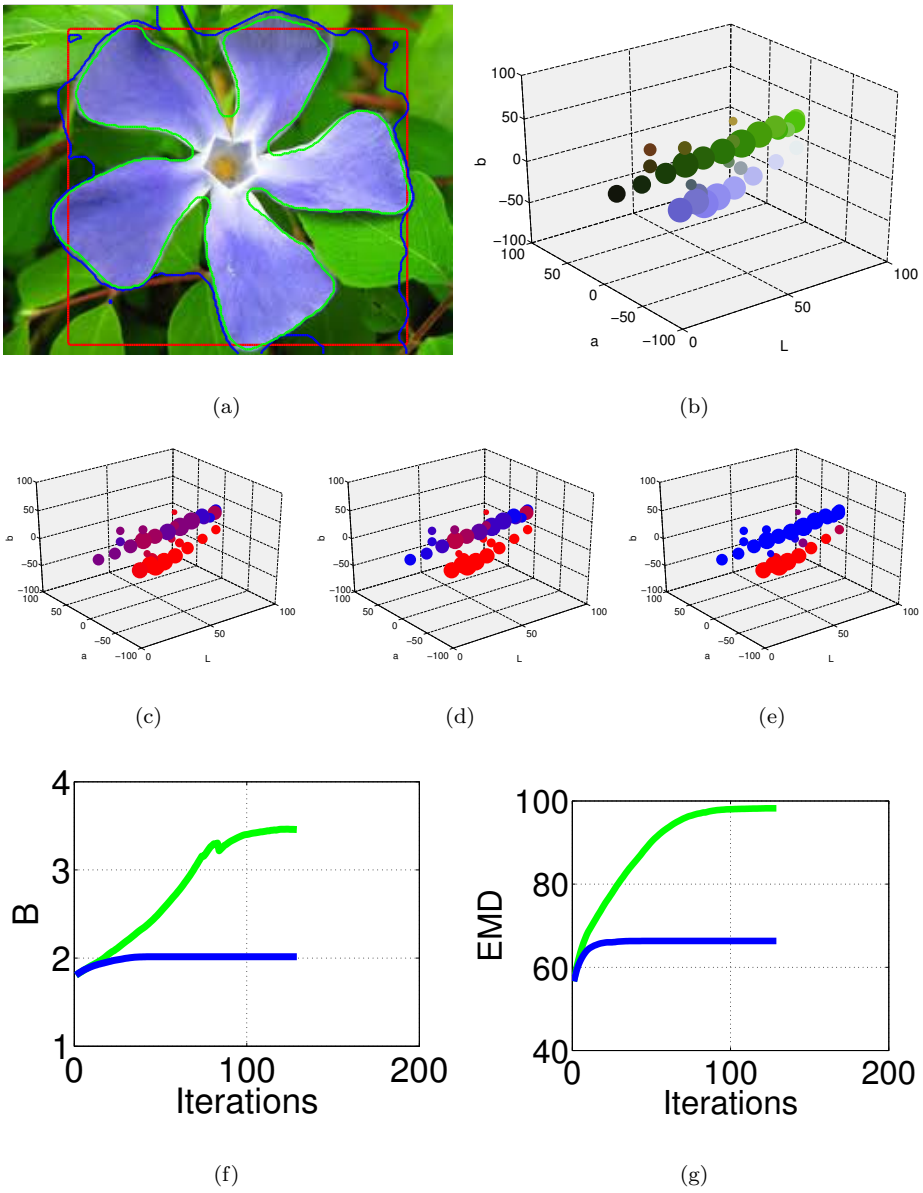

Figure 4.4: Segmentation for 'Blue Fish' Image. (a) Original image with contours overimposed (Red: Initialization, Blue: Bhattacharrya final contour, Green: EMD final contour). (b) Color distribution in *Lab* space. (c) Distribution inside (red) and outside (blue) the initial contour. Intermediate colors indicate partial pertenence. (d) Distribution inside/outside Bhattacharyya final contour. (e) Distribution inside/outside EMD final contour. (f) Evolution of Bhattacharyya Distance $B = -\log \tilde{B}$ as initial contour evolves under both schemes. (g) Evolution of EMD as initial contour evolves under both schemes.

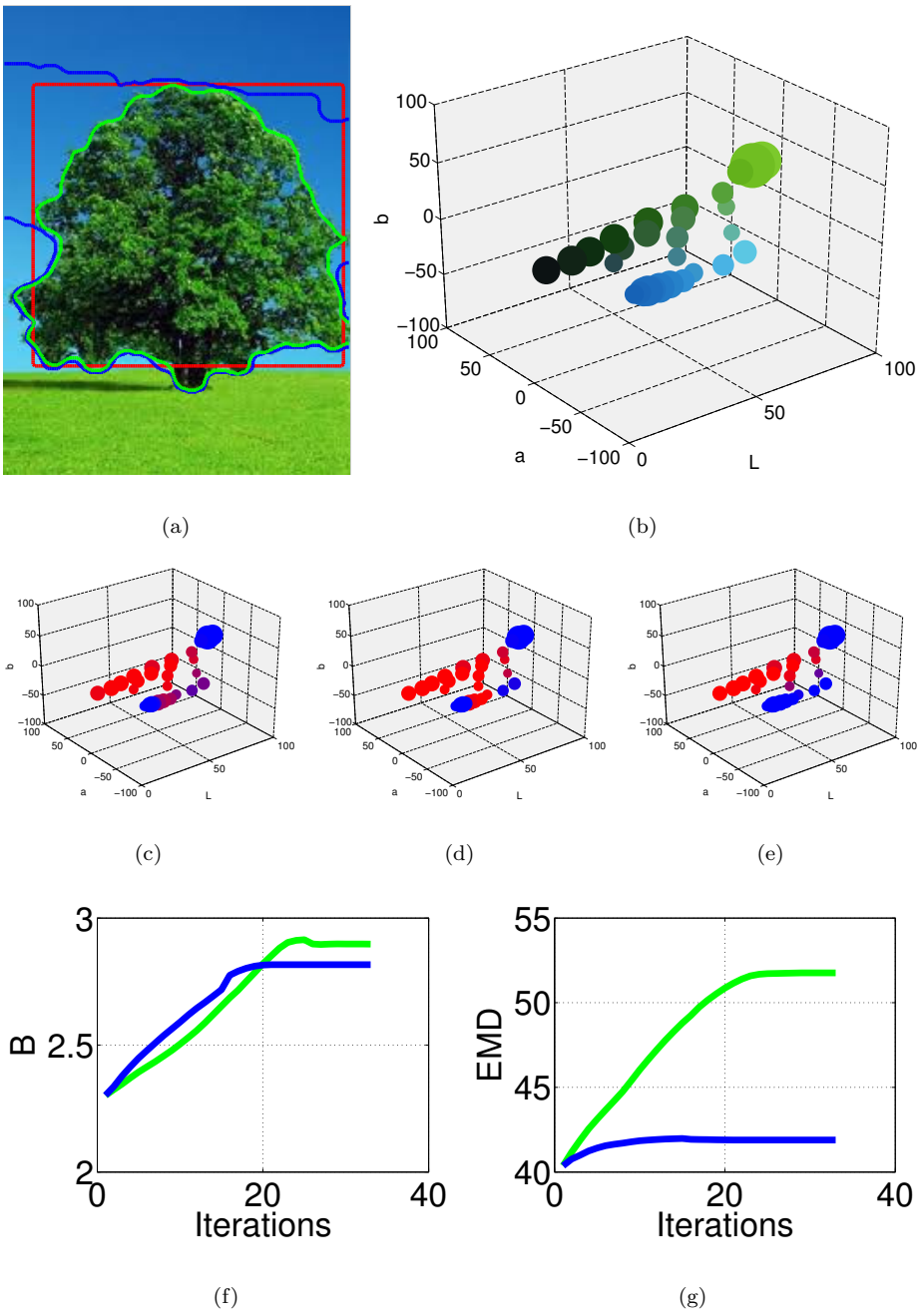

Figure 4.5: Segmentation for 'Tree' Image. (a) Original image with contours overimposed (Red: Initialization, Blue: Bhattacharrya final contour, Green: EMD final contour). (b) Color distribution in *Lab* space. (c) Distribution inside (red) and outside (blue) the initial contour. Intermediate colors indicate partial pertenence. (d) Distribution inside/outside Bhattacharyya final contour. (e) Distribution inside/outside EMD final contour. (f) Evolution of Bhattacharyya Distance $B = -\log \tilde{B}$ as initial contour evolves under both schemes. (g) Evolution of EMD as initial contour evolves under both schemes.

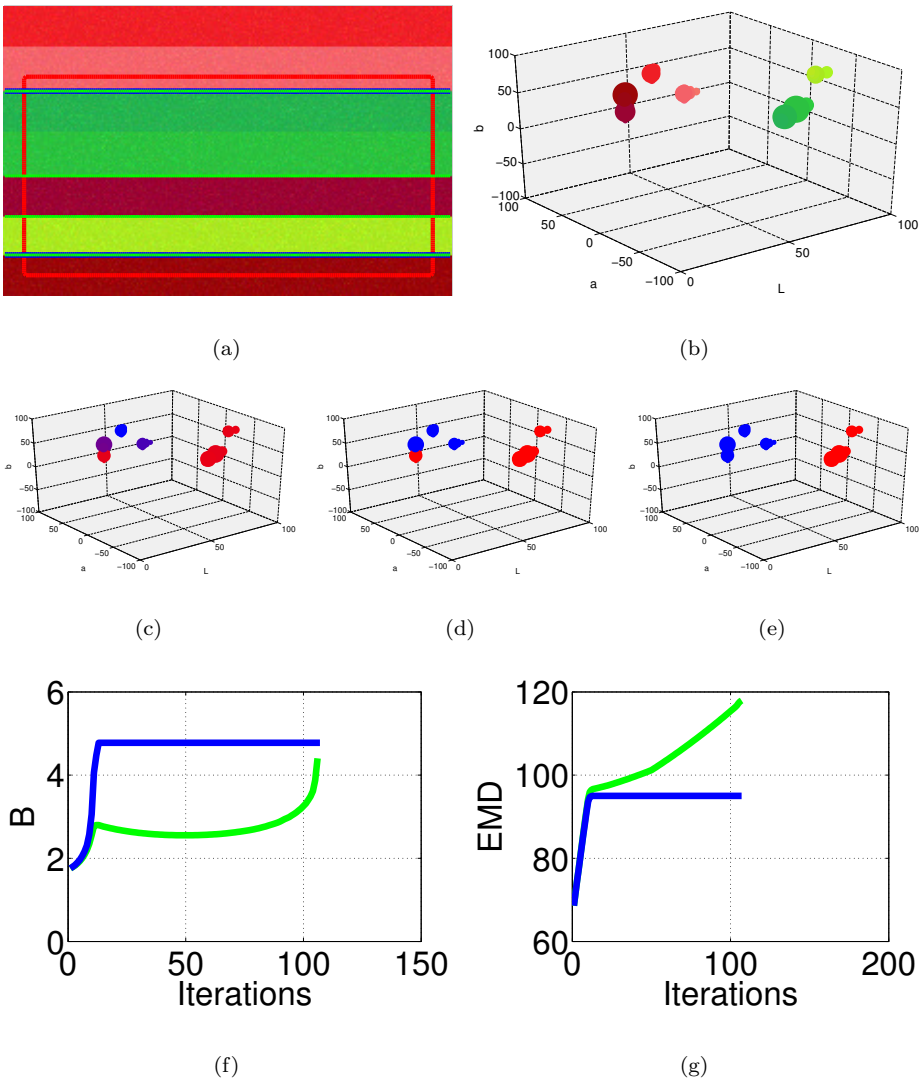

Figure 4.6: Segmentation for 'Stripes' Synthetic Image. (a) Original image with contours overimposed (Red: Initialization, Blue: Bhattacharrya final contour, Green: EMD final contour). (b) Color distribution in *Lab* space. (c) Distribution inside (red) and outside (blue) the initial contour. Intermediate colors indicate partial pertenence. (d) Distribution inside/outside Bhattacharyya final contour. (e) Distribution inside/outside EMD final contour. (f) Evolution of Bhattacharyya Distance $B = -\log \tilde{B}$ as initial contour evolves under both schemes. (g) Evolution of EMD as initial contour evolves under both schemes.

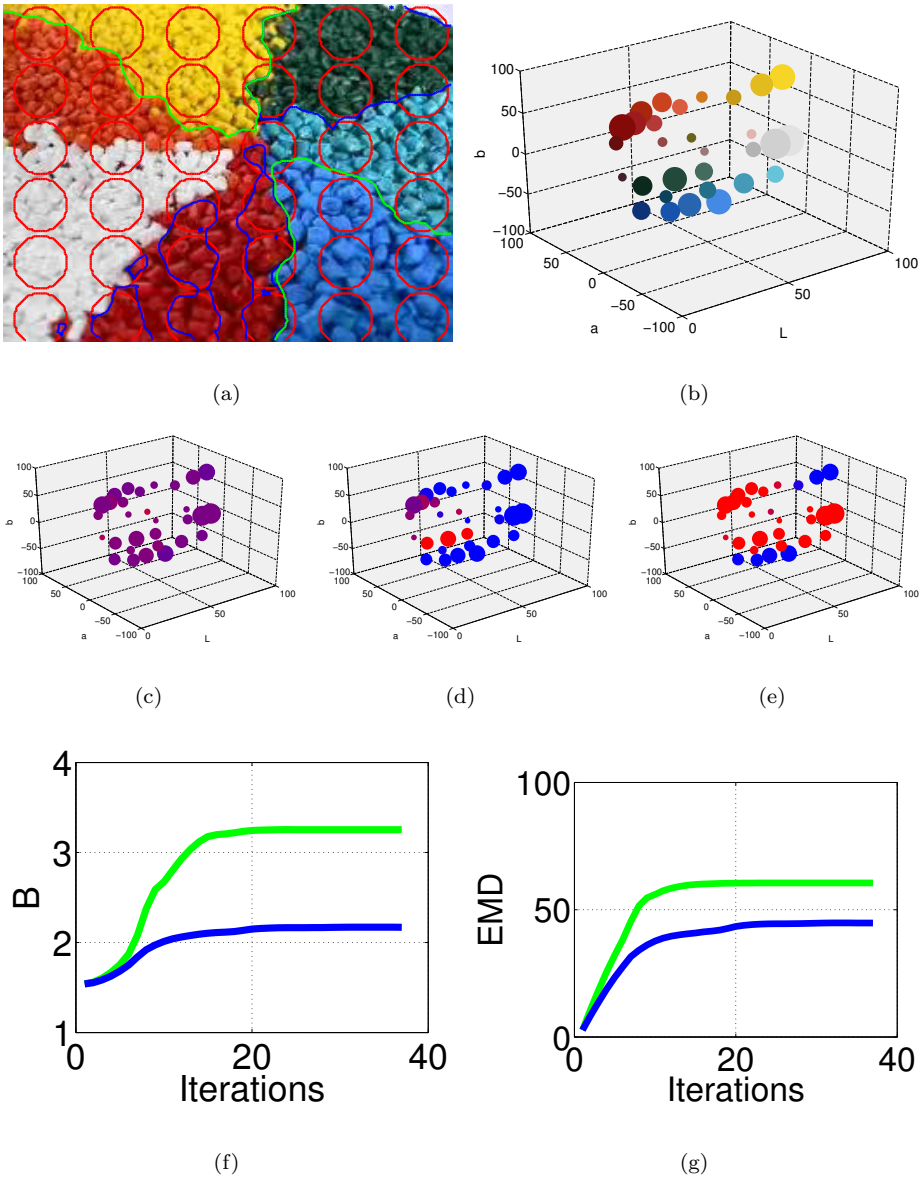

Figure 4.7: Segmentation for 'Cobbles' Image. (a) Original image with contours overimposed (Red: Initialization, Blue: Bhattacharrya final contour, Green: EMD final contour). (b) Color distribution in *Lab* space. (c) Distribution inside (red) and outside (blue) the initial contour. Intermediate colors indicate partial pertenence. (d) Distribution inside/outside Bhattacharyya final contour. (e) Distribution inside/outside EMD final contour. (f) Evolution of Bhattacharyya Distance $B = -\log \tilde{B}$ as initial contour evolves under both schemes. (g) Evolution of EMD as initial contour evolves under both schemes.

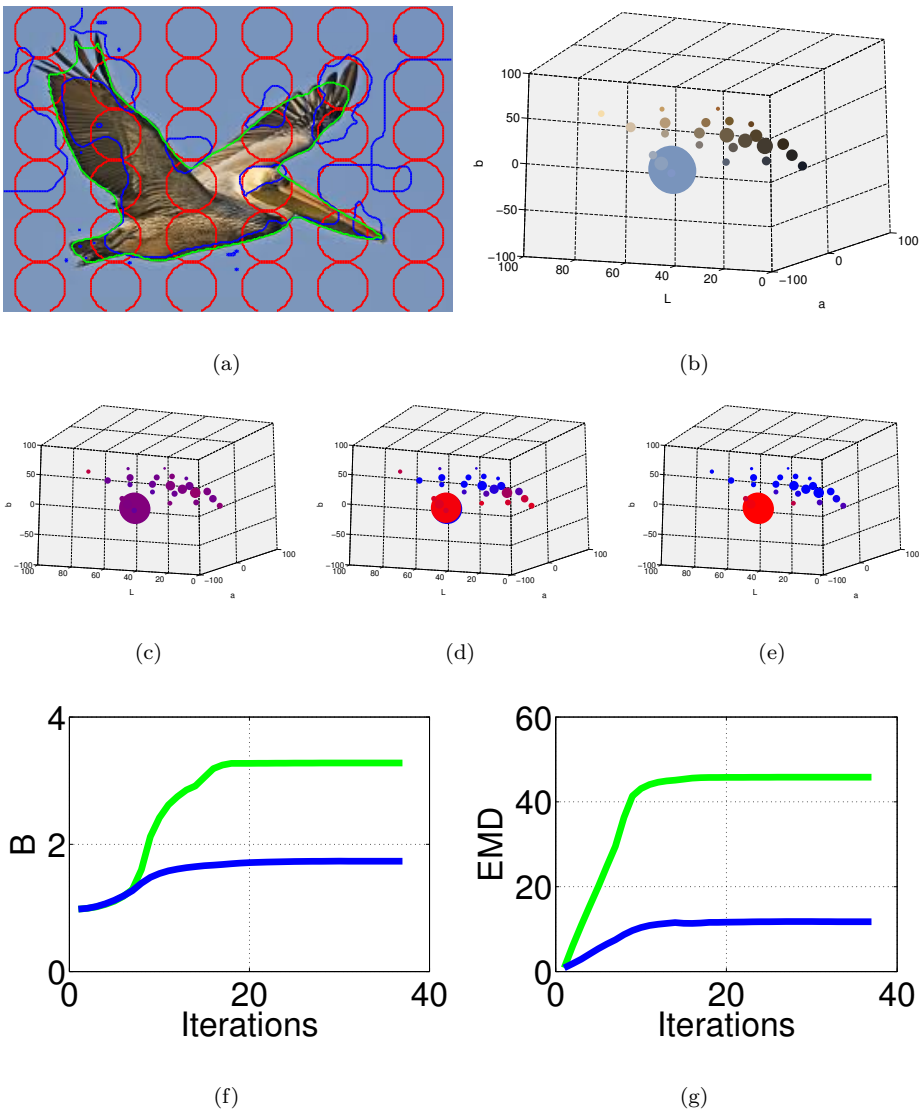

Figure 4.8: Segmentation for 'Pelican' Image. (a) Original image with contours overimposed (Red: Initialization, Blue: Bhattacharrya final contour, Green: EMD final contour). (b) Color distribution in *Lab* space. (c) Distribution inside (red) and outside (blue) the initial contour. Intermediate colors indicate partial pertenence. (d) Distribution inside/outside Bhattacharyya final contour. (e) Distribution inside/outside EMD final contour. (f) Evolution of Bhattacharyya Distance $B = -\log \tilde{B}$ as initial contour evolves under both schemes. (g) Evolution of EMD as initial contour evolves under both schemes.

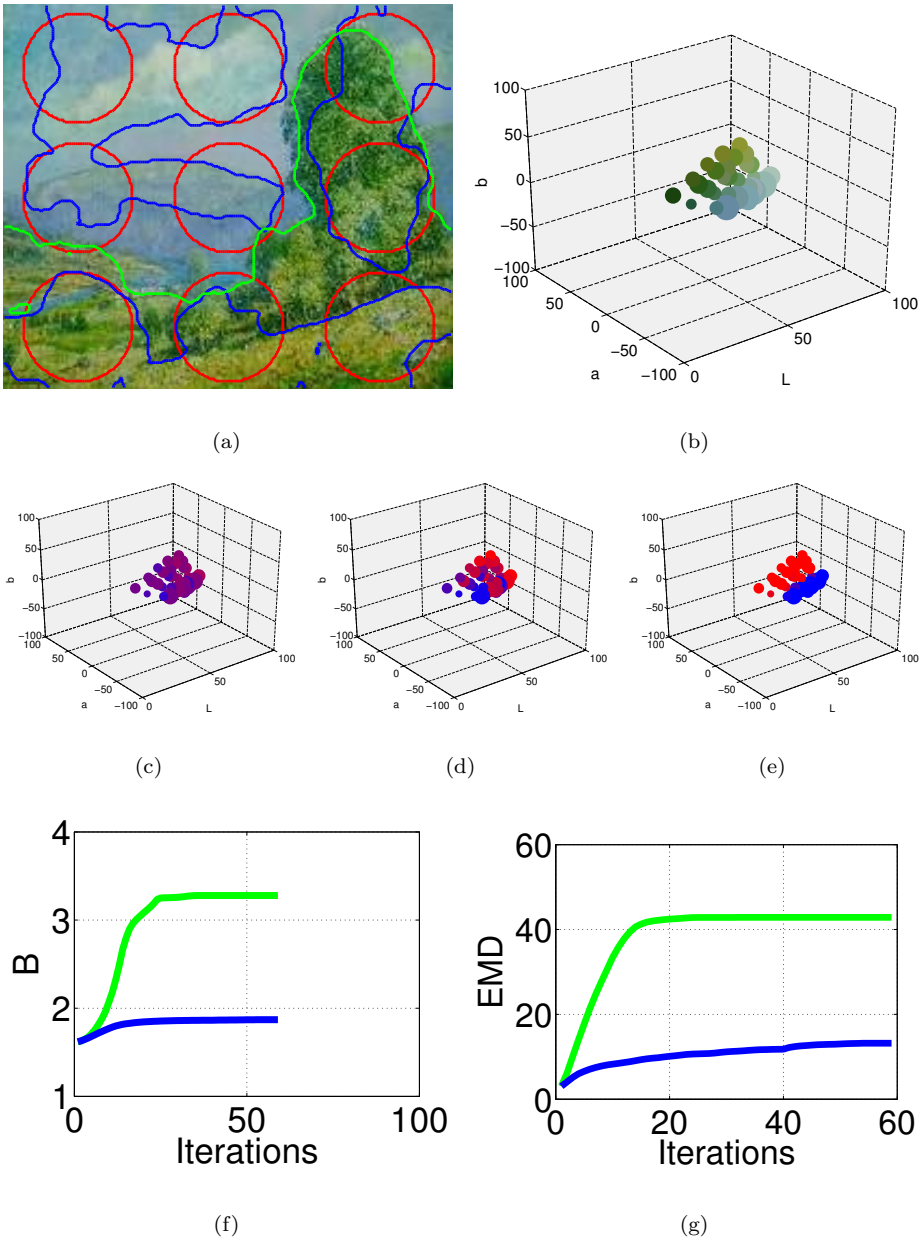

Figure 4.9: Segmentation for 'Landscape' Image. (a) Original image with contours overimposed (Red: Initialization, Blue: Bhattacharrya final contour, Green: EMD final contour). (b) Color distribution in *Lab* space. (c) Distribution inside (red) and outside (blue) the initial contour. Intermediate colors indicate partial pertenence. (d) Distribution inside/outside Bhattacharyya final contour. (e) Distribution inside/outside EMD final contour. (f) Evolution of Bhattacharyya Distance $B = -\log \tilde{B}$ as initial contour evolves under both schemes. (g) Evolution of EMD as initial contour evolves under both schemes.

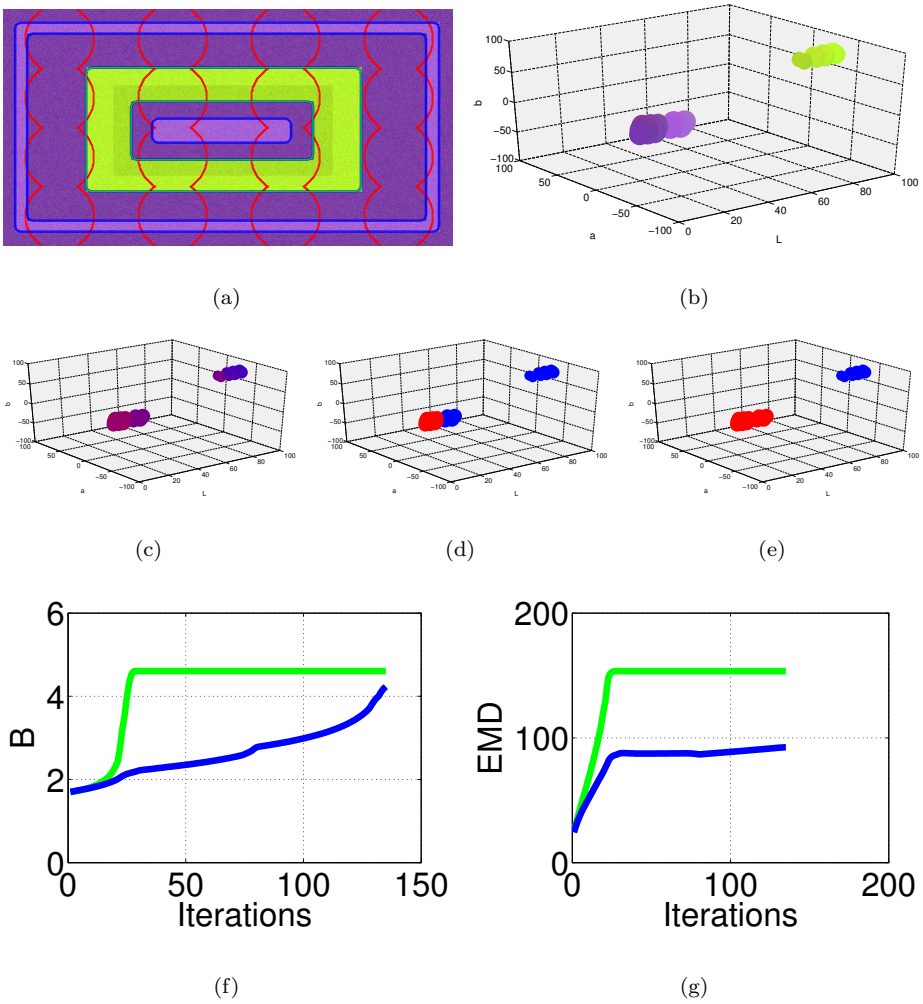

Figure 4.10: Segmentation for 'Rectangles' Image. (a) Original image with contours overimposed (Red: Initialization, Blue: Bhattacharrya final contour, Green: EMD final contour). (b) Color distribution in *Lab* space. (c) Distribution inside (red) and outside (blue) the initial contour. Intermediate colors indicate partial pertenence. (d) Distribution inside/outside Bhattacharyya final contour. (e) Distribution inside/outside EMD final contour. (f) Evolution of Bhattacharyya Distance $B = -\log \tilde{B}$ as initial contour evolves under both schemes. (g) Evolution of EMD as initial contour evolves under both schemes.

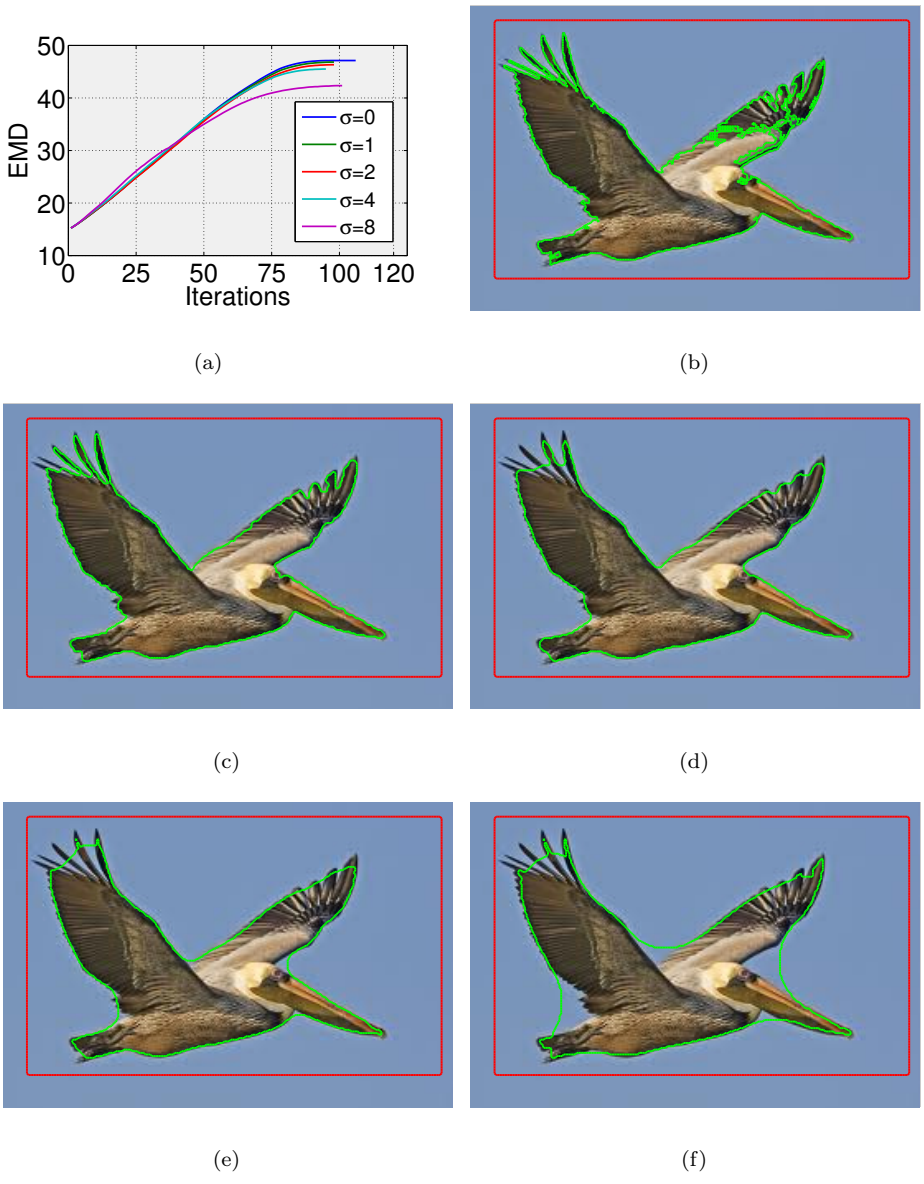

Figure 4.11: Influence of the Regularizer on 'Pelican' Image Segmentation. (a) EMD evolution for all regularization levels. (b) No regularizer. (c) $\sigma = 1$. (d) $\sigma = 2$. (e) $\sigma = 4$. (f) $\sigma = 8$.

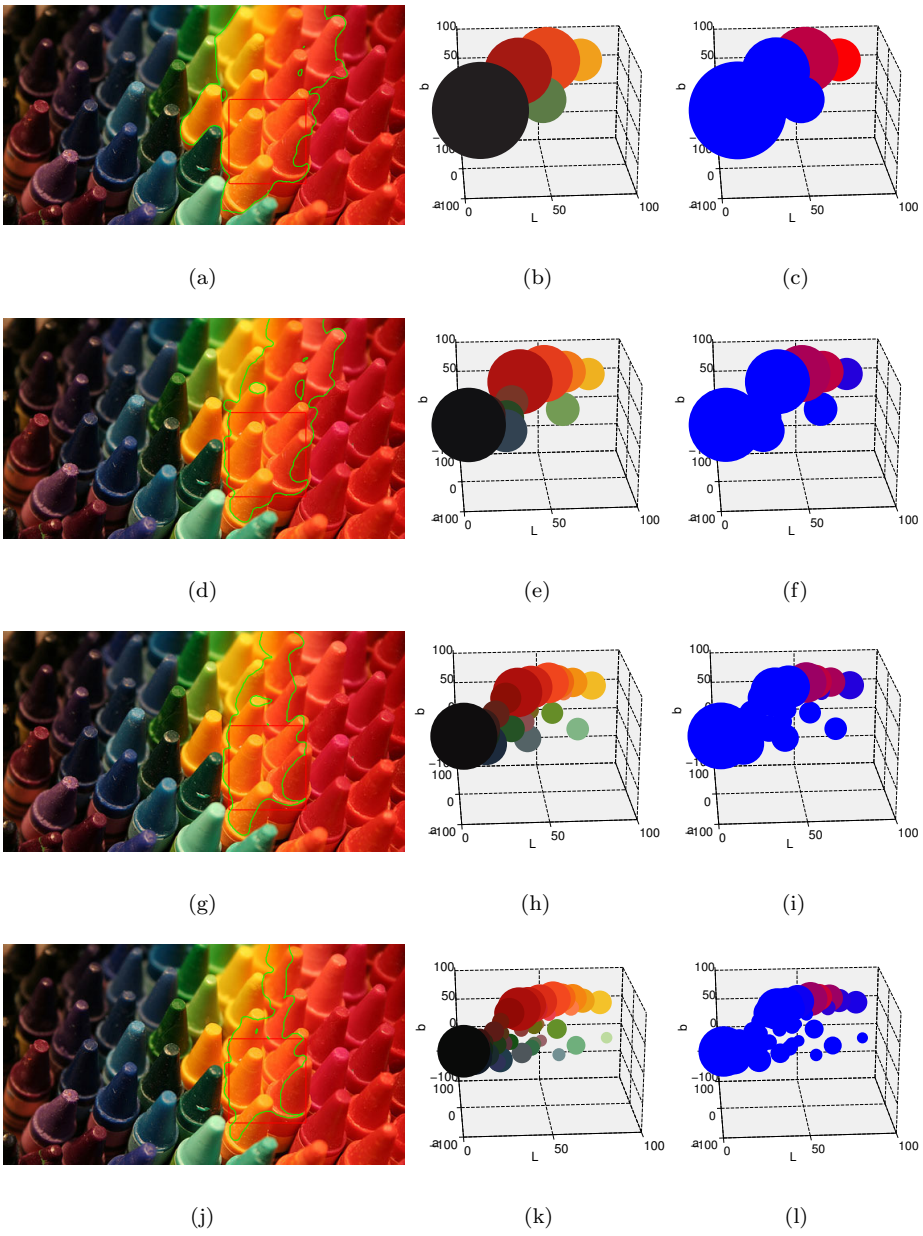

Figure 4.12: Influence of N on 'Crayons' Image Segmentation. (First colmun) Images showing initialization and final EMD contour. (Second column) Color distribution in *Lab*. (Third column) Distribution inside (red) and outside (blue) EMD final contour. Intermediate colors indicate partial pertenence. (First row) $N = 5$. (Second row) $N = 10$. (Third row) $N = 20$. (Forth row) $N = 40$.

4.4 Conclusion

We propose in this work all the necessary steps in order to perform multi-dimensional (or one-dimensional non-arbitrary ground-distance based) EMD-maximizing active contours. The unavailability of closed analytical expressions for derivatives of these types of EMD computations is circumvented using sensitivity analysis. Then active contour equations based on such analysis are derived comprehensively and tested thanks to a fast approximate implementation.

To illustrate the properties of our novel gradient flows, we have proposed a color segmentation scenario previously untreatable with EMD (one-dimensional) gradient flows. We make use of a signature representation in three-dimensional $L^*a^*b^*$ color space. Test images are represented as a set of clusters in this space using the k-means algorithm. Then the ground distances between cluster centroids - i.e. the work needed to transfer one unit of mass from one cluster to another - are made equal to their Euclidean distance in the aforementioned perceptually uniform color space.

Previous one-dimensional EMD gradient flows [134] have been compared with Bhattacharyya flows like Michailovich et. al. [132]. As done in [134] for the one-dimensional case, we compare our color EMD gradient flow with the equivalent Bhattacharyya flow. For every experiment we use the same cluster configuration and run both gradient flows using the same approximate level-set evolution framework.

Then we study the influence of the regularizer and the number of clusters in the signature on some exemplary test images.

Finally we provide segmentation results using images of skin lesions, obtained from MDC and H-MDC schemes.

As can be seen from results, EMD active contours are better correlated with color perception, are less sensitive to initialization thanks to fewer local extrema, and ultimately produce more meaningful segmentations when it makes sense to apply the maximal discrepancy criterion.

This descriptive richness can also benefit active contour segmentation for other sets of features, like those derived from texture descriptors, that were not suitable for one-dimensional, Euclidean ground distance EMD active contours.

Two main limitations of our approach can be outlined. First, the inside/outside regions only change at their interfaces due to the approximate implementations. This can be solved by using a standard partial differential equation (PDE) implementation with a regularized Dirac delta function that would extend the evolving contour to an evolving band, as proposed in [125]. Of course this will affect performance. Second, the maximal discrepancy criterion is not always suitable for object segmentation, since it is not always the case that the object maximally differs from the background. There might be several discrepant regions, as in 4.7. For such cases it becomes necessary to provide a multi-region level-set extension for our algorithm.

Furthermore, other energetic criteria could be brought into the multi-dimensional EMD framework, like the Match-to-Template criterion proposed in [134].

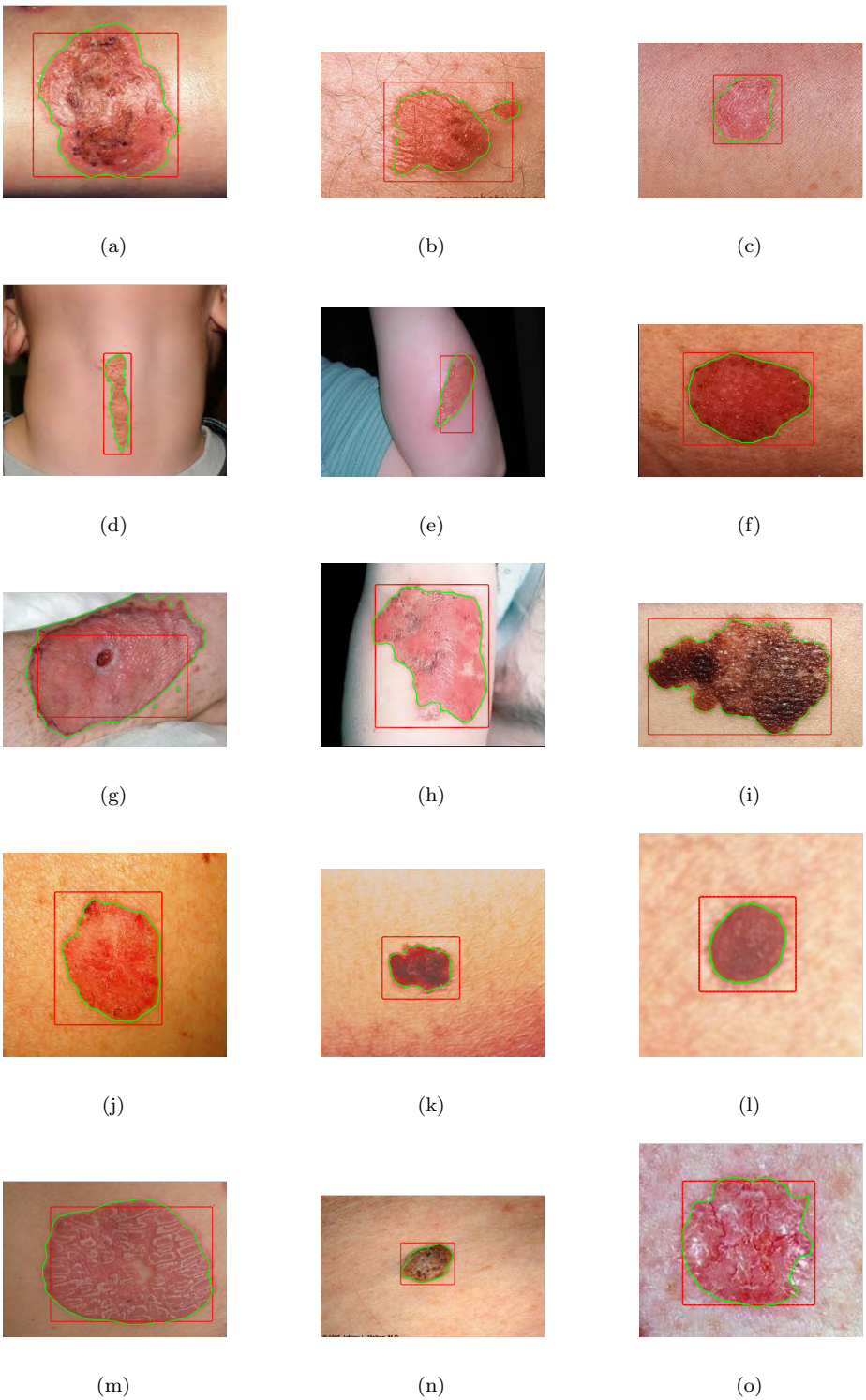

(a) (b) (c)

(d) (e) (f)

(g) (h) (i)

(j) (k) (l)

(m) (n) (o)

Figure 4.13: Examples of skin lesion segmentation using MDC

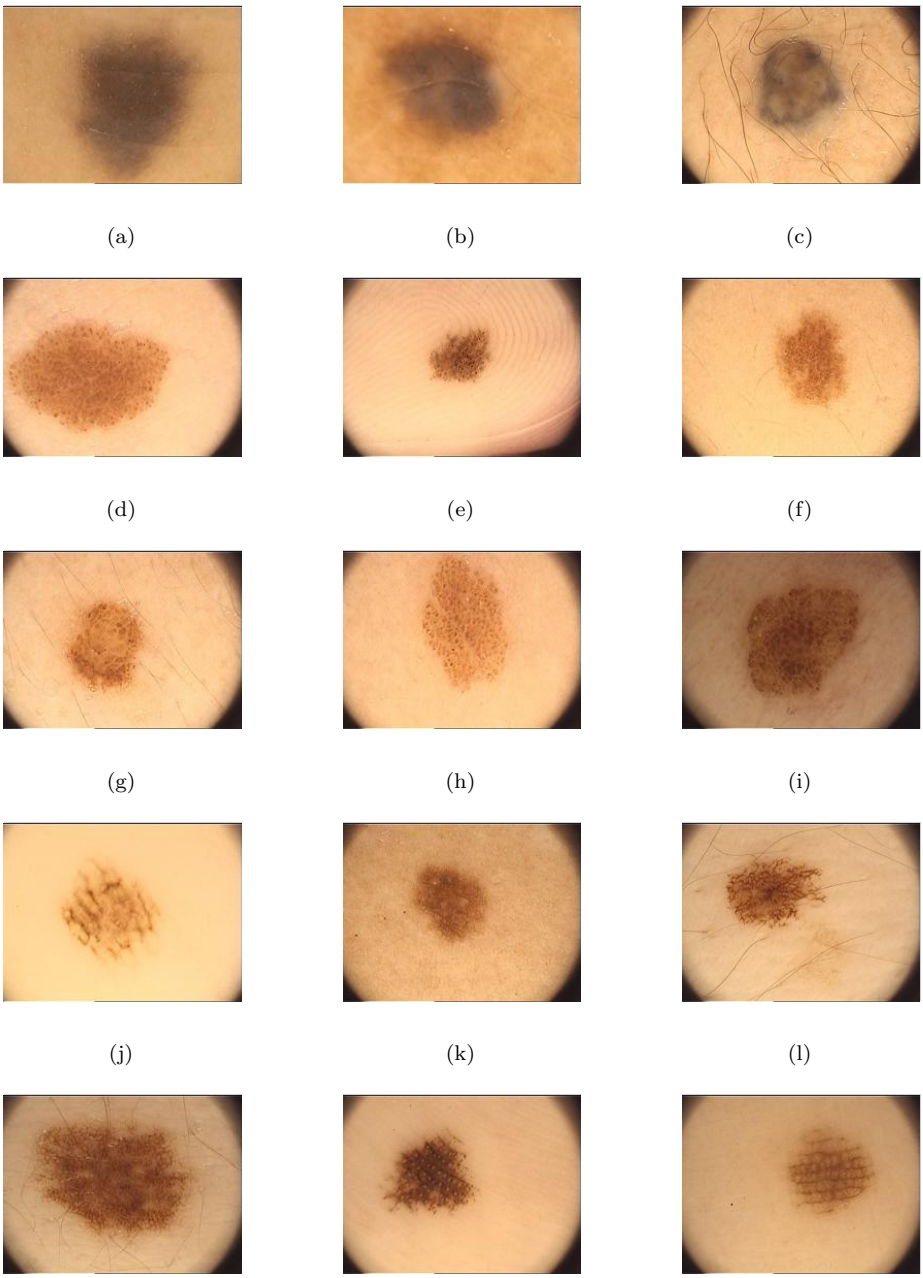

(a) (b) (c)

(d) (e) (f)

(g) (h) (i)

(j) (k) (l)

(m) (n) (o)

Figure 4.14: Examples of melanocytic lesions

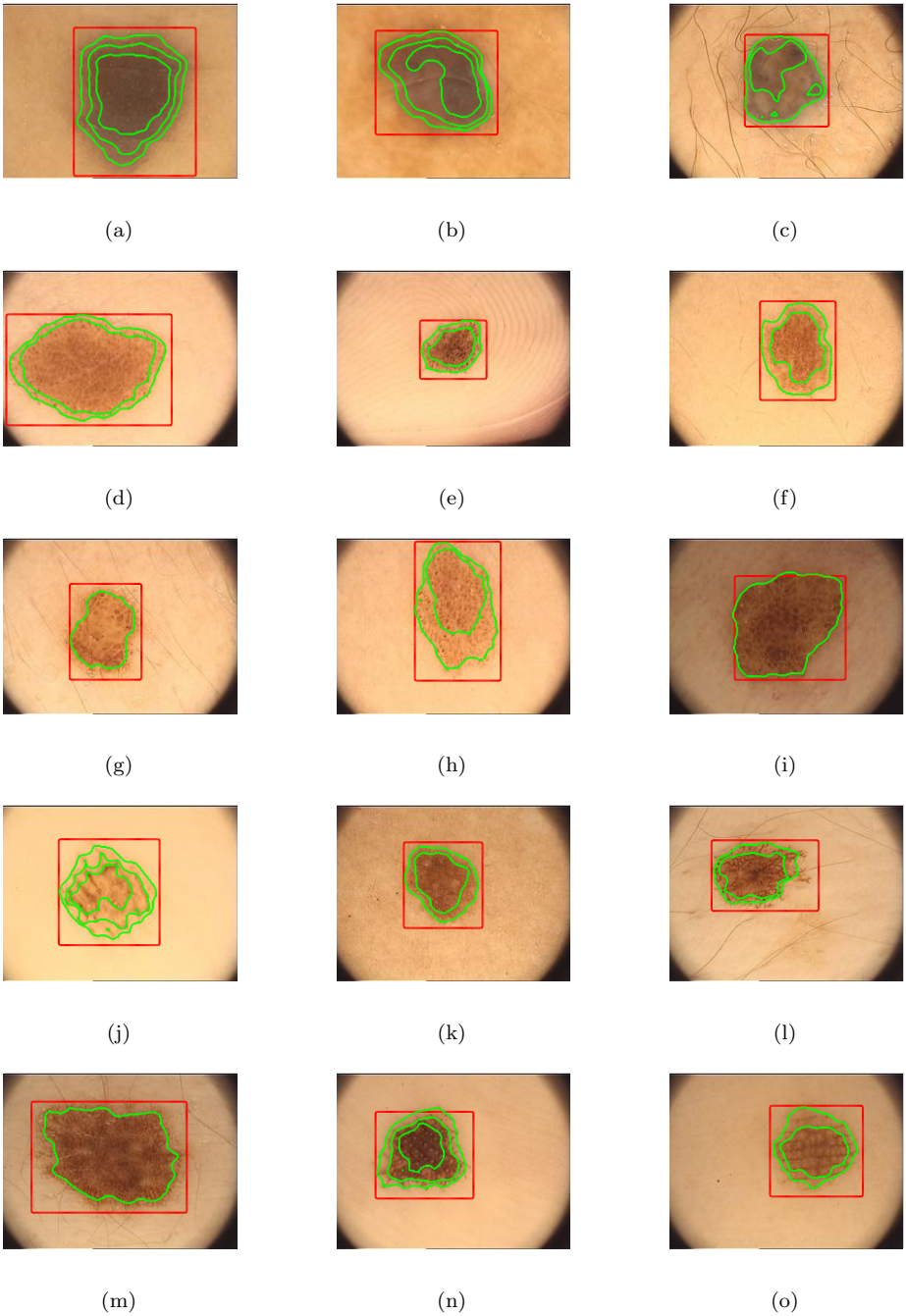

(a) (b) (c)

(d) (e) (f)

(g) (h) (i)

(j) (k) (l)

(m) (n) (o)

Figure 4.15: Segmentation of lesions in Fig. 4.14 using H-MDC. The number of displayed contours indicate the number of hierarchical iterations applied.

Chapter 5

Advances for CAD: Quantification of Pigmented Lesions

Pattern Analysis of Dermoscopic Images Based on Finnite-Symmetric Conditional Model Color Markov Random Fields

---

5.1 Introduction

In the last two decades a rising incidence of malignant melanoma has been observed. Because of a lack of adequate therapies for metastatic melanoma, the best treatment is still early diagnosis and prompt surgical excision of the primary cancer. Dermoscopy (also known as epiluminescence microscopy) is an in vivo method that has been reported to be a useful tool for the early recognition of malignant melanoma [150]. Its use increases diagnostic accuracy between 5 and 30% in clinical visual inspection [151].

Currently available digital dermoscopic systems offer the possibility of computer storage and retrieval of dermoscopic images. Some systems even display the potential for Computer Assisted Diagnosis [152, 153]. As diagnostic accuracy with dermoscopy has been shown to depend on the dermatologist's experience, CAD systems will help less-experienced specialists and decrease the impact of inter-subject variability.

Most technical papers developing methods to automatically classify dermatological images are based on the ABCD rule (Asymmetry, Border irregularity, Color variation, Diameter greater than 6 mm or growing). Frequently, such papers present an approach to cover one or several "letters" of the rule, that is, some are based on detecting asymmetry [154, 155], borders [156–159], color [160, 161] or diameter [161].

One of the key ideas of our work is that it is not focused on detecting specific features in the images to cover the four letters of the ABCD rule, but instead

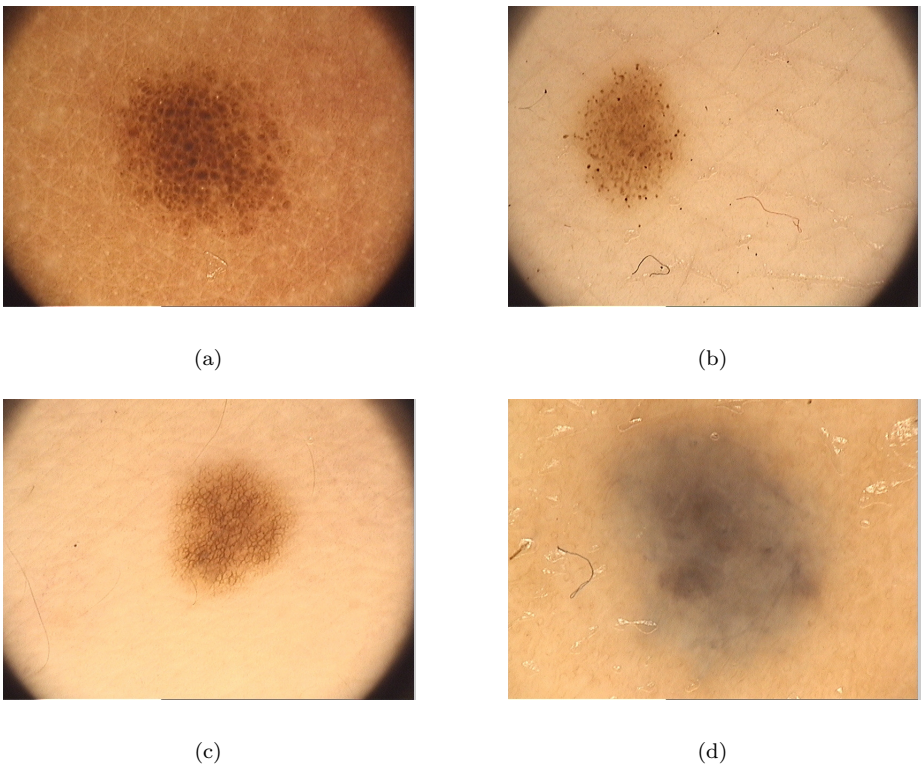

(a) (b)

(c) (d)

Figure 5.1: Examples of the patterns under study. (a) Cobblestone. (b) Globular. (c) Reticular. (d) Homogeneous

follows the new tendency in dermatology: to look for specific patterns in the lesions which can lead physicians to an assessment, by means of the so-called pattern *turbulence* analysis [162].

According to [163], in dermoscopic observation, global patterns are the first features of recognition and are subdivided into representative classes. Basic global features include reticular, globular, cobblestone, homogeneous, starburst and parallel patterns [163, 164]. Multicomponent pattern is a combination of three or more patterns, meaning that there is a high possibility of malignant melanoma. Interestingly, it has been claimed that benign lesions show symmetrical dermoscopic distributions of patterns and malignant ones depict asymmetrical distributions of patterns [163, 164].

It would be desirable to incorporate this new dermoscopy pattern analysis trend in a computer-assisted detection (CADe) system. Pattern irregularity, sometimes referred as *turbulence*, can be evaluated by the specialist as long as we can devise techniques for texture characterization inside the area of the lesion.

In their article, Tanaka et al. [162] extracted different features for texture description of abnormal skin pigmentation samples. Unfortunately their study does not provide a list of principal features, preventing from further extensions towards a pattern turbulence quantification method. Our contribution consists

in a thorough description of a particular modelization [165] which, relying on a great classification success rate for as many as four of the existing melanocytic patterns, ultimately provides a framework for pattern chart creation.

In this work we take Serrano et al. [165] a couple steps forward. We segment the lesion from healthy skin, which was done manually in their work. But our main contribution is providing an asessment of lesion pattern irregularity from classifying a grid of overlapping ROIs inside the lesion, which allows for assessing global irregularity approximately without the need for texture segmentation. Then, further developments on recognition techniques for interpreting the obtained chart might be exploitable for malignancy assessment toward a computer-assisted diagnosis (CADx) system.

In order to perform the pattern analysis to classify the dermoscopic image samples, we follow a model-based technique. In such methods, image classification is treated as an incomplete data problem, where the value of each pixel is known, and the label which identifies the underlying texture is unknown. Additionally, textures are modeled as Markov random field (MRF) realizations and their characterization is posed as a parameter estimation problem. Once the parameters have been estimated, we propose a Gaussian model for the extracted parameters to be treated as features in our classification problem. We proceed then to classification by solving an energy optimization problem in a Bayesian framework. In this study we will deal only with globular, reticular, homogeneous and cobblestone patterns, as can be seen in Fig. 5.1.

One important characteristic of melanocytic patterns is color. Panjwani et al. developed MRF models for unsupervised segmentation of textured color images considering inter-plane dependencies [166]. They work in the *RGB* color space, a perceptually non-uniform space. Kato et al. [167] use a combination of grey-level based texture features and color instead of direct modeling of color textures. The color features are calculated in the $L^*u^*v^*$ color space. Tab et al. present a multi-resolution color image segmentation algorithm [168]. Regarding the MRF model for colored textures, they assume channel conditional independence and they use the *YUV* color space. In this work we describe a MRF model-based classification framework, performed in the $L^*a^*b^*$ color space. We consider inter-channel dependencies explicitly in our approach.

In what concerns the use of MRF in segmentation/classification of dermoscopic images the literature is scarce. To the best of our knowledge, only Gao et al. [169] present a related approach. The MRF technique is poorly explained, and they use the first plane of the PCT (Principal Component Transform) of the dermoscopic images, i.e. is a grey-level version of MRF modeling. But, in any case, their ultimate goal is to segment the lesion, which for us is just a preprocessing step.

5.2 Model-based Classification Algorithm

For textured images, the theory based on Markov Random Fields (MRF) is an important field, which has been developed extensively in the last decades. MRF theory provides a convenient and consistent way for modeling context-dependent

entities such as image intensities/color and spatially correlated features [170].

According to the theory of MRF, the field is uniquely described by its Gibbs clique potential parameters, and feature extraction is equivalent to parameter estimation [170]. We will model each one of the classes under study as a different MRF. We will then estimate the parameters for every class model, and use them to create a feature space for the classifier to operate upon.

In this work we present a trained classification scheme. A training set with images individually representing each pattern is available. The training set is formed by 50×50 patches extracted from single-pattern dermoscopy images of melanocytic lesions, each one labeled by an experienced dermatologist as belonging to one of the four different patterns. The classifier, when facing a lesion with a specific pattern, must label it correctly.

We use the same images to build our test set. First, the lesion will be segmented from the background (normally pigmented skin) by applying the methodology explained in Chapter 4. Then, the segmented area will be analyzed by leave-one-lesion-out classification of overlapping neighborhoods of size 50×50. Finally a pattern chart is obtained, capable of approximating the spatial extent of the different patterns inside the lesion.

5.2.1 Texture Model

As suggested in Xia et al. [171], each textured color plane is considered as a random field G, defined on a $W \times H$ rectangular lattice, where W and H represent the patch size (in our case $W = H = 50$). The lattice is denoted by $S = \{(i,j) : 1 \leq i \leq W, 1 \leq j \leq H\}$, which is indexed by the coordinate (i,j). Each of the color planes are represented by $G = \{G_s = g_s : s \in S\}$, where $s = (i,j)$ denotes a specific *site* and the random variable G_s represents a value of the pixel at s in one of the planes of the $L^*a^*b^*$ color space. An observed patch color plane $g = \{g_s : s \in S\}$ is an instance of G. It can be described by a finite symmetric conditional model (FSCM) [172] as follows

$$g_s = \mu_s + \sum_{t \in \eta_g} \beta_{s,t}[(g_{s+t} - \mu_{s+t}) + (g_{s-t} - \mu_{s-t})] + e_s \ , \tag{5.1}$$

where $\eta_g = \{(0,1),(1,0),(1,1),(-1,1)\}$ is the set of shift vectors corresponding to the second order neighborhood system, μ_s is the mean of the pixels in the sample, $\{\beta_{s,t} : t \in \eta_g\}$ is the set of correlation coefficients associated with the set of translations from every site s, and $\{e_s\}$ is a stationary Gaussian noise sequence with variance σ_s^2.

The scope of our work presented herein, is to classify 50×50 pixel images into 4 possible patterns. Each patch will be characterized by a unique parameter vector $\vec{f}$, calculated for the whole extent of the patch. Pixels take value in a 3D (three-dimensional) space ($L^*a^*b^*$). Each one of the planes contributes six parameters. Therefore, the parameter vector $\vec{f}$ is formed by 18 components:

$$\vec{f} = (\mu_L, \sigma_L^2, \beta_{L,t}, \mu_a, \sigma_a^2, \beta_{a,t}, \mu_b, \sigma_b^2, \beta_{b,t} : t \in \eta_g) \ . \tag{5.2}$$

5.2.2 Parameter Estimation

In order to estimate the parameters, we follow the least-squares estimation method [173, 174]. For each color plane we get the following parameter estimators

$$\hat{\beta} = \left[\sum_{s\in N^I} Q_s Q_s^T\right]^{-1} \left[\sum_{s\in N^I} Q_s g_s\right] \ , \tag{5.3}$$

$$\sigma^2 = \frac{1}{|N^I|}\sum_{s\in N^I}\left[g_s - \hat{\beta}^T Q_s\right]^2 \ , \tag{5.4}$$

$$\mu = \frac{1}{|N|}\sum_{s\in N} g_s \ . \tag{5.5}$$

where Q_s is a column vector defined by $Q_s = [g_{s+t} + g_{s-t} : t \in \eta_g]$ with dimensions (4×1×3) because g_s is a 3D color pixel, N is the set of all the sites belonging to the patch of interest and N^I is the interior subset of N. Because we are processing color images, the dimensions of the parameters are (4×1×3) for $\hat{\beta}$, (1×3) for σ^2 and (1×3) for μ. In summary, the parameter vector has 18 components as it has been described in Sect. 5.2.1.

5.2.3 Feature Model

The Gausian mixture is typically an appropriate model for the components of the feature vector in most classification problems, where those components are continuous valued.

The $L^*a^*b^*$ color space is considered as a perceptually uniform color space, i.e. distances calculated in this space approximately match perceptual color differences as perceived by the human visual system.

Chen et. al. [175] showed that applying the K-L (Karhunen-Loève) transform to one hundred test images in $L^*a^*b^*$ coordinates, the principal eigenvector in $L^*a^*b^*$ coordinates is very close to the vector $(1,0,0)^T$, and the other two eigenvector are primarily in the a^*b^* plane of the $L^*a^*b^*$ color system. We postulate this as a justification for considering statistical independence between the L^* component and the a^*b^* components.

We assume that the six parameters obtained from L^* component are independent from the twelve parameters calculated from the a^* and b^* components. Therefore, $\vec{f}$ is decomposed into two parameter vectors:

$$\vec{f_L} = (\mu_L, \sigma_L^2, \beta_{L,t} : t \in \eta_g) \ , \tag{5.6}$$

$$\vec{f_{ab}} = (\mu_a, \mu_b, \sigma_a^2, \sigma_b^2, \beta_{a,t}, \beta_{b,t} : t \in \eta_g) \ , \tag{5.7}$$

each one following a Normal mixture distribution $N(\vec{M}_{i,\lambda}, \Sigma_{i,\lambda})$ with ML-estimated mean $\vec{M}_{i,\lambda}$ and ML-estimated covariance matrix $\Sigma_{i,\lambda}$ for $i \in \{L, ab\}$. The variable λ represents the pattern class, $\lambda \in \Lambda = \{1,2,3,4\}$.

$$N(\vec{M}_{i,\lambda}, \Sigma_{i,\lambda}) = \frac{\exp\left(-\frac{1}{2}(\vec{f_i} - \vec{M}_{i,\lambda})\Sigma_{i,\lambda}^{-1}(\vec{f_i} - \vec{M}_{i,\lambda})^T\right)}{\sqrt{(2\pi)^n |\Sigma_{i,\lambda}|}}, \tag{5.8}$$

where n is the dimension of the parameter vector ($n = 6$ for $\vec{f}_L$ and $n = 12$ for $\vec{f}_{ab}$).

5.2.4 Optimization

As our images consist of overlapping patches containing patterns out of four different classes (reticular, cobblestone, homogeneous and globular), each patch will be assigned to a unique label λ, taking values from a finite set $\Lambda = \{1,2,3,4\}$. We assume that each texture pattern occurs with the same probability in any pigmented lesion of our dataset. Therefore the Λ variable is uniformly distributed. In order to find the optimum label for the patch under study, we apply the maximum likelihood (ML) criterion instead of the maximum a posteriori probability (MAP) criterion, as we assume that the prior information of the label follows a uniform probability mass function:

$$\hat{\lambda} = \underset{\lambda \in \Lambda}{\operatorname{argmax}}\, P(\vec{F}_L = \vec{f}_L, \vec{F}_{ab} = \vec{f}_{ab} | \lambda) \ . \tag{5.9}$$

Assuming independence between $\vec{f}_L$ and $\vec{f}_{ab}$ (according to Sect. 5.2.1):

$$P(\vec{F}_L = \vec{f}_L, \vec{F}_{ab} = \vec{f}_{ab} | \lambda) = P(\vec{F}_L = \vec{f}_L | \lambda) P(\vec{F}_{ab} = \vec{f}_{ab} | \lambda) \ . \tag{5.10}$$

The ML problem given by (5.9) can then be solved by minimizing the following energy, deriving from the exponent of the Gaussian multivariate:

$$\begin{aligned} \hat{\lambda} &= \underset{\lambda \in \Lambda}{\operatorname{argmin}} \left\{ E_G(\vec{f}_L, \lambda) + E_G(\vec{f}_{ab}, \lambda) \right\} \\ &= \underset{\lambda \in \Lambda}{\operatorname{argmin}} \left\{ \left[\left(\vec{f}_L - \vec{M}_{L,\lambda} \right)^T \Sigma_{L,\lambda}^{-1} \left(\vec{f}_L - \vec{M}_{L,\lambda} \right) + \ln \left((2\pi)^6 \left| \Sigma_{L,\lambda} \right| \right) \right] \right. \\ &\left. + \left[\left(\vec{f}_{ab} - \vec{M}_{ab,\lambda} \right)^T \Sigma_{ab,\lambda}^{-1} \left(\vec{f}_{ab} - \vec{M}_{ab,\lambda} \right) + \ln \left((2\pi)^6 \left| \Sigma_{ab,\lambda} \right| \right) \right] \right\} \ , \end{aligned} \tag{5.11}$$

that takes into account the Gaussian multivariate parameters ML-estimated from the training samples and compares them with the parameter vectors obtained for the patch under study.

5.3 Experimental Results

The proposed algorithm has been tested on a database containing 9 images corresponding to every different kind of pattern, adding up to a total of 36 images. All the images were acquired with the same, calibrated dermoscope Fotofinder Schuco International London Limited. The images are of size 767×576 and have been classified by a physician as globally belonging to one of the four patterns in our training set. Since the available lesions contain only samples of one single class, the overall quality of the classification will be measured using the percentage of lesions assigned to the right global pattern available in each lesion. As

Table 5.1: Classification Results

Pattern	Success rate	Robustness
Reticular	1.00	0.65
Cobblestone	1.00	0.84
Homogeneous	0.89	0.82
Globular	0.56	0.80
Average	0.86	0.78

training, we have employed 50 50×50 different patches for each of the 4 possible textures. Considering the small size of the available database, 5 patches were extracted from every lesions. For the classification of the patches inside a lesion, only patches from the other lesions were used for training.

The segmented area was analyzed in 50×50 overlapping neighborhoods according to the method described above. The resulting labels were polled to throw a global majority label. Then the whole lesions gets assigned to that class. The average success rate is summarized in Table 5.1. Notice the good results for the first three pattern classes. Mediocre results for globular pattern are probably due to varying degree of globule scale in the available database. We hope this figure to rise as soon as we can have a greater database with representative cases for all patterns and we are able to study our system's behavior against texture scale variations.

The robustness measure in Table 5.1 takes into account the percentage of properly classified patches inside the globally successfully classified lesion. The lower value for reticular lesions indicate that the classifier labeled many non-reticular patches inside the reticular lesions. After carefully observing our reticular lesions, we conclude that in fact globally reticular lesions tend to contain fuzzy areas that are not strictly reticular.

Figure 5.2 shows an example of a pattern chart. The chart, when compared with the lesion, illustrates the fact that subtle irregularities in the apparently single-textured lesion, provide alternative pattern labelings, thus revealing the potential of our charting strategy for helping the specialist in malignancy assessment.

5.4 Conclusion

We have presented a novel pattern description technique based on MRF modeling. The main singularity of our work is the methodology followed to analyze the dermoscopic images. To the best of our knowledge, except for [162,165], the references in the literature mostly apply the ABCD rule in order to classify the lesion. In this work, we introduce a new methodology to assist the specialist in analyzing pattern distribution in melanocytic lesions. We segment the lesion from healthy skin. Also we perform classification on overlapping patches, which

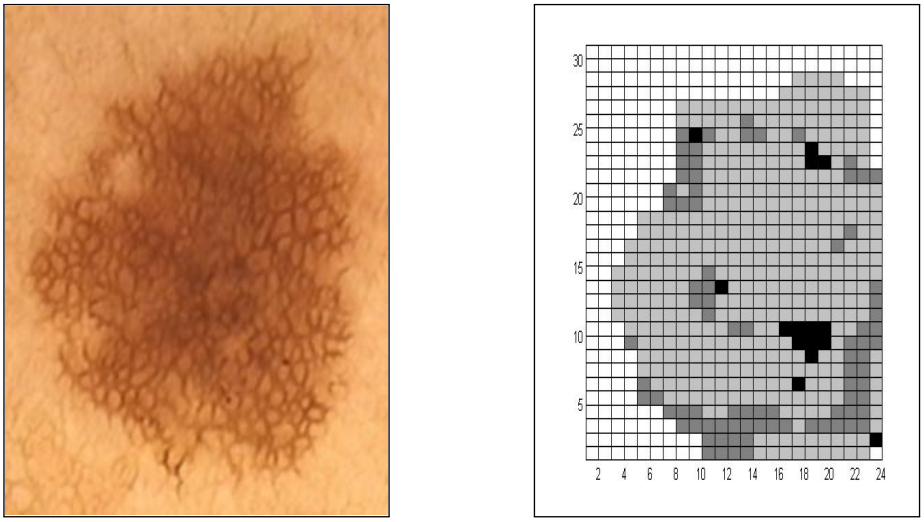

Figure 5.2: Quantification example for a reticular lesion. The grid on the right represents the labeling of the patches in the lesion on the left. Gray levels evolve from white to black according to the following order: Healthy skin, Reticular, Cobblestone, Homogeneous(absent in this example) and Globular. Notice how subtle irregularities are detected in the chart creation

spares the need for texture segmentation schemes. Finally, we provide a charting method which facilitates the specialists' turbulence analysis and malignancy assessment.

For analysing the color textured pattern, we model the image as a FSCM model, and calculate a feature vector with the estimated parameters of the model. To classify, we apply the ML criterion to maximize the conditional probability assuming a Gaussian distribution of the feature vectors. We make use of the $L^*a^*b^*$ color space and suppose independence between the parameters extracted from the L^* channel and the ones calculated from the a^* and b^* channels.

The starbust pattern was not analyzed because its description requires segmentation, as its main discriminative characteristic from the rest of patterns is located in the border of the starbust lesion, and not in a particular pattern inside the lesion [163]. Regarding parallel pattern, we are currently working on rotation-invariant descriptors that can possibly respond in the same manner to parallel pattern with different orientations.

Our contribution establishes a line of work towards malignancy assessment by characterization of the textures present in the lesion, eliminating the need for texture segmentation.

Chapter 6

Advances for Surgical Planning: Segmentation of CT Scans

Fast Parameter-Free Region-Growing Segmentation for Virtual-Reality Planning in Plastic Surgery

---

6.1 Introduction

One of the most promising applications of medical image computerized visualization is virtual reality surgical planning. Traditional surgical planning uses volumetric information stored in a stack of intensity-based images, usually from computerized tomography (CT) scanners. Based on a number of these image slices, surgeons build their own mental 3D model of the relevant tissues. This task is difficult even for experienced surgeons. As a consequence, they can miss important information or draw incorrect conclusions due to anatomical variability, either of which can lead to suboptimal treatment strategy decisions [176]. Using volumetric renderings of anatomical structures, and the appropriate virtual tools for basic surgical operations, the complexity of many plastic surgery interventions can be addressed ahead of the actual physical procedure.

A main bottleneck for these computer environments is the delineation of the tissues involved, to such an extent that automated approaches become mandatory. If we can provide a technique that is able to automatically detect the tissues of surgical interest (fat, bone, muscle), then these tissues can be rendered, excisioned directly in 3D, and manipulated or repositioned using the virtual reality platform.

Automatic segmentation is a problem exhaustively addressed in the literature. Any inaccuracies in the process can distort the simulated measures and surgical operations. In this work we propose a novel segmentation strategy in the context of the development of a virtual surgical planning environment.

The environment under study was conceived for the simulation of different kinds of reconstructive surgery, providing virtual tools for tissue excision and repositioning, tissue quantification and stereo-lithographic prototyping. In such a framework the need for proper delineation of tissues like fat, muscle and bone becomes crucial. In the initial version of the platform, a simple voxel classification scheme was proposed [177]. Beyond classical segmentation methods like thresholding and simple region growing [178–180], which rely on a number of tuning parameters, developments in automatic parameter-free segmentation approaches become necessary.

In order to pay back the cost and burden of this virtual surgical planning platform development, a wide range of situations were to be covered with the proposed technique. Most available resources, i.e. imaging devices, must be compatible with the method, even ensuring backwards compatibility (for images acquired in the past). As a consequence neither resolution, contrast nor signal-to-noise rate (SNR) specific standards can be expected. Further, no imaging protocol can be presumed, as regarding reconstruction algorithm, patient positioning in the scanner, presence of radioactive contrast, body segment of the patient to be imaged and so on.

A few authors have referred to the issue of classifying this concrete set of tissue types using a common method. In their work, Zhou et al. [181] developed a technique for skin, fat, muscle, organs and bone segmentation. Their approach was mainly articulated by threshold automatic selection, except for bony tissue, for which the authors made use of a self-assessed adaptive region growing algorithm. Their threshold selection method, based on hierarchical discriminant analysis made assumptions on the histogram that turned out to be unaffordable in our less predictable context. Their strategy for bony tissue, that had been earlier proposed for bronchus segmentation by Law and Heng [182], computed the optimal adaptive threshold by detecting sudden increases in the segmented volume. Its main weakness is the need for an empirical range in this increase, in order to distinguish routinary growth from undesired explosion. This range can hardly be established in our more general problem, since we are faced with varying noise levels, which makes it hard to generalize how much growth must be considered explosion.

Apart from manual trial-and-error adaptive threshold selection [183], some self-assessed region growing strategies, outside our context of application, have been proposed in the past. Some general requirements are expected from any region growing algorithm for clinical use. Such methods must operate in a parameter-free manner, the degree of interaction should be minimal, the output must be provided in reasonable time ranges, and also similar results should be produced for alternative seeding schemes in the region of interest [184].

In their work [185], Hojjatoleslami and Kittler proposed a 3D segmentation method based on finding the global maxima for two different contrast measures which they computed iteratively, as intensity-decreasing pixels were added to the segmented region. The success of the assessment was founded on the assumption that maximal contrast occurred on region boundaries, which is a reformulation of approaches assuming that the variation of the gray values within regions is smaller than across regions, an inherent assumption in all region growing techniques [186]. Unfortunately, the exhaustivity of their per-voxel approach

entailed very low computational efficiency, aggravated by their multiple complex peripheral measures. Moreover, the fact that they computed contrast for every voxel addition results in low robustness when facing increasing levels of noise. Revol-Muller et al. [187] used morphological measures to assess the multiplier of the adaptive range in 3D region growing. Instead of computing their assessment function for every pixel addition to the region, they sampled the function for an evenly-spaced set of values.

Another popular region growing technique was proposed by Udupa and Samarasekera [188], based on the fuzzy connectivity measure. This technique computes the path of strongest affinity between each point and the seed point. The fuzzy connectivity algorithm has been used in various medical applications [189–192]. All of these approaches exhibit the inconvenience of parameter-tuning stages prior to their execution, which prevents their use by untrained specialists. For the algorithm in [193], the fuzzy connectivity threshold value is not needed, but as a counter-effect the need for user interaction is considerably increased, and the required computational time rises to impractical values.

In our method we propose an assessment function based on a modified version of the evolving contrast for the region growing sequence. Our approach could be considered as an adaptive sampling strategy for the contrast measure, that is usually computed for every voxel addition to the growing region. This adaptive, regularly-spaced sampling can account for variations in the noise level as it can convey the proper low frequency trend of the evolving contrast, filtering off spurious variations. This results in increased stability and lower computational time, as fewer contrast values ought to be computed.

In Sect. 6.2 we will analyze the proposed technique, discussing the assumptions made on the intensity distribution of the tissues involved. We will describe the algorithm and the key aspects that constitute the novelty in our approach. In Sect. 6.3 we will present our validation experiments, and will objectively and subjectively analyze the accuracy, precision and efficiency of the algorithm according to trained expert assessments. The improvements obtained in virtual-reality surgical planning after integration of our technique will also be outlined. Finally, in Sect. 6.4 we will conclude with some remarks and future possibilities for our technique.

6.2 Method

6.2.1 Normalization and Denoising

From the nature of our regions of interest, we will consider tissue segments that exhibit an inherently constant density, and thus a similar requirement is expected from intensity in the image domain, except for the effects of acquisition noise. We intend to group together all voxels that belong to the same tissue class, and are connected to a provided set of seeds. We model then our object of interest as a connected region whose pixel intensities are sampled from a Gaussian distribution with unknown mean and standard deviation. We may presume that our tissues of interest are surrounded by other tissues derived

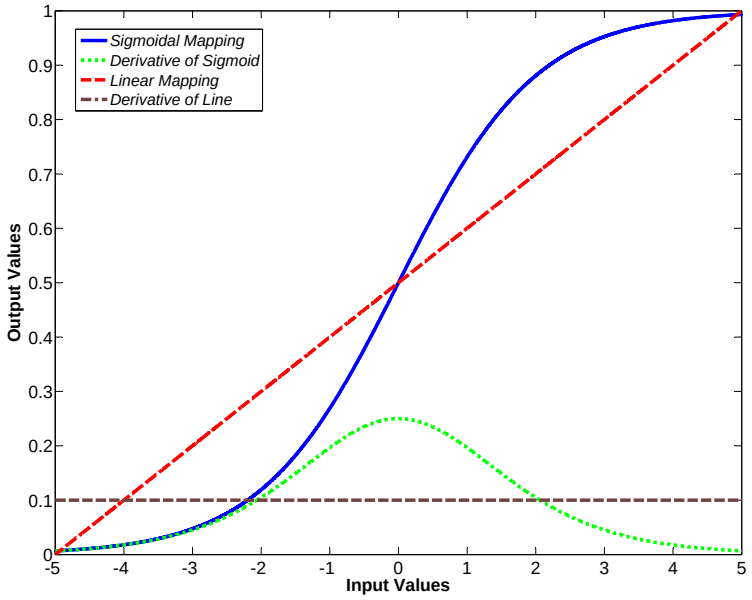

Figure 6.1: Comparison of dynamic range extension performed by sigmoidal and linear mappings. When the derivative of the sigmoid overpasses the constant derivative of the linear mapping for a given range of values, then the range gets expanded. The opposite indicates a range contraction.

from other, sometimes adjacent, intensity distributions, like other authors have proposed [194]. Due to the nature of our assessment function as described below, we need intensity values to be mapped in a range of positive values between zero and one. We make use of a sigmoidal mapping with varying slope depending on the statistics of the region surrounding the provided samples. This can amplify the significance of critical values of the assessment measure in comparison with those obtained with a simpler linear mapping. The reason is that sigmoidal mapping expands the range of values around its center and contracts those away from it. See Fig. 6.1 for a comparison of the derivatives of linear and sigmoidal functions. Aside from this, any mapping into positive ranges will do the job similarly as concluded from our tests.

If $\vec{x}$ is a voxel position, f is a function assigning intensity levels for every position in the image domain, as given by the dataset under study, and $|\cdot|$ denotes cardinality, we define the following operations on a set A of voxels:

$$\bar{f}_A = \frac{1}{|A|} \sum_{\vec{x} \in A} f(\vec{x}) \quad , \tag{6.1}$$

$$\sigma_{f_A} = \sqrt{\frac{1}{|A|} \sum_{\vec{x} \in A} \left(f(\vec{x}) - \bar{f}_A \right)^2} \quad . \tag{6.2}$$

These expressions are known as the sample mean and sample standard deviation

of the population obtained from the elements in A. If N_i is a cubic neighborhood of radius R around the i-th element of a set of M seeds, and $N = \bigcup_i^M N_i$, then $\bar{f}_N$ and σ_{f_N} are the Maximum Likelihood (ML) estimates of the mean and standard deviation of the underlying distribution from the provided population samples if:

$$\bar{f}_N = \frac{1}{M}\sum_{i=1}^{M} \bar{f}_{N_i} \quad , \tag{6.3}$$

$$\sigma_{f_N} = \frac{1}{\sqrt{M}}\sum_{i=1}^{M} \sigma_{f_{N_i}} \quad . \tag{6.4}$$

According to these estimates we proceed by application of a non-linear mapping consisting of a sigmoidal window centered at the mean, with width linearly dependent on the standard deviation:

$$f'(\vec{x}) = \left(1 + \exp\left(-\frac{f(\vec{x}) - \bar{f}_N}{\left(\frac{K\sigma_{f_N}}{3}\right)}\right)\right)^{-1} \quad . \tag{6.5}$$

The width of such a sigmoidal window is usually considered to extend $K\sigma$ around the center $\bar{f}_N$ of the mapping. For $K = 3$ the width of the window would be enough to map 99.7% of the samples hypothetically obtainable from a Gaussian distribution with similar mean and standard deviation. Greater values of K ensure sufficient mapping for the estimated distribution (that of the tissues of interest), avoiding saturation.

Finally, we perform non-linear denoising using an in-slice two-dimensional median filter with kernel radius Γ. Other denoising schemes have been tested without significant impact on the overall performance.

6.2.2 Self-Assessed Region Growing

Departing from a normalized and filtered version of the image under study, whose intensities lie in the range $[0,1]$, and a manually provided set of seeds, we apply our proposed self-assessed contrast-maximizing algorithm. Basically, the output of the region growing process depends on a confidence interval defined by coefficient k_i, that gets incremented from an initial value k_0 in equal steps of adapted size Δk. The set of operations for the i-th iteration is described in the following steps:

1. Compute i-th coefficient $k_i = k_0 + i\Delta k$
2. For $j = 0, 1, 2, ...L-1$, and $R_{i0} = N$:
   - Compute tolerance interval I_{ij} using 6.1, 6.2 and:

$$I_{ij} = I(R_{ij}) = \left[\bar{f'}_{R_{ij}} \pm k_i \sigma_{f'_{R_{ij}}}\right] \quad . \tag{6.6}$$

   - Compute $R_{i(j+1)}$ as the greatest 26-connected set of voxels inside the I_{ij} tolerance interval, that contains R_{ij} and is 26-connected to it.

3. Compute the assessment function $O_i\left(\bar{f}'_{R_{iL}}, \bar{f}'_{P_i}\right)$ according to the intensity average $\bar{f}'_{R_{iL}}$ in R_{iL} and the intensity average $\bar{f}'_{P_i}$ in the external perimeter P_i of R_{iL}:

$$P_i = (R_{iL} \oplus B) \cap R_{iL} \ , \tag{6.7}$$

where $\oplus$ denotes morphological dilation, and set B is some structuring element, using

$$O_i\left(\bar{f}'_{R_{iL}}, \bar{f}'_{P_i}\right) = \left| \frac{\bar{f}'_{P_i} - \bar{f}'_{R_{iL}}}{\bar{f}'_{P_i} + \bar{f}'_{R_{iL}}} \right| \ . \tag{6.8}$$

4. If O_{i-1} is a local maximum, when compared to O_{i-2} and O_i (only when $i \geq 2$), then the algorithm stops and the output is $R_{(i-1)L}$. Otherwise another iteration takes place

Of all aforementioned parameters only k_0 and Δk are critical for the performance of the algorithm. Lower values of k_0 affect computational efficiency requiring a greater number of iterations before a local maximum of $O\left(\bar{f}_{R_i}, \bar{f}_{P_i}\right)$ is actually found. Therefore, its fine tuning for a specific scanner, could save some computational time. From observation of the region growing sequence, we conclude that these first iterations are typically very fast, so the improvement is frequently negligible. With regard to Δk, the choice must guarantee that the assessment function is being sampled adequately in order to detect its local variations, but also coarsely enough so that contrast variations due to noise do not stop the algorithm on spurious maxima.

Fortunately, the fact that Δk affects the tolerance interval in each iteration through multiplication with the standard deviation, guarantees that the sampling of the assessment function adapts to the noise level in the dataset. As compared to the contrast evolution for regularly increasing intensity values, the resulting sampling will be spaced according to the standard deviation of the grown region (estimated with ever-increasing precision as the region grows). Assuming approximately constant regions of interest, this variance can be attributed mostly to noise. As a consequence, for a constant value of Δk, the sampling adapts to the roughness of the assessment function in such a way that the main trend of the evolution is captured, and higher frequency components are missed.

Beyond these considerations, we have determined the exact value of Δk empirically from the available datasets, and this value has proven to be rather general according to our experimental results.

To illustrate the pertinence of our assessment function, we provide in Fig. 6.2 an exhaustive analysis of the contrast evolution for our region growing sequence in three different segmentation scenarios. Using the same dataset, we have provided one single seed for bone, muscle and fat segmentations. Instead of stopping the algorithm at the first maximum, the region growing proceeds until the iteration right before full-image flooding. Contrast evolution curves where all maxima have been arrow-marked can be seen in Subfigs. 6.2(a)-(c). The segmentation output for these marked iterations are shown in Subfigs. 6.2(e)-(g) for bone segmentation, in Subfigs. 6.2(h)-(k) for muscle segmentation and in Subfigs. 6.2(l)-(s) for fat segmentation. Notice both the adequateness of the first-maximum criterion, and the semantic value of contrast maxima.

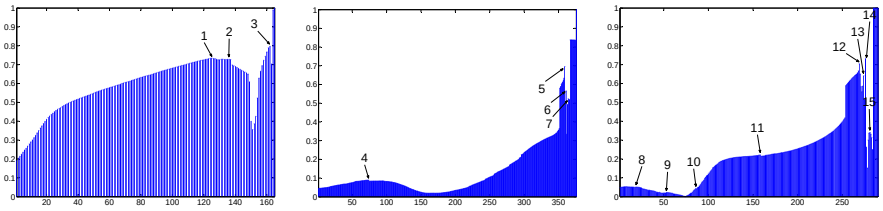

(a) Bone Segmentation Contrast

(b) Muscle Segmentation Contrast

(c) Fat Segmentation Contrast

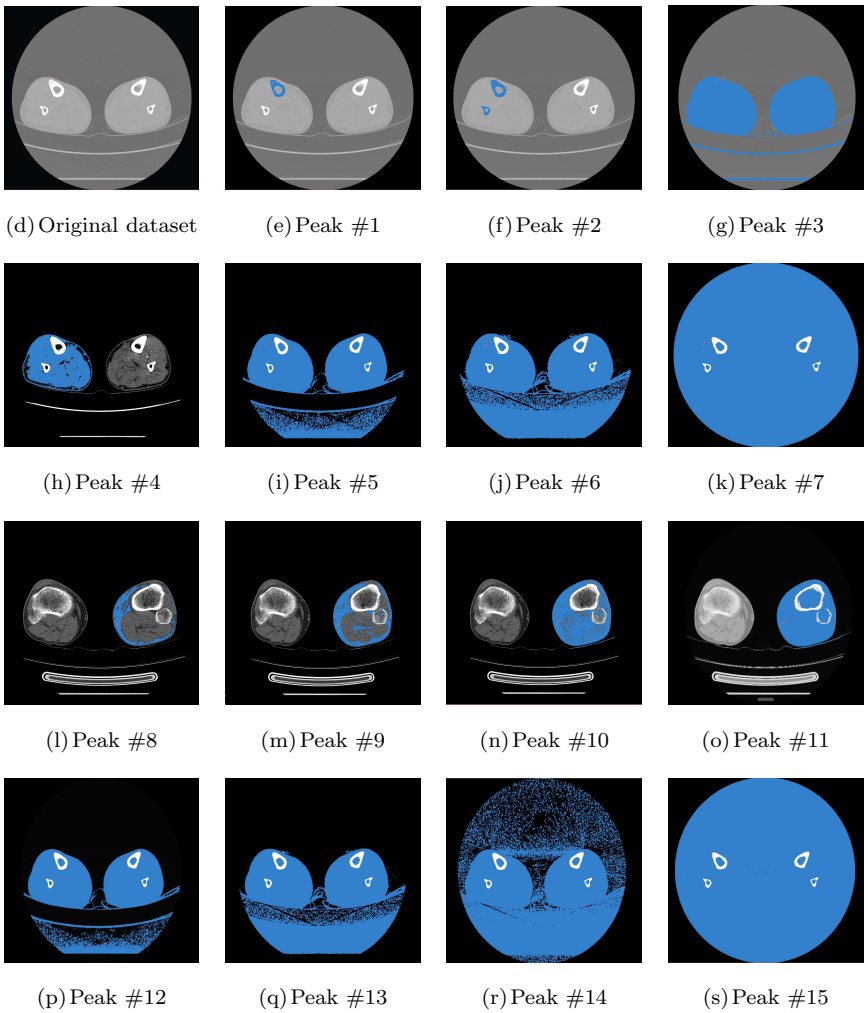

(d) Original dataset (e) Peak #1 (f) Peak #2 (g) Peak #3

(h) Peak #4 (i) Peak #5 (j) Peak #6 (k) Peak #7

(l) Peak #8 (m) Peak #9 (n) Peak #10 (o) Peak #11

(p) Peak #12 (q) Peak #13 (r) Peak #14 (s) Peak #15

Figure 6.2: Fat, muscle and bone contrast maxima. The areas in blue indicate segmentations for the arrow-marked maxima. Contrast curves are shown across growing number of iterations

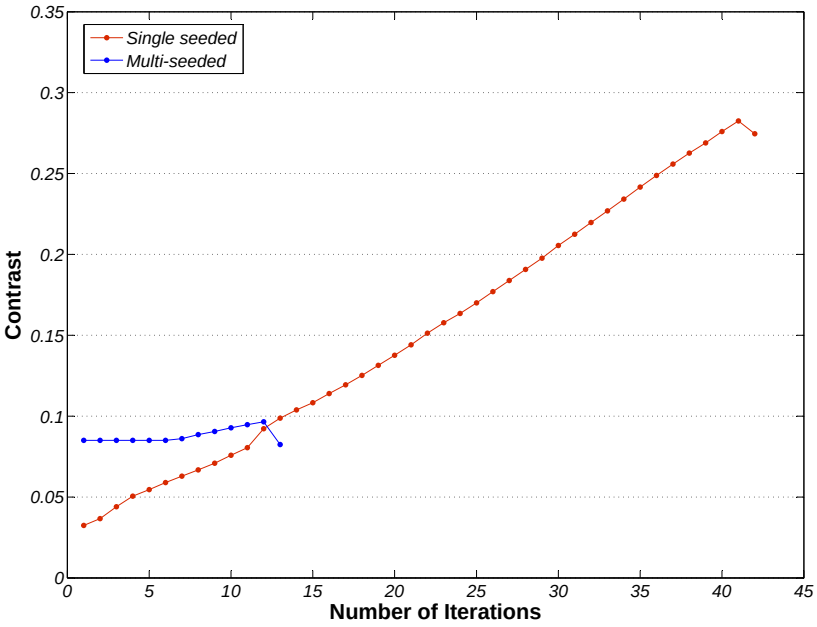

Figure 6.3: Contrast evolution comparison for head CT bone segmentation. Red curve depicts single seeding evolution, and blue curve does multiple seeding evolution

The adaptation of the sampling process to the characteristics of the tissue surrounding the seeds, allows for an interactive scheme, in which the user can decide to provide additional seeds after getting an incomplete solution, in an iterative manner. This approach has proven to be naturally accepted by the clinical practitioners on field, as they seem to prefer this intuitive way of incorporating their knowledge into the segmentation process. This is especially relevant as the variety of acquisition scenarios grows, like is the case for our domain of application.

To illustrate the effects of multiple seeding, we provide the region growing contrast evolution and growing sequence for a sample bone tissue segmentation in Figs. 6.3 and 6.4 until the first maximum is reached. Colors in Fig. 6.4 indicate iterations, and vary from yellow to violet as the total number is reached. The last iteration occurs earlier when using multiple seeds, as revealed by the smaller number of colors in Subfig. 6.4(c). Figure 6.3 shows how the first maximum is reached earlier, as the assessment function gets more coarsely sampled.

This adaptation of the sampling rate simultaneously results in less sensibility to spurious maxima and lower precision in the localization of the maximum of interest. So the greater number of seeds decreases the precision of the segmentation, but provides a solution for eventual incomplete segmentations that can occur for some of the noisier datasets, where spurious maxima can prematurely stop the algorithm. For color illustrations please refer to the electronic version of this document.

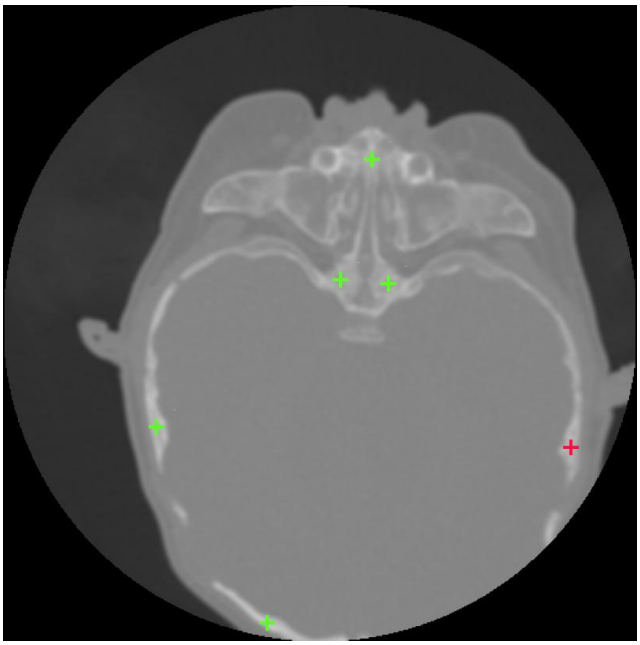

(a)

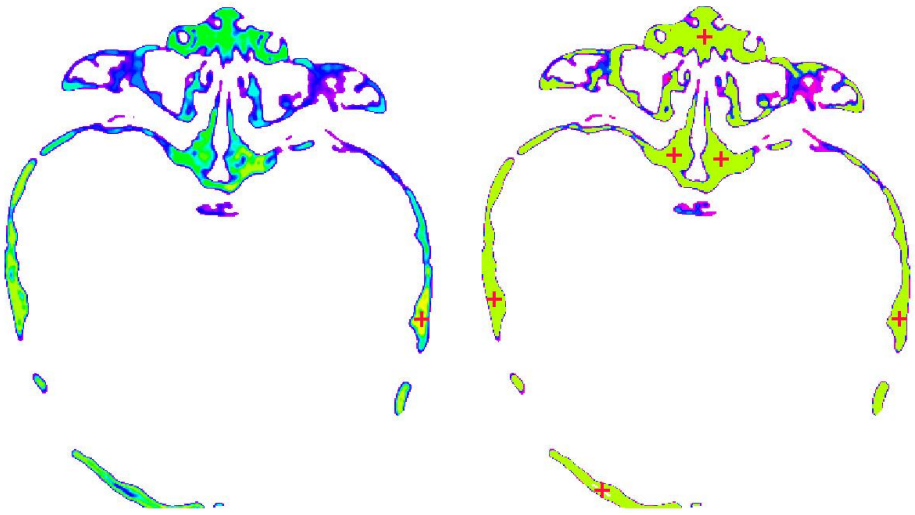

(b) (c)

Figure 6.4: Region growing sequence comparison for head CT bone segmentation. (a) Single and multiple seeding. Red cross-hairs is the single seed, green cross-hairs add to the red one for the multi-seed segmentation. (b) Region growing sequence for single seeding. (c) Region growing sequence for multiple seeding. (Colder colors represent higher iteration number outputs).

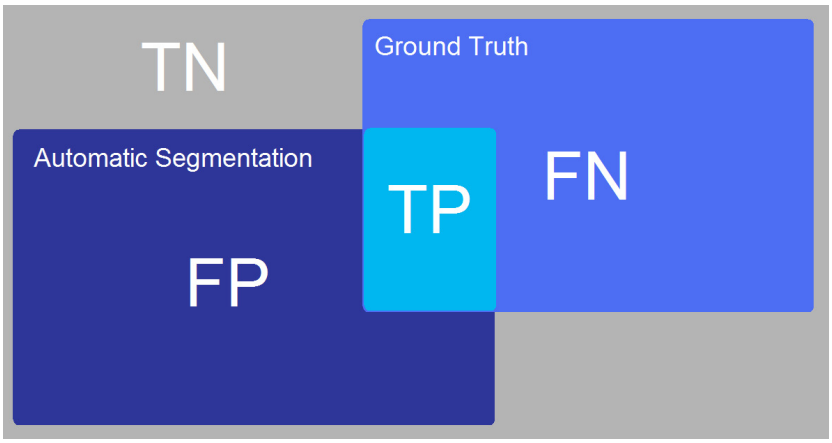

Figure 6.5: Sets for accuracy assessment.

In the following section, experimental validation is provided for both single and multiple seeding schemes.

6.3 Results

We have implemented our algorithm using open source medical image processing libraries, more precisely the Insight Toolkit [195] for algorithm development, and the command line executable module infrastructure provided by 3DSlicer for fast prototyping, calibration, evaluation, and manual segmentation [196]. The algorithm that we will validate, and that was finally implemented in the virtual reality platform that motivated its development, uses the following parameter values: $R = 2, K = 12, \Gamma = 1, k_0 = 1$, $\Delta k = 0.1$, $L = 3$ and B is the 3×3 binary cross structuring element.

To validate our algorithm we have proposed several experiments, based on synthetic and real CT datasets. In their inspiring work, Udupa et al. [197] deployed a methodology for the validation of medical volume segmentation methods. For a segmentation algorithm to be proven useful it has to demonstrate its accuracy (quality of results), precision (parameter independence) and efficiency (human and computational times). *Accuracy* is evaluated in terms of several classical measures, i.e. sensitivity (Sn), specificity (Sp), Dice's coefficient (D) [198], and Jaccard's index (J) [199]. All four measures are dependent on the concepts of True Positive (TP), True Negative (TN), False Positive (FP) and False Negative (FN) for a given segmentation and ground truth. See Fig. 6.5 for an example of the meaning of these concepts.

To produce such a ground truth a reference delineation of the object must be available. This delineation can be accomplished manually by a trained medical expert. Accuracy can also be assessed by subjective evaluation by an accredited observer in cases where manual delineation is impractical.

Sensitivity and specificity are widely-known, classical assessment quotients. They compute the proportion between detected truth and full truth. Furthermore,

Dice's coefficient and Jaccard's index are related measures that provide a combination of sensitivity and specificity characteristics.

$$\mathrm{Sn} = \frac{|\mathrm{TP}|}{|\mathrm{TP}| + |\mathrm{FN}|} \ , \tag{6.9}$$

$$\mathrm{Sp} = \frac{|\mathrm{TN}|}{|\mathrm{TN}| + |\mathrm{FP}|} \ , \tag{6.10}$$

$$\mathrm{D} = \frac{2|\mathrm{TP}|}{|\mathrm{FN}| + |\mathrm{FP}| + 2|\mathrm{TP}|} \ , \tag{6.11}$$

$$\mathrm{J} = \frac{|\mathrm{TP}|}{|\mathrm{FN}| + |\mathrm{FP}| + |\mathrm{TP}|} \ . \tag{6.12}$$

Precision is also evaluated according to the Jaccard's index applied on two different outputs rather than on a segmentation and a ground truth set. Precision can be computed in terms of inter/intra-operator variability and inter-scanner variability. Since our method relies on only a seed selection procedure, and is supposed to work for a variety of acquisition devices, we decided to compute precision for inter-seed variability. This variability is accounted for by comparing the resulting segmentation from seeds placed randomly inside the tissue of interest. Several seeds can be used so that J is computed for all possible combinations of outputs, and then averaged to obtain a more representative measure.

Efficiency relates to the segmentation performance time, human as well as computational time. According to Udupa et al. [197], it is extremely hard to provide an efficiency measure that proves useful when comparing different methods. One possible way of summing up all efficiency factors is related to the economic cost of usage for an algorithm. Human time is much more expensive than computer time. In our method, usage is designed to be extremely simple, and reduces to placing a handful of seeds on the desired object. For that reason we have computed here only computational times for the execution of our algorithm. The total usage time comprising loading of dataset, seed placement and algorithm execution, ranges from user to user, but seldom surpasses twice the computational time.

All computational times were recorded in a Windows PC with 2 GHz. Intel Core 2 Duo and 2 GB RAM, although our implementation is not multi-threaded. The average dataset size is 512×512×350.

6.3.1 Constant-valued spheres

To validate the claim that our contrast-based assessment function accurately detects homogeneous-intensity regions, we have created synthetic volume images and corrupted them with some typical CT acquisition artifacts. We have created a 3D volume composed by two ideal tissues, with constant intensity. The first tissue is shaped as a ball centered in the image domain, with radius $r = 20$ voxels. The second tissue is the background which extends to a final image domain with size $512 \times 512 \times 100$ voxels. We argue that this simple phantom is enough to test

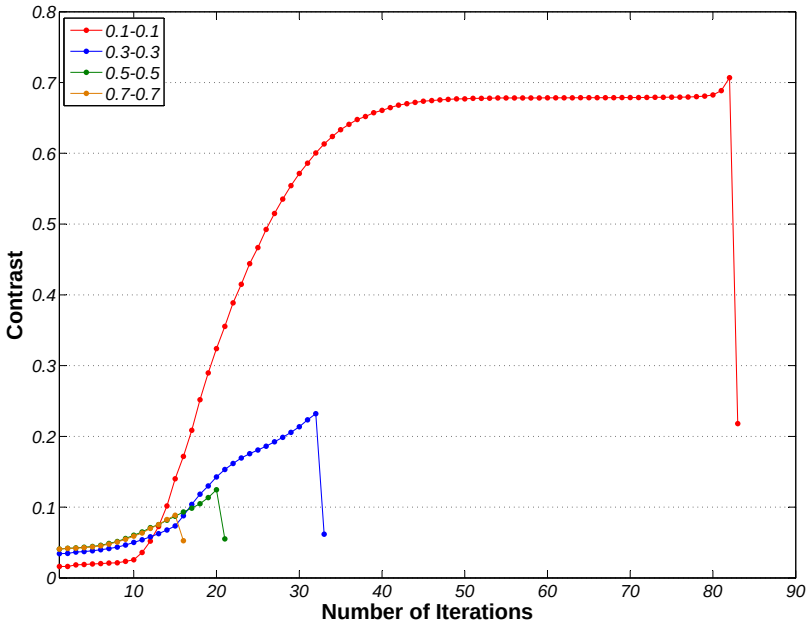

Figure 6.6: Contrast evolution for some constant-valued spheres

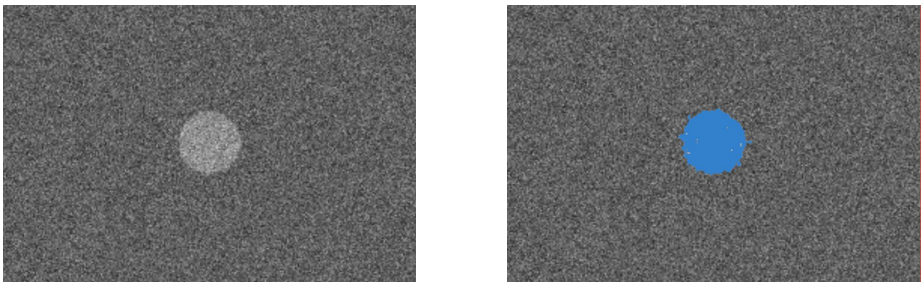

(a) (b)

Figure 6.7: Constant-valued sphere segmentation for $\sigma_b = 0.5$, $\sigma_n = 0.5$. (a) Slice of the test image. (b) Segmentation for the same slice.

the effect of artifacts on boundary detection as long as connectivity is preserved. Our method depends only on connectivity and intensity shifts, so the precise shape of the tissue is irrelevant as long as it is connected.

For simulating CT acquisition, we proceeded by blurring the image (accounting for partial volume effect) and adding Gaussian noise. Blurring was performed using a Gaussian smoothing kernel with width σ_b. Zero-mean Gaussian noise was generated with standard deviations σ_n. We produced segmentations for all combinations for $\sigma_b \in [0.1, 0.9]$ in increments of 0.2, and $\sigma_n \in [0.1L, 0.7L]$ (with L the absolute intensity difference between the two tissues, $L = 1$ in our experiment) in increments of 0.2.

Table 6.1: Computed measures for constant-valued spheres

σ_b-σ_n	Sensitivity	Specificity	Dice	Jaccard
0.1-0.1	1.0000	1.0000	0.9900	0.9802
0.1-0.3	0.9998	0.9998	0.9565	0.9165
0.1-0.5	0.9961	0.9997	0.9159	0.8448
0.1-0.7	0.9265	0.9999	0.9257	0.8618
0.3-0.1	1.0000	0.9998	0.9365	0.8805
0.3-0.3	0.9999	0.9998	0.9345	0.8770
0.3-0.5	0.9943	0.9997	0.9293	0.8680
0.3-0.7	0.9264	0.9998	0.9182	0.8488
0.5-0.1	1.0000	0.9997	0.9276	0.8650
0.5-0.3	0.9996	0.9998	0.9434	0.8928
0.5-0.5	0.9888	0.9998	0.9445	0.8949
0.5-0.7	0.9326	0.9998	0.9161	0.8452
0.7-0.1	1.0000	0.9998	0.9329	0.8743
0.7-0.3	1.0000	0.9995	0.8679	0.7666
0.7-0.5	0.9905	0.9998	0.9313	0.8714
0.7-0.7	0.9340	0.9998	0.9092	0.8335
0.9-0.1	1.0000	0.9997	0.9320	0.8727
0.9-0.3	1.0000	0.9996	0.8847	0.7933
0.9-0.5	0.9916	0.9997	0.9085	0.8323
0.9-0.7	0.9351	0.9997	0.8955	0.8108

Table 6.2: Average accuracy, precision and efficiency for constant-valued spheres

Avg. Sensitivity	0.9808 ± 0.0298
Avg. Specificity	0.9998 ± 0.0001
Avg. Dice	0.9250 ± 0.0260
Avg. Jaccard	0.8615 ± 0.0452
Precision	0.9250 ± 0.0413
Efficiency ($s.$)	72.6 ± 40.8

From all the segmentations we computed the aforementioned measures and show them in Table 6.1. For a representative case ($\sigma_b = 0.5$, $\sigma_n = 0.5$), we have computed precision measure **J** for all possible combinations of three different seeds. The average similarity according to **J** is presented in Table 6.2. For efficiency evaluation, computational time t_c has been computed and averaged across all images. We also display average values for the four measures in Table 6.2. For a representative case ($\sigma_b = 0.5$, $\sigma_n = 0.5$), we have computed similarity Jaccard's index for all possible combinations of three different seeds, which we present in Table 6.2. For efficiency evaluation, computational time has been recorded and averaged across all images. Notice in Table 6.2 how the experimental values for **Sn** and **Sp** are close to one, indicating very high segmentation fidelity. Precision is close to 1, indicating weak dependence on seed placement. Times show great variance due to the iterative nature of the algorithm.

For illustrative purposes we include in Fig. 6.6 a graphical representation of the

Table 6.3: Computed measures for continuous-valued spheres

σ_n	Sensitivity	Specificity	Dice	Jaccard
0.1	0.9375	1.0000	0.9617	0.9262
0.3	0.8543	0.9998	0.8791	0.7843
0.5	0.7491	0.9990	0.6813	0.5166

Table 6.4: Average accuracy, precision and efficiency for continuous-valued spheres

Avg. Sensitivity	0.8470 ± 0.0944
Avg. Specificity	0.9996 ± 0.0005
Avg. Dice	0.8407 ± 0.1441
Avg. Jaccard	0.7424 ± 0.2080
Precision	0.9300 ± 0.0176
Efficiency ($s.$)	257 ± 12.9

evolution of the assessment function as the algorithm iterates. See how the fall after the peak decreases as noise and blurring increase.

Also, in Fig. 6.7 we show a slice of the generated volume for the case 0.5-0.5 and the segmented region marked in blue over the image. Notice the good results facing noise with standard deviation as high as half the intensity difference between the two tissues.

6.3.2 Continuous-valued spheres

For this experiment we produced a similar synthetic image, only now the intensity inside the ball smoothly varies from 0 to 1 proportionally to the Euclidean distance to the center of the ball. The intensity value for the background was set to 1. In this scheme, no clear boundary is available, the reason is that we wanted to prove that our method does not require abrupt intensity changes, for boundaries to be detected. We corrupted the image only with Gaussian noise of standard deviation $\sigma_n = 0.1, 0.3$ and 0.5. We computed the same accuracy and efficiency measures, as well as precision for the case $\sigma_n = 0.3$. Due to the nature of the values in the regions, seeds must be placed close to the center in order for the condition (which is inherent to any region growing approach) of greater variance across than inside regions, to be met [186]. According to Tables 6.3 and 6.4, the results for this extremely subtle boundary are still acceptable. **Sn** and **Sp** stay somewhat close to 1, and precision is close enough to 1 as to support the claim of low seed location dependence. Time has increased due to the greater variance of the segmented tissue, which forcer the algorithm to perform more iterations, so that greater frequency maxima can be detected.

For Fig. 6.8 we can observe the same effect as in Fig. 6.6. Notice the increased roughness in these curves as compared to those in Fig. 6.6, especially in the earlier iterations. This is due to a greater influence of noise on consecutive iterations of the region growing sequence, due to the non-constant intensity of the tissue. This effect has dramatic consequences on the contrast evolution for the case $\sigma_n = 0.1$, where the low value of noise together with the smoothness

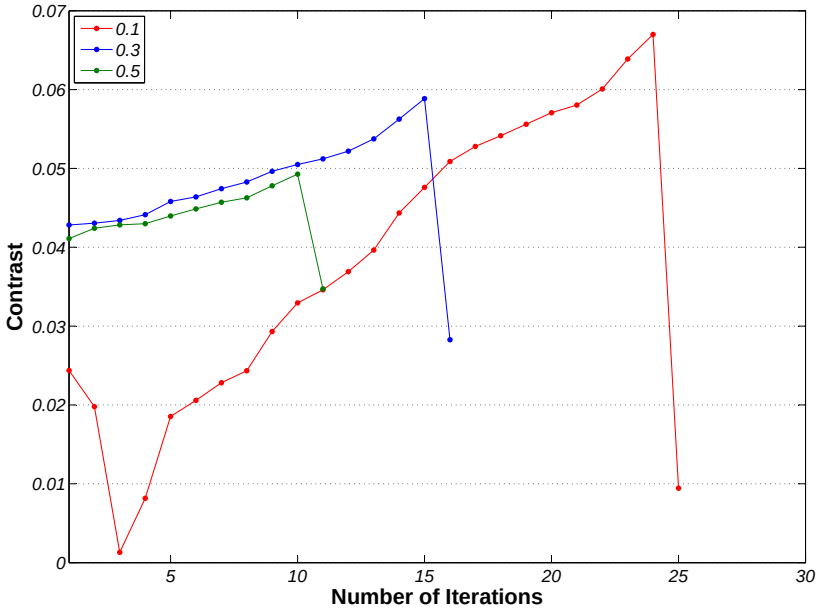

Figure 6.8: Contrast evolution for all continuous-valued spheres

of the variation produces, after normalization, significant instability for early iterations. Notice that this a limit case, as our tissues of interest display almost constant intensity (apart from noise), rather than linearly varying intensity.

We present in Fig. 6.9 again a slice of the generated volume for the case 0.5 and its segmentation output. The quality of the segmentation is pretty good even for extremely dim boundaries.

6.3.3 Ground truth CT images

For this experiment we have produced automatic segmentations using a set of real CT images for one of the described tissues (muscle, fat and bone). The testing set proceeds from three different scanners present in our clinical setting (a LightSpeed16 by General Electrics Medical Systems, Milwaukee, Wisconsin USA; an Aquilion by Toshiba Medical Systems Company, Tokyo, Japan; and an AVPS by Philips Medical Systems, Best, the Netherlands). We found almost no coincidences between datasets regarding reconstruction kernel, slice thickness, and intensity windowing. Some of them presented contrast agents in some way.

As explained above, validation of real CT images requires manual segmentations provided by a clinical expert. In our application context this manual segmentation process can be extremely time-consuming, or even intractable, due to considerable tissue delocalization, e.g. manual segmentation of muscular tissue implies manually avoiding all blood vessels and fat traces, for up to 500 slices. For this reason we have computed our accuracy and precision metrics from an average of 20 evenly-spaced slices, in 10 cases.

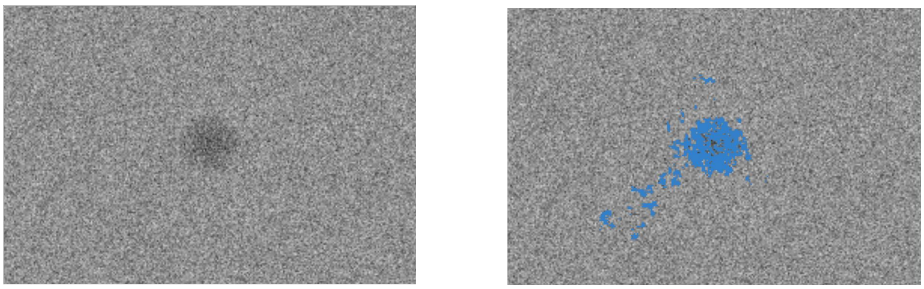

(a) (b)

Figure 6.9: Continuous-valued sphere segmentation for $\sigma_n = 0.5$. (a) Slice of the test image. (b) Segmentation for the same slice.

Moreover, the manual accuracy of the segmentation is biased by human high-level knowledge, presenting considerable inter-subject variability, and we (the authors and the clinical practitioners) have observed that in many cases poorer results in accuracy are related to incomplete manual segmentations, rather than incomplete automatic segmentations. Let us say then, that the quality of the segmentation is *at least* as good as the presented results. See in Fig. 6.10 a cropped comparison sample showing discrepancies between our segmentation output and the manual delineation provided. For the results presented in

Table 6.5: Accuracy metrics for all CT datasets

	Sensitivity	Specificity	Dice	Jaccard
Case 1	0.884	0.998	0.903	0.824
Case 2	0.967	0.996	0.949	0.902
Case 3	0.783	0.999	0.853	0.743
Case 4	0.828	0.951	0.807	0.676
Case 5	0.650	1.000	0.787	0.649
Case 6	0.869	1.000	0.928	0.866
Case 7	0.744	0.999	0.731	0.576
Case 8	0.988	1.000	0.929	0.867
Case 9	0.702	0.997	0.777	0.635
Case 10	0.805	0.987	0.788	0.651

Tables 6.5 and 6.6, all segmentations have been used for accuracy and efficiency assessment, and one particular segmentation and several seeds for precision. While specificity stays very high, ensuring self-contained segmented regions, sensitivity is still reasonably close to 1. This prevalence of specificity satisfies our domain of application, since surgical planning depends strongly on boundaries, and incompleteness of our segmentations usually remain in the inner part of the regions. Due to the connected nature of our output regions, over-segmentation would necessarily entail boundary alteration. Computational time ranges between 2 or 3 minutes, which implies a great reduction as compared to previous trial-and-error parameter tuning, according to non-technical users' opinions.

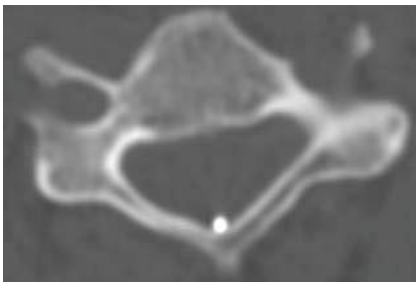

(a)

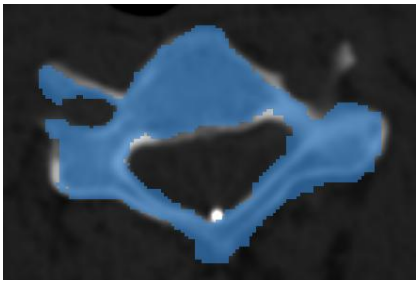

(b)

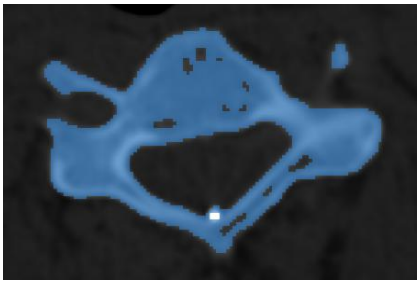

(c)

Figure 6.10: Close-up comparison of manual segmentation and automatic segmentation. (a) Original caption. (b) Manual segmentation. (c) Automatic segmentation.

6.3.4 Ground truth CT samples

In an attempt to circumvent the inherent difficulty of providing manual segmentations for our very extensive regions of interest, we have developed a more tractable experiment. In this evaluation strategy we made use of partial volume samples from a new set of 10 segmented CT scans. As before, we have performed segmentation for bone, fat and muscle tissue indifferently on these 10 sets, but instead of comparing with manual delineations of full slices, we have extracted small regions of interest with size $20(\text{axial}) \times 40 \times 40$. The reason is that for such smaller regions, manual delineation can be produced by our expert with much greater precision. For a comparison between manual/automatic delineations in small samples see Fig. 6.11.

Table 6.6: Average accuracy, precision and efficiency for CT datasets

Avg. Sensitivity	0.822 ± 0.109
Avg. Specificity	0.993 ± 0.015
Avg. Dice	0.845 ± 0.077
Avg. Jaccard	0.739 ± 0.117
Precision	0.733 ± 0.171
Efficiency (*s.*)	156.0 ± 36.2

Table 6.7: Accuracy metrics for all CT samples

	Sensitivity	Specificity	Dice	Jaccard
Sample 1	0.891	0.986	0.936	0.881
Sample 2	0.928	0.985	0.955	0.914
Sample 3	0.982	0.927	0.845	0.732
Sample 4	0.996	0.867	0.960	0.923
Sample 5	0.985	0.974	0.907	0.830
Sample 6	0.986	0.983	0.961	0.924
Sample 7	0.964	0.947	0.973	0.948
Sample 8	0.988	0.958	0.941	0.888
Sample 9	0.943	0.958	0.933	0.875
Sample 10	0.948	0.983	0.970	0.942

Table 6.8: Average accuracy, precision and efficiency for CT samples

Avg. Sensitivity	0.961 ± 0.0334
Avg. Specificity	0.957 ± 0.0370
Avg. Dice	0.938 ± 0.0382
Avg. Jaccard	0.886 ± 0.0646

For quantitative evaluation we have computed the values of sensitivity, specificity, Jaccard's index and Dice's coefficient as described at the beginning of this section. See the computed measures in table 6.7 for each of the concerned datasets. We display in table 6.8 the average results for this validation experiment. Notice how the use of manageable regions of interest results in greater performance of the algorithm, since the obtention of the ground truth is now trivial.

6.3.5 Subjective evaluation of real CT cases (Multi-seed scheme)

For complementary accuracy assessment we provide also a subjective evaluation performed by a clinical expert in surgery (a user of the surgical planning platform under development) on 35 datasets. These images proceed from the scanners enumerated in Subsect. 6.3.3, and also present differences in most imaging acquisition parameters previously described.

Thirty-five segmentations of muscle, fat and bone were performed randomly on the datasets. In this case the multiple seeding scheme was used in a maximum of two seed placement iterations, as described in Subsect. 6.2.2. The computational time referred below includes both iterations when applicable.

We required our expert to evaluate the percentage of slices in the output segmentation, that required further modifications in order to serve the purpose of surgical planning for the body region comprised in the dataset. We gave him instructions to classify segmentation as Excellent if 100-75% of the slices were good enough, Good for 75-50%, Acceptable for 50-25%, and Useless for 25-0%. We also asked him to provide detailed comments on any non-Excellent

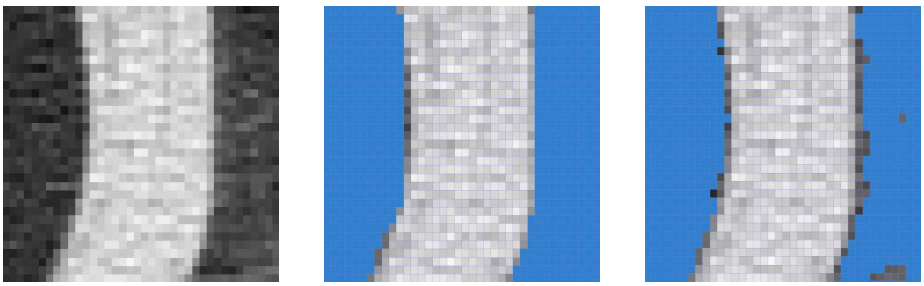

(a) (b) (c)

Figure 6.11: Comparison of manual segmentation and automatic segmentation for the axial view of a sample. (a) Original sample. (b) Manually delineated sample. (c) Segmentation output sample.

Table 6.9: Subjective assessment for segmentation of real CT images

Correct slices (%)	100-75%	75-50%	50-25%	25-0%	t_c(s)
Bone Tissue	76.5%	23.5%	0%	0%	52.3±18.3
Fat Tissue	85.8%	7.1%	7.1%	0%	117.5±27.0
Muscle Tissue	62.6%	37.4%	0%	0%	141.6±48.8

segmentations, for future improvements of the algorithm.

See in Fig. 6.12 some examples of the obtained outputs. First column is for fat segmentation, second for muscle, and third for bone. Three-dimensional surface models obtained by means of the marching cubes algorithm [200], as well as different views are provided. Notice that neither the varying resolution nor the movement artifacts prevented the overall correctness of results.

Notice in Table 6.9 the very good subjective assessment obtained for most test datasets. Just one segmentation scored below Good for any of the tissues involved, and that should be considered in the context of varying scanners and imaging conditions. Besides these results were obtained in reasonable computational times and with minimal user intervention (two multiple-seeding iterations at most).

Regarding the few cases with non-Excellent qualification the main comments made by the observer concerned issues like poor image quality in the test dataset for muscle and fat segmentation, or abnormal tissue intensity distribution for bone segmentation (Osteoporosis condition). The interest of this kind of subjective assessment is based in the definition of the evaluation. In this case, the evaluation is made taking in consideration the application for which this technique was developed.

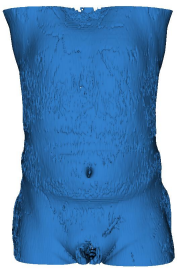

(a) Fat. Surface rendering.

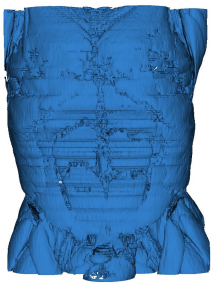

(b) Muscle. Surface rendering.

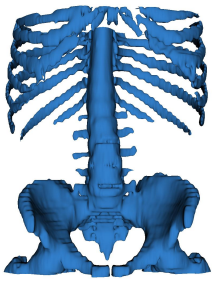

(c) Bone. Surface rendering.

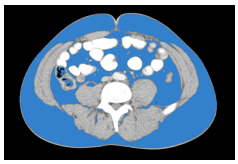

(d) Fat. Axial view.

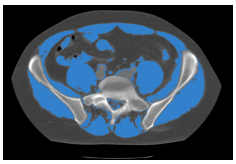

(e) Muscle. Axial view.

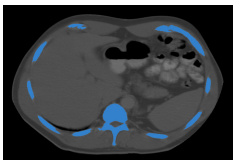

(f) Bone. Axial view.

(g) Fat. Saggital view.

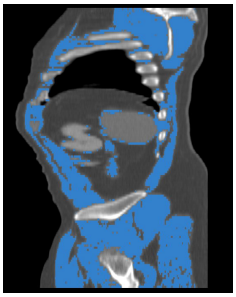

(h) Muscle. Saggital view.

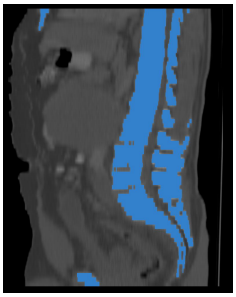

(i) Bone. Saggital view.

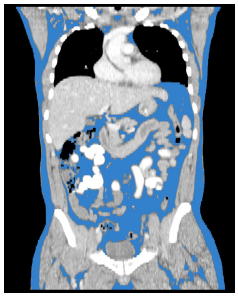

(j) Fat. Coronal view.

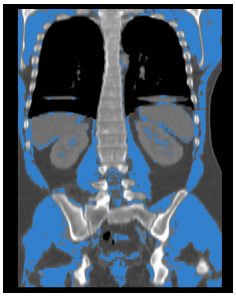

(k) Muscle. Coronal view.

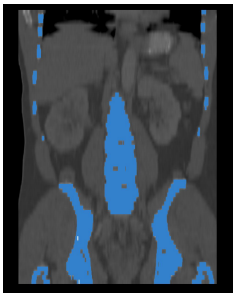

(l) Bone. Coronal view.

Figure 6.12: Fat, muscle and bone segmentation examples. The blue region is the segmentation output.

6.3.6 Performance of our technique once integrated in virtual reality platform VirSSPA

According to our field inquiries, our segmentation technique (that we integrated with the virtual reality surgical planning viewer VirSSPA) has produced dramatic time reduction in surgical planning. Before our algorithm was available for platform VirSSPA, segmentation was usually performed using either rough manual delineation, or iterative threshold selection techniques highly dependent on user interaction. Now, the developed technique is able to produce very precise segmentations just from a couple seeds, which can be introduced quickly and trivially by any operator, thus reducing the cost and burden of the surgical planning cycle.

Once the whole tissue of interest has been obtained, a surface rendering is produced through a simple marching cubes technique [200], and then the surgeon in charge of the surgical planning proceeds by 3D manipulation, excision and replacement of different parts of the rendered model. The accuracy of virtual-reality based surgical planning procedures using VirSSPA, exemplified by deep inferior epigastric artery perforator (DIEP) flap surgery, has extensively been demonstrated in [201–203].

Recently, VirSSPA-based surgical planning has been a key factor in successfully performing the first face transplant ever performed in Andalusia (second in Spain, and ninth in the world). The surgical process was simulated using surface models of the skin, muscle, fat, bone and vessels, most of which were segmented using the presented technique.

6.4 Conclusion

Our work is basically an attempt to generalize a classical image processing methodology, so it deals properly with real imaging-condition variations. Few efforts have been pursued to achieve this kind of robustness, as most methods are either manually tuned or based on prior unrealistic assumptions that only work for a given set of imaging conditions. Considering the numeric results for the experimental validation, we consider our approach successful in solving the particular needs for which it was conceived. The algorithm has been integrated in the reference platform and prevents from previous trial-and-error segmentation, which was very time-consuming according to its users. Its greatest advantage is thus the absence of tuning parameters and ability to produce nice results for a wide set of acquisition devices, with minimal user intervention, in reasonable time frames. This is founded in the use of our adaptively-sampled contrast measure, and in the normalizing strategy that allows for generalization of the contrast sampling rate.

The most significant limitation to this region growing approach has to do with the fact that connectivity is sometimes too weak as a requirement for some applications (tumor segmentation, organ segmentation...), as the region of interest may be connected to other similar-intensity regions. For this reason, future improvement for the technique could consist of incorporating some morpholog-

ical limitations to the growth of the region in order to impose some degree of *stiffness*, and to avoid flooding towards adjacent, slightly connected regions. This improvement could make the algorithm useful in greater variety of surgical planning scenarios.

Besides this regularization, another field of exploration consists of transposing our assessment measure into other segmentation paradigms, like watersheds or deformable surfaces, allowing for automatization of these other schemes, which rely on manual tuning and intervention for the obtention of adequate results.

Chapter 7

Conclusion

In the preceding Chapters we have presented our work on applying image processing to serve the fundamental goals of healthcare.

In the pursuit for better understanding COPD, we have developed a pattern recoginition scheme that allows for computing the relative area of six emphysema classes usually encountered in the COPD lung. Our approach is simpler than texture analysis techniques while obtaining similar results. We have proven that the current gap between clinical-practice densitometry and impractical time-consuming texture analysis can be abridged by the use of local intensity distributions. The demonstrated approach is more intuitive, and since histogram sparsity is dealt with by non-parametric methods, it is well suited for emphysema analysis in complex multi-scanner scenarios like the one presented. It can be seen in our results, that new interesting lessons about emphysematous disease can be learnt using this simpler approach.

Ultimately, our technique is susceptible of being incorporated in clinical practice, once some minor aspect are taken care for, and further studies provide a model of the relation between tissue percentages and different PFTs or quality of life indicators. COPD patients can beneffit from fully-automatic tissue percentage computations, which is much richer a description of the pulmonary condition than current densitometric approaches and can finely assess the response to therapy or the correlation with genetics.

We have also introduced our work on buiding pathways toward automatically detecting and diagnosis the malignancy of pigmented lesions of the skin.

In a first step, lesion segmentation is tackled using our original active contour technique. We are the first authors to ever propose active contours capable of maximizing cross-bin histogram dissimilarity of the enclosed objects in consideration of multi-dimensional features, like color. We have demonstrated the ability of our general-purpose framework to discern between color distributions in comparison with bin-to-bin dissimilarity active contours. Some of the advantages of our methodology include better discrimination between color signatures of the objects of interest, as well as better convergence properties.

In the future we plan to incorporate other segmentation criteria beyond maximal discrepancy into the framework, and to test our technique for discrimination of textured regions by substituting color features by texture features.

Subsequently we have presented a texture classification technique which, in combination with lesion segmentation and lesion sampling, is capable of detecting pattern variations inside a melanocytic lesion. Our texture description is based on a MRF modelisation of some of the basic patterns usually encountered in this type of skin lesion. Feature extraction is then assimilated as a parameter estimation problem in which color inter-plane dependencies have been explicitly accounted for. The resulting feature space allows for classification of a grid of samples from unseen lesions. We produce charts of pattern variations which could assist dermatologists in assessing the malignancy of the lesion, and may set the foundations for a future computer-assisted diagnosis system.

Some of the future lines of work include extending the texture classification scheme to more of the existing melanocytic patterns. Also, it shall be useful to have access to a larger set of diagnosed dermoscopic images in order to provide a model of the relation between class percentages and the probability of malignancy. Furthermore, the pertinence of scale or rotation invariance should be explored when discriminating textures, as texture irregularity is a preferred cue for the assessment of malignancy of pigmented lesions of the skin.

Finally, we have introduced our contribution to a virtual-reality surgical planning platform. We developed a segmentation technique for CT scans allowing for automatic delineation of structures of interest to the planning of plastic surgery interventions. Our work is basically an attempt to generalize a classical image processing methodology, so it deals properly with real imaging-condition variations. Considering the numeric results for the experimental validation, we consider our approach successful in producing a turn-key solution to the particular needs for which it was conceived. The algorithm has been integrated in the reference platform and prevents from previous trial-and-error segmentation, which was very time-consuming according to its users. Its greatest advantage is thus the absence of tuning parameters and ability to produce accurate results for a wide set of acquisition devices, with minimal user intervention (just a couple of seeds), in reasonable time frames.

The most signifficant limitation to our region growing approach has to do with the fact that connectivity is sometimes too weak as a requirement for some applications (tumor segmentation, organ segmentation...), as the region of interest may be connected to other similar-intensity regions. For this reason, future improvement for the technique could consist of incorporating some regularization term in order to impose some degree of stiffness, and to avoid flooding towards adjacent, partially connected regions. This improvement could make the algorithm useful in greater variety of surgical planning scenarios beyond plastic surgery.

Publications

Journal Articles

- C.S. Mendoza, B. Acha, C. Serrano, and T. Gómez-Cía, "Fast parameter-free region growing segmentation with application to surgical planning," *Machine Vision and Applications*, article in press.

- C. S. Mendoza, G. R. Washko, J. C. Ross, A. A. Diaz, D. A. Lynch, J. D. Crapo, E. K. Silverman, C. Serrano, B. Acha and R. San José Estépar, "Emphysema quantification in multi-scanner HRCT using local intensity distributions," submitted to *IEEE Transactions on Medical Imaging.*

- C. S. Mendoza, B. Acha, C. Serrano, "Linearized multi-dimensional earth mover's distance gradient flows," submitted to *IEEE Transactions on Image Processing.*

Conference Communications

- C.S. Mendoza, C. Serrano, and B. Acha, "Pattern analysis of dermoscopic images based on FSCM color Markov random fields," *Lecture Notes in Computer Science (including subseries Lecture Notes in Artificial Intelligence and Lecture Notes in Bioinformatics)*, vol. 5807 LNCS, pp. 676–685, 2009.

- C.S. Mendoza, B. Acha, C. Serrano, and T. Gómez-Cía, "Self-assessed contrast-maximizing adaptive region growing," *Lecture Notes in Computer Science (including subseries Lecture Notes in Artificial Intelligence and Lecture Notes in Bioinformatics)*, vol. 5807 LNCS, pp. 652–663, 2009.

- C.S. Mendoza, C. Serrano, and B. Acha, "Scale invariant descriptors in pattern analysis of melanocytic lesions," *Proceedings - International Conference on Image Processing, ICIP 2009*, pp. 4193–4196, 2009.

- C.S. Mendoza, B. Acha, C. Serrano, "Maximal Contrast Adaptive Region Growing for CT Airway Tree Segmentation," In M. Brown, M. de Bruijne, B. van Ginneken, A. Kiraly, J.-M. Kuhnigk, C. Lorenz, K. Mori, and J. M.

Reinhardt, editors, *Second International Workshop on Pulmonary Image Analysis.* pp. 285-295, 2009.

- C.S. Mendoza, G. Bohórquez-Ruiz, B. Acha and C. Serrano, "Multidimensional earth movers distance active contours," submitted to *International Conference on Image Processing, ICIP 2011.*

- C. S. Mendoza, G. R. Washko, J. C. Ross, A. A. Diaz, D. A. Lynch, J. D. Crapo, E. K. Silverman, C. Serrano, B. Acha and R. San José Estépar, "Emphysema Quantification in Multi-Scanner HRCT Using Local Intensity Distributions," submitted to *Medical image computing and computer-assisted intervention : MICCAI International Conference on Medical Image Computing and Computer-Assisted Intervention 2011.*

Spanish Patents

- Automatic procedure for tissue segmentation via region growing. Patent P201030710. Pending approval.

- Anatomical structure retrieval for surgical grafting: query algorithm. Patent P201030637. Pending approval.

Bibliography

[1] I. H. Bankman, Ed., *Handbook of Medical Image Processing and Analysis*. Academic Press, 2009.

[2] T. Liu, H. Peng, and X. Zhou, "Imaging informatics for personalised medicine: applications and challenges," *International Journal of Function Informatics and Personalised Medicine*, vol. 2, no. 2, pp. 125–135, 2009.

[3] COPDGene Website. [Online]. Available: http://www.copdgene.org/

[4] M. B. Lanktree, R. G. Hassell, P. Lahiry, and R. A. Hegele, "Phenomics: Expanding the role of clinical evaluation in genomic studies," *Journal of Investigative Medicine*, vol. 58, no. 5, pp. 700–706, 2010.

[5] Y. A. Lussier and Y. Liu, "Computational approaches to phenotyping: High-throughput phenomics," *Proceedings of the American Thoracic Society*, vol. 4, no. 1, pp. 18–25, 2007.

[6] D. Houle, D. R. Govindaraju, and S. Omholt, "Phenomics: The next challenge," *Nature Reviews Genetics*, vol. 11, no. 12, pp. 855–866, 2010.

[7] J. Rittscher, *Characterization of biological processes through automated image analysis*. Annual Reviews, 2010, vol. 12.

[8] J. Ley-Zaporozhan and E. J. R. V. Beek, "Imaging phenotypes of chronic obstructive pulmonary disease," *Journal of Magnetic Resonance Imaging*, vol. 32, no. 6, pp. 1340–1352, 2010.

[9] S. A. Al-Attar, R. L. Pollex, J. F. Robinson, B. A. Miskie, R. Walcarius, C. H. Little, B. K. Rutt, and R. A. Hegele, "Quantitative and qualitative differences in subcutaneous adipose tissue stores across lipodystrophy types shown by magnetic resonance imaging," *BMC Medical Imaging*, vol. 7, 2007.

[10] S. R. Hopkins and G. K. Prisk, "Lung perfusion measured using magnetic resonance imaging: New tools for physiological insights into the pulmonary circulation," *Journal of Magnetic Resonance Imaging*, vol. 32, no. 6, pp. 1287–1301, 2010.

[11] S. Lagerholm, H. B. Park, H. Luthman, M. Nilsson, F. McGuigan, M. Swanberg, and K. Akesson, "Genetic loci for bone architecture determined by three-dimensional CT in crosses with the diabetic GK rat," *Bone*, vol. 47, no. 6, pp. 1039–1047, 2010.

[12] R. W. W. Lee, K. Sutherland, A. S. L. Chan, B. Zeng, R. R. Grunstein, M. A. Darendeliler, R. J. Schwab, and P. A. Cistulli, "Relationship between surface facial dimensions and upper airway structures in obstructive sleep apnea," *Sleep*, vol. 33, no. 9, pp. 1249–1254, 2010.

[13] T. M. O'Connell and P. B. Watkins, "The application of metabonomics to predict drug-induced liver injury," *Clinical pharmacology and therapeutics*, vol. 88, no. 3, pp. 394–399, 2010.

[14] M. A. Kurian, Y. Li, J. Zhen, E. Meyer, N. Hai, H. J. Christen, G. F. Hoffmann, P. Jardine, A. von Moers, S. R. Mordekar, F. O'Callaghan, E. Wassmer, E. Wraige, C. Dietrich, T. Lewis, K. Hyland, S. J. R. Heales, T. Sanger, P. Gissen, B. E. Assmann, M. E. A. Reith, and E. R. Maher, "Clinical and molecular characterisation of hereditary dopamine transporter deficiency syndrome: An observational cohort and experimental study," *The Lancet Neurology*, vol. 10, no. 1, pp. 54–62, 2011.

[15] M. L. Giger, H. P. Chan, and J. Boone, "Anniversary paper: History and status of cad and quantitative image analysis: The role of medical physics and AAPM," *Medical physics*, vol. 35, no. 12, pp. 5799–5820, 2008.

[16] S. Yu and L. Guan, "A cad system for the automatic detection of clustered microcalcifications in digitized mammogram films," *IEEE Transactions on Medical Imaging*, vol. 19, no. 2, pp. 115–126, 2000.

[17] B. Sahiner, H.-P. Chan, L. Hadjiiski, M. Helvie, C. Paramagul, J. Ge, J. Wei, and C. Zhou, "Joint two-view information for computerized detection of microcalcifications on mammograms," *Medical Physics*, vol. 33, no. 7, pp. 2574–2585, 2006.

[18] C. Kimme, B. O'Loughlin, and J. Sklansky, "Automatic detection of suspicious abnormalities in breast radiographs," *Data Structures, Computer Graphics, and Pattern Recognition*, pp. 427–447, 1975.

[19] S.-M. L. Lai and W. F. Xiaoboand Bischof, "On techniques for detecting circumscribed masses in mammograms," *IEEE Transactions on Medical Imaging*, vol. 8, no. 4, pp. 377–386, 1989.

[20] P. Carson, G. Lecarpentier, M. Roubidoux, R. Erkamp, J. Fowlkes, and M. Goodsitt, "Physics and technology of breast us imaging including automated three-dimensional us," *Advances in Breast Imaging: Physics, Technology, and Clinical Applications-Categorical Course in Diagnostic Radiology Physics*, pp. 223–232, 2004.

[21] H.-P. Chan, J. Wei, B. Sahiner, E. Rafferty, T. Wu, M. Roubidoux, R. Moore, D. Kopans, L. Hadjiiski, and M. Helvie, "Computerized detection of masses on digital tomosynthesis mammograms -a preliminary study," *Proceedings of the 7th International Workshop on Digital Mammography*, pp. 199–202, 2004.

[22] S. Katsuragawa, K. Doi, and H. MacMahon, "Image feature analysis and computer-aided diagnosis in digital radiography: Detection and characterization of interstitial lung disease in digital chest radiographs," *Medical Physics*, vol. 15, no. 3, pp. 311–319, 1988.

[23] T. Ishida, S. Katsuragawa, T. Kobayashi, H. MacMahon, and K. Doi, "Computerized analysis of interstitial disease in chest radiographs: Improvement of geometric-pattern feature analysis," *Medical Physics*, vol. 24, no. 6, pp. 915–924, 1997.

[24] S. Sanada, K. Doi, and H. MacMahon, "Image feature analysis and computer-aided diagnosis in digital radiography: Automated detection of pneumothorax in chest images," *Medical Physics*, vol. 19, no. 5, pp. 1153–1160, 1992.

[25] B. Sahiner, Z. Ge, H. Chan, L. Hadjiiski, N. Bogot, P. Cascade, and E. Kazerooni, "False positive reduction using hessian features in computer-aided detection of pulmonary nodules on thoracic CT images," *Proceedings of the SPIE-Medical Imaging Annual Meeting 2005*, 2005.

[26] K. Marten and C. Engelke, "Computer-aided detection and automated CT volumetry of pulmonary nodules," *European Radiology*, vol. 17, no. 4, pp. 888–901, 2007.

[27] K. Suzuki, H. Yoshida, J. Nappi, and A. Dachman, "Massive-training artificial neural network (MTANN) for reduction of false positives in computer-aided detection of polyps: Suppression of rectal tubes," *Medical Physics*, vol. 33, no. 10, pp. 3814–3824, 2006.

[28] S. Taylor, S. Halligan, D. Burling, M. Roddie, L. Honeyfield, J. McQuillan, H. Amin, and J. Dehmeshki, "Computer-assisted reader software versus expert reviewers for polyp detection on CT colonography," *American Journal of Roentgenology*, vol. 186, no. 3, pp. 696–702, 2006.

[29] L. Zhao, C. Botha, J. Bescos, R. Truyen, F. Vos, and F. Post, "Lines of curvature for polyp detection in virtual colonoscopy," *IEEE Transactions on Visualization and Computer Graphics*, vol. 12, no. 5, pp. 885–892, 2006.

[30] K. Horsch, M. Giger, C. Vyborny, L. Lan, E. Mendelson, and R. Hendrick, "Classification of breast lesions with multimodality computer-aided diagnosis: Observer study results on an independent clinical data set," *Radiology*, vol. 240, no. 2, pp. 357–368, 2006.

[31] Z. Huo, M. Giger, C. Vyborny, and C. Metz, "Breast cancer: Effectiveness of computer-aided diagnosis - observer study with independent database of mammograms," *Radiology*, vol. 224, no. 2, pp. 560–568, 2002.

[32] J. Gurney and S. Swensen, "Solitary pulmonary nodules: Determining the likelihood of malignancy with neural network analysis," *Radiology*, vol. 196, no. 3, pp. 823–829, 1995.

[33] K. Nakamura, M. Yoshida, R. Engelmann, H. MacMahon, S. Katsuragawa, T. Ishida, and D. K. Ashizawa, K., "Computerized analysis of the likelihood of malignancy in solitary pulmonary nodules with use of artificial neural networks," *Radiology*, vol. 214, no. 3, pp. 823–830, 2000.

[34] M. Aoyama, Q. Li, S. Katsuragawa, H. MacMahon, and K. Doi, "Automated computerized scheme for distinction between benign and malignant solitary pulmonary nodules on chest images," *Medical Physics*, vol. 29, no. 5, pp. 701–708, 2002.

[35] G. Fichtinger, P. Kazanzides, A. M. Okamura, G. D. Hager, L. L. Whitcomb, and R. H. Taylor, "Surgical and interventional robotics: Part II," *IEEE Robotics and Automation Magazine*, vol. 15, no. 3, pp. 94–102, 2008.

[36] Q. H. Li, L. Zamorano, A. Pandya, R. Perez, J. Gong, and F. Diaz, "The application accuracy of the NeuroMate robot - a quantitative comparison with frameless and frame-based surgical localization systems," *Computer Aided Surgery*, vol. 7, no. 2, pp. 90–98, 2002.

[37] A. T. Stadie, R. A. Kockro, R. Reisch, A. Tropine, S. Boor, P. Stoeter, and A. Perneczky, "Virtual reality system for planning minimally invasive neurosurgery. Technical note," *Journal of Neurosurgery*, vol. 108, no. 2, pp. 382–394, 02/01 2008.

[38] K. Cleary and T. M. Peters, *Image-guided interventions: Technology review and clinical applications*, 2010, vol. 12.

[39] T. Peters and K. Cleary, *Image-Guided Interventions: Technology and Applications*. Springer-Verlag, 2008.

[40] R. H. Taylor, A. Menciassi, G. Fichtinger, and P. Dario, "Medical robots and systems," *Springer Handbook of Robotics*, 2008.

[41] G. Fichtinger, J. Fiene, C. Kennedy, I. Iordachita, G. Kronreif, D. Y. Song, E. C. Burdette, and P. Kazanzides, "Robotic assistance for ultrasound guided prostate brachytherapy," *Medical Image Analysis*, article in press.

[42] K. Cleary, A. Melzer, V. Watson, G. Kronreif, and D. Stoianovici, "Interventional robotic systems: Applications and technology state-of-the-art," *Minimally Invasive Therapy and Allied Technologies*, vol. 15, no. 2, pp. 101–113, 2006.

[43] W. Hara, S. G. Soltys, and I. C. Gibbs, "CyberKnife®robotic radiosurgery system for tumor treatment," *Expert Review of Anticancer Therapy*, vol. 7, no. 11, pp. 1507–1515, 2007.

[44] F. A. Jolesz and N. McDannold, "Current status and future potential of MRI-guided focused ultrasound surgery," *Journal of Magnetic Resonance Imaging*, vol. 27, no. 2, pp. 391–399, 2008.

[45] A. Krieger, R. C. Susil, C. Mï¿½nard, J. A. Coleman, G. Fichtinger, E. Atalar, and L. L. Whitcomb, "Design of a novel MRI compatible manipulator for image guided prostate interventions," *IEEE Transactions on Biomedical Engineering*, vol. 52, no. 2, pp. 306–313, 2005.

[46] S. Xu, J. Kruecker, P. Guion, N. Glossop, Z. Neeman, P. Choyke, A. K. Singh, and B. J. Wood, "Closed-loop control in fused MR-TRUS image-guided prostate biopsy." *Medical image computing and computer-assisted*

intervention : MICCAI International Conference on Medical Image Computing and Computer-Assisted Intervention, vol. 10, no. Pt 1, pp. 128–135, 2007.

[47] E. Watanabe, T. Watanabe, and S. Manaka, "Three-dimensional digitizer (neuronavigator): New equipment for computed tomography-guided stereotaxic surgery," *Surgical neurology*, vol. 27, no. 6, pp. 543–547, 1987.

[48] Y. S. Kwoh, J. Hou, E. A. Jonckheere, and S. Hayati, "A robot with improved absolute positioning accuracy for CT guided stereotactic brain surgery," *IEEE Transactions on Biomedical Engineering*, vol. 35, no. 2, pp. 153–160, 1988.

[49] T. M. Qiu, Y. Zhang, J. S. Wu, W. J. Tang, Y. Zhao, Z. G. Pan, Y. Mao, and L. F. Zhou, "Virtual reality presurgical planning for cerebral gliomas adjacent to motor pathways in an integrated 3-D stereoscopic visualization of structural MRI and DTI tractography," *Acta Neurochirurgica*, vol. 152, no. 11, pp. 1847–1857, 2010.

[50] D. P. Mo, S. D. Bao, L. Li, Z. Q. Yi, J. Y. Zhang, and Y. Zhang, "Virtual reality system for diagnosis and therapeutic planning of cerebral aneurysms," *Chinese medical journal*, vol. 123, no. 16, pp. 2206–2210, 2010.

[51] R. H. Taylor, B. D. Mittelstadt, H. A. Paul, W. Hanson, P. Kazanzides, J. F. Zuhars, B. Williamson, B. L. Musits, E. Glassman, and W. L. Bargar, "Image-directed robotic system for precise orthopaedic surgery," *IEEE Transactions on Robotics and Automation*, vol. 10, no. 3, pp. 261–275, 1994.

[52] J. Fornaro, M. Keel, M. Harders, B. Marincek, G. Szï¿½kely, and T. Frauenfelder, "An interactive surgical planning tool for acetabular fractures: Initial results," *Journal of Orthopaedic Surgery and Research*, vol. 5, no. 1, 2010.

[53] M. Jakopec, S. J. Harris, F. R. y Baena, P. Gomes, J. Cobb, and B. L. Davies, "The first clinical application of a "hands-on" robotic knee surgery system," *Computer Aided Surgery*, vol. 6, no. 6, pp. 329–339, 2001.

[54] Y. S. N. Jayaratne, R. A. Zwahlen, J. Lo, S. C. Tam, and L. K. Cheung, "Computer-aided maxillofacial surgery: An update," *Surgical Innovation*, vol. 17, no. 3, pp. 217–225, 2010.

[55] C. Rickers, R. Gallegos, R. Seethamraju, X. Wang, C. Swingen, A. Jayaswal, E. P. Rahrmann, Z. J. Kastenberg, C. E. Clarkson, R. Bianco, T. O'Brian, C. Verfaillie, R. M. B. III, N. Wilke, and M. Jerosch-Herold, "Applications of magnetic resonance imaging for cardiac stem cell therapy," *Journal of interventional cardiology*, vol. 17, no. 1, pp. 37–46, 2004.

[56] M. Rodriguez-Porcel, O. Gheysens, I. Y. Chen, J. C. Wu, and S. S. Gambhir, "Image-guided cardiac cell delivery using high-resolution small-animal ultrasound," *Molecular Therapy*, vol. 12, no. 6, pp. 1142–1147, 2005.

[57] M. E. Rettmann, D. R. Holmes III, B. M. Cameron, and R. A. Robb, "An event-driven distributed processing architecture for image-guided cardiac ablation therapy," *Computer methods and programs in biomedicine*, vol. 95, no. 2, pp. 95–104, 2009.

[58] K. Wilson, G. Guiraudon, D. L. Jones, and T. M. Peters, "Mapping of cardiac electrophysiology onto a dynamic patient-specific heart model," *IEEE Transactions on Medical Imaging*, vol. 28, no. 12, pp. 1870–1880, 2009.

[59] V. Falk, S. Jacobs, J. F. Gummert, T. Walther, and F. W. Mohr, "Computer-enhanced endoscopic coronary artery bypass grafting: The da Vinci experience," *Seminars in thoracic and cardiovascular surgery*, vol. 15, no. 2, pp. 104–111, 2003.

[60] G. P. Mylonas, A. Darzi, and G. Z. Yang, "Gaze-contingent control for minimally invasive robotic surgery," *Computer Aided Surgery*, vol. 11, no. 5, pp. 256–266, 2006.

[61] N. V. Vasilyev, J. F. Martinez, F. P. Freudenthal, Y. Suematsu, G. R. Marx, and P. J. del Nido, "Three-dimensional echo and videocardioscopy-guided atrial septal defect closure," *Annals of Thoracic Surgery*, vol. 82, no. 4, pp. 1322–1326, 2006.

[62] C. A. Linte, M. Wierzbicki, J. Moore, S. H. Little, G. M. Guiraudon, and T. M. Peters, "Towards subject-specific models of the dynamic heart for image-guided mitral valve surgery." *Medical image computing and computer-assisted intervention : MICCAI International Conference on Medical Image Computing and Computer-Assisted Intervention*, vol. 10, no. Pt 2, pp. 94–101, 2007.

[63] S. G. Yuen, S. B. Kesner, N. V. Vasilyev, P. J. D. Nido, and R. D. Howe, "3D ultrasound-guided motion compensation system for beating heart mitral valve repair." *Medical image computing and computer-assisted intervention : MICCAI International Conference on Medical Image Computing and Computer-Assisted Intervention*, vol. 11, no. 1, pp. 711–719, 2008.

[64] S. Birring, C. Brightling, P. Bradding, J. J. Entwisle, D. D. Vara, J. Grigg, A. J. Wardlaw, and I. D. Pavord, "Clinical, radiologic, and induced sputum features of chronic obstructive pulmonary disease in nonsmokers: A descriptive study," *American Journal of Respiratory and Critical Care Medicine*, vol. 166, no. 8, pp. 1078–1083, 2002.

[65] K. F. Rabe, S. Hurd, A. Anzueto, P. J. Barnes, S. A. Buist, P. Calverley, Y. Fukuchi, C. Jenkins, R. Rodriguez-Roisin, C. V. Weel, and J. Zielinski, "Global strategy for the diagnosis, management, and prevention of chronic obstructive pulmonary disease: GOLD executive summary," *American Journal of Respiratory and Critical Care Medicine*, vol. 176, no. 6, pp. 532–555, 2007.

[66] J. W. Gurney, "Pathophysiology of obstructive airways disease," *Radiologic clinics of North America*, vol. 36, no. 1, pp. 15–27, 1998.

[67] H. O. Coxson and R. M. Rogers, "Quantitative computed tomography of chronic obstructive pulmonary disease," *Academic Radiology*, vol. 12, no. 11, pp. 1457–1463, 2005.

[68] J. Reilly, "Using computed tomographic scanning to advance understanding of chronic obstructive pulmonary disease," *Proceedings of the American Thoracic Society*, vol. 3, no. 5, pp. 450–455, 2006.

[69] N. L. Muller, C. A. Staples, R. R. Miller, and R. T. Abboud, "'Density mask'. An objective method to quantitate emphysema using computed tomography," *Chest*, vol. 94, no. 4, pp. 782–787, 1988.

[70] B. van Ginneken, L. Hogeweg, and M. Prokop, "Computer-aided diagnosis in chest radiography: Beyond nodules," *European Journal of Radiology*, vol. 72, no. 2, pp. 226–230, 2009.

[71] E. Cavigli, G. Camiciottoli, S. Diciotti, I. Orlandi, C. Spinelli, E. Meoni, L. Grassi, C. Farfalla, M. Pistolesi, F. Falaschi, and M. Mascalchi, "Whole-lung densitometry versus visual assessment of emphysema," *European radiology*, vol. 19, no. 7, pp. 1686–1692, 2009.

[72] T. Stavngaard, S. B. Shaker, K. S. Bach, B. C. Stoel, and A. Dirksen, "Quantitative assessment of regional emphysema distribution in patients with Chronic Obstructive Pulmonary Disease (COPD)," *Acta radiologica*, vol. 47, no. 9, pp. 914–921, 2006.

[73] R. Uppaluri, T. Mitsa, M. Sonka, E. A. Hoffman, and G. McLennan, "Quantification of pulmonary emphysema from lung computed tomography images," *American Journal of Respiratory and Critical Care Medicine*, vol. 156, no. 1, pp. 248–254, 1997.

[74] R. Uppaluri, E. A. Hoffman, M. Sonka, P. G. Hartley, G. W. Hunninghake, and G. McLennan, "Computer recognition of regional lung disease patterns," *American Journal of Respiratory and Critical Care Medicine*, vol. 160, no. 2, pp. 648–654, 1999.

[75] O. Friman, M. Borga, M. Lundberg, U. Tylen, and H. Knutsson, "Recognizing emphysema - a neural network approach," *Proceedings - International Conference on Pattern Recognition*, vol. 16, no. 1, pp. 512–515, 2002.

[76] F. Chabat, G.-Z. Yang, and D. M. Hansell, "Obstructive lung diseases: Texture classification for differentiation at CT," *Radiology*, vol. 228, no. 3, pp. 871–877, 2003.

[77] I. C. Sluimer, P. F. V. Waes, M. A. Viergever, and B. V. Ginneken, "Computer-aided diagnosis in high resolution CT of the lungs," *Medical physics*, vol. 30, no. 12, pp. 3081–3090, 2003.

[78] I. C. Sluimer, M. Prokop, I. Hartmann, and B. V. Ginneken, "Automated classification of hyperlucency, fibrosis, ground glass, solid, and focal lesions in high-resolution CT of the lung," *Medical physics*, vol. 33, no. 7, pp. 2610–2620, 2006.

[79] Y. Xu, M. Sonka, G. McLennan, J. Guo, and E. A. Huffman, "MDCT-based 3-D texture classification of emphysema and early smoking related lung pathologies," *IEEE Transactions on Medical Imaging*, vol. 25, no. 4, pp. 464–475, 2006.

[80] A. Depeursinge, D. Sage, A. Hidki, A. Platon, P. A. Poletti, M. Unser, and H. Muller, "Lung tissue classification using wavelet frames," 2007, pp. 6259–6262.

[81] Y. S. Park, J. B. Seo, N. Kim, E. J. Chae, Y. M. Oh, S. D. Lee, Y. Lee, and S. H. Kang, "Texture-based quantification of pulmonary emphysema on high-resolution computed tomography: Comparison with density-based quantification and correlation with pulmonary function test," *Investigative radiology*, vol. 43, no. 6, pp. 395–402, 2008.

[82] M. Prasad, A. Sowmya, and I. Koch, "Designing relevant features for continuous data sets using ICA," *International Journal of Computational Intelligence and Applications*, vol. 7, no. 4, pp. 447–468, 2008.

[83] M. Prasad, A. Sowmya, and P. Wilson, "Multi-level classification of emphysema in HRCT lung images," *Pattern Analysis and Applications*, vol. 12, no. 1, pp. 9–20, 2009.

[84] L. Sørensen, S. B. Shaker, and M. D. Bruijne, "Quantitative analysis of pulmonary emphysema using local binary patterns," *IEEE Transactions on Medical Imaging*, vol. 29, no. 2, pp. 559–569, 2010.

[85] W. R. Webb, N. L. Muller, and D. P. Naidich, *High-Resolution CT of the Lung*, 3rd ed., J.-R. John, Ed. Baltimore, MD: Lippincott Williams & Wilkins, 2001.

[86] W. R. Webb, "Thin-section CT of the secondary pulmonary lobule: Anatomy and the image– The 2004 Fleischner Lecture," *Radiology*, vol. 239, no. 2, pp. 322–338, 2006.

[87] R. M. Haralick, "Statistical and structural approaches to texture." *Proceedings IEEE*, vol. 67, no. 5, pp. 786–804, 1979.

[88] T. Ojala, M. Pietikäinen, and D. Harwood, "A comparative study of texture measures with classification based on feature distributions," *Pattern Recognition*, vol. 29, no. 1, pp. 51–59, 1996.

[89] T. Ojala, M. Pietikäinen, and T. Mäenpää, "Multiresolution gray-scale and rotation invariant texture classification with local binary patterns," *IEEE Transactions on Pattern Analysis and Machine Intelligence*, vol. 24, no. 7, pp. 971–987, 2002.

[90] R. G. Keys, "Cubic convolution interpolation for digital image processing." *IEEE Transactions on Acoustics, Speech, and Signal Processing*, vol. ASSP-29, no. 6, pp. 1153–1160, 1981.

[91] X. Tan and B. Triggs, "Enhanced local texture feature sets for face recognition under difficult lighting conditions," *IEEE Transactions on Image Processing*, vol. 19, no. 6, pp. 1635–1650, 2010.

[92] Z. I. Botev, J. F. Grotowski, and D. P. Kroese, "Kernel density estimation via diffusion," *Annals of Statistics*, vol. 35, no. 5, pp. 2916–2957, 2010.

[93] S. H. Cha and S. N. Srihari, "On measuring the distance between histograms," *Pattern Recognition*, vol. 35, no. 6, pp. 1355–1370, 2002.

[94] Y. Rubner, C. Tomasi, and L. J. Guibas, "Earth mover's distance as a metric for image retrieval," *International Journal of Computer Vision*, vol. 40, no. 2, pp. 99–121, 2000.

[95] W. Niblack, R. Barber, W. Equitz, M. D. Flickner, E. H. Glasman, D. Petkovic, P. Yanker, C. Faloutsos, and G. Taubin, "QBIC project: querying images by content, using color, texture, and shape," in *Storage and Retrieval for Image and Video Databases*, vol. 1908, 1993, pp. 173–187.

[96] H. Ling and K. Okada, "Diffusion distance for histogram comparison," in *2006 IEEE Computer Society Conference on Computer Vision and Pattern Recognition, CVPR 2006*, vol. 1, 2006, pp. 246–253.

[97] H. C. Shen and A. K. C. Wong, "Generalized texture representation and metric," *Computer Vision, Graphics and Image Processing*, vol. 23, no. 2, pp. 187–206, 1983.

[98] A. K. Jain, R. P. W. Duin, and J. Mao, "Statistical pattern recognition: A review," *IEEE Transactions on Pattern Analysis and Machine Intelligence*, vol. 22, no. 1, pp. 4–37, 2000.

[99] S. Hu, E. A. Hoffman, and J. M. Reinhardt, "Automatic lung segmentation for accurate quantitation of volumetric X-ray CT images," *IEEE Transactions on Medical Imaging*, vol. 20, no. 6, pp. 490–498, 2001.

[100] M. Kass, A. Witkin, and D. Terzopoulos, "Snakes: Active contour models," *International Journal of Computer Vision*, vol. 1, no. 4, pp. 321–331, 1988.

[101] C. Xu and J. L. Prince, "Snakes, shapes, and gradient vector flow," *IEEE Transactions on Image Processing*, vol. 7, no. 3, pp. 359–369, 1998.

[102] L. D. Cohen, "On active contour models and balloons," *CVGIP: Image Understanding*, vol. 53, no. 2, pp. 211–218, 1991.

[103] S. Kichenassamy, A. Kumar, P. Olver, A. Tannenbaum, and A. Yezzi, "Gradient flows and geometric active contour models," in *IEEE International Conference on Computer Vision*, 1995, pp. 810–815.

[104] R. Malladi, J. A. Sethian, and B. C. Vemuri, "Shape modeling with front propagation: A level set approach," *IEEE Transactions on Pattern Analysis and Machine Intelligence*, vol. 17, pp. 158–175, 1995.

[105] V. Caselles, R. Kimmel, and G. Sapiro, "Geodesic active contours," *International Journal of Computer Vision*, vol. 22, pp. 61–79, 1997.

[106] N. Paragios and R. Deriche, "Unifying boundary and region-based information for geodesic active tracking," *IEEE Computer Society Conference on Computer Vision and Pattern Recognition*, vol. 2, pp. 422–427, 1999.

[107] L. Cohen, E. Bardinet, and N. Ayache, "Surface reconstruction using active contour models," *SPIE Conference on Geometric Methods in Computer Vision*, 1993.

[108] O. Ecabert and J. P. Thiran, "Variational image segmentation by unifying region and boundary information," in *16th International Conference on Pattern Recognition*, vol. 16, 2002, pp. 885–888.

[109] S. J. Besson, M. Barlaud, and G. Aubert, "Detection and tracking of moving objects using a new level set based method," *International Conference on Pattern Recognition*, 2000.

[110] S. C. Zhu, "Region competition: Unifying snakes, region growing, and bayes/mdl for multiband image segmentation," *IEEE Transactions on Pattern Analysis and Machine Intelligence*, vol. 18, no. 9, pp. 884–900, 1996, cited By (since 1996): 786.

[111] G. Aubert, M. Barlaud, O. Faugeras, and S. Jehan-Besson, "Image segmentation using active contours: Calculus of variations or shape gradients?" *SIAM Journal on Applied Mathematics*, vol. 63, no. 6, pp. 2128–2154, 2003.

[112] S. Jehan-Besson, M. Barland, and G. Aubert, "DREAM2S: Deformable regions driven by an eulerian accurate minimization method for image and video segmentation," *International Journal of Computer Vision*, vol. 53, no. 1, pp. 45–70, 2003.

[113] T. Roy, E. Debreuve, M. Barlaud, and G. Aubert, "Segmentation of a vector field: Dominant parameter and shape optimization," *Journal of Mathematical Imaging and Vision*, vol. 24, no. 2, pp. 259–276, 2006.

[114] T. Roy, M. Barlaud, E. Debreuve, and G. Aubert, "Vector field segmentation using active contours: Regions of vectors with the same direction," *Workshop on Variational, Geometric, and Level Set Methods in Computer Vision (VLSM)*, 2003.

[115] N. Paragios, "Geodesic active contours and level sets for the detection and tracking of moving objects," *IEEE Transactions on Pattern Analysis and Machine Intelligence*, vol. 22, no. 3, pp. 266–280, 2000.

[116] T. Brox, M. Rousson, R. Deriche, and J. Weickert, "Unsupervised segmentation incorporating colour, texture and motion," *Computer Analysis of Images and Patterns – Lecture Notes Computer Science*, 2003.

[117] N. Paragios and R. Deriche, "Geodesic active contours for supervised texture segmentation," *Proceedings of IEEE International Conference on Computer Vision and Pattern Recognition*, pp. 2422–2427, 1999.

[118] T. Brox and J. Weickert, "A TV flow based local scale measure for texture discrimination," *Proceedings of ECCV*, vol. 2, pp. 578–590, 2004.

[119] M. Rousson, T. Brox, and R. Deriche, "Active unsupervised texture segmentation on a diffusion based feature space," *IEEE Conference on Computer Vision and Pattern Recognition*, pp. 699–704, 2003.

[120] D. Cremers, F. Tischhäuser, J. Weickert, and C. Schnörr, "Diffusion snakes: Introducing statistical shape knowledge into the Mumford-Shah functional," *International Journal of Computer Vision*, vol. 50, no. 3, pp. 295–313, 2002.

[121] M. Gastaud, M. Barlaud, and G. Aubert, "Combining shape prior and statistical features for active contour segmentation," *IEEE Transactions on Circuits and Systems for Video Technology*, vol. 14, no. 5, pp. 726–734, 2004.

[122] M. Rochery, I. H. Jermyn, and J. Zerubia, "Higher order active contours," *International Journal of Computer Vision*, vol. 69, no. 1, pp. 27–42, 2006.

[123] N. Paragios and R. Deriche, "Geodesic active regions: A new framework to deal with frame partition problems in computer vision," *Journal of Visual Communication and Image Representation*, vol. 13, no. 1-2, pp. 249–268, 2002.

[124] A. Chakraborty and L. H. Staib, "Deformable boundary finding in medical images by integrating gradient and region information," *IEEE Transactions on Medical Imaging*, vol. 15, no. 6, pp. 859–870, 1996.

[125] T. F. Chan and L. A. Vese, "Active contours without edges," *IEEE Transactions on Image Processing*, vol. 10, no. 2, pp. 266–277, 2001.

[126] T. Chan and L. Vese, "An active contour model without edges," *International Conference of Scale-Space Theories in Computer Vision*, pp. 141–151, 1999.

[127] C. Chesnaud, P. Rélrégier, and V. Boulet, "Statistical region snake-based segmentation adapted to different physical noise models," *IEEE Transactions on Pattern Analysis and Machine Intelligence*, vol. 21, no. 11, pp. 1145–1157, 1999.

[128] T. Brox and J. Weickert, "Level set based image segmentation with multiple regions," *Springer Lecture Notes on Computer Science*, p. 3175, 2004.

[129] D. Freedman and T. Zhang, "Active contours for tracking distributions," *IEEE Transactions on Image Processing*, vol. 13, no. 4, pp. 518–526, 2004.

[130] Y. Rubner, J. Puzicha, C. Tomasi, and J. M. Buhmann, "Empirical evaluation of dissimilarity measures for color and texture," *Computer Vision and Image Understanding*, vol. 84, no. 1, pp. 25–43, 2001.

[131] F. L. Hitchcock, "The distribution of a product from several sources to numerous localities," *Journal of Mathematics and Physics*, vol. 20, pp. 224–230, 1941.

[132] O. Michailovich, Y. Rathi, and A. Tannenbaum, "Image segmentation using active contours driven by the Bhattacharyya gradient flow," *IEEE Transactions on Image Processing*, vol. 16, no. 11, pp. 2787–2801, 2007.

[133] K. Ni, X. Bresson, T. Chan, and S. Esedoglu, "Local histogram based segmentation using the Wasserstein distance," *International Journal of Computer Vision*, vol. 84, no. 1, pp. 97–111, 2009.

[134] A. Adam, R. Kimmel, and E. Rivlin, "On scene segmentation and histograms-based curve evolution," *IEEE Transactions on Pattern Analysis and Machine Intelligence*, vol. 31, no. 9, pp. 1708–1714, 2009.

[135] Q. Zhao, Z. Yang, and H. Tao, "Differential earth mover's distance with its applications to visual tracking," *IEEE Transactions on Pattern Analysis and Machine Intelligence*, vol. 32, no. 2, pp. 274–287, 2010.

[136] F. Serratosa and A. Sanfeliu, "Signatures versus histograms: Definitions, distances and algorithms," *Pattern Recognition*, vol. 39, no. 5, pp. 921–934, 2006.

[137] D. Mumford and J. Shah, "Boundary detection by minimizing functionals I," in *IEEE Conference on Computer Vision and Pattern Recognition*, 1985.

[138] R. Ronfard, "Region-based strategies for active contour models," *International Journal of Computer Vision*, vol. 13, no. 2, pp. 229–251, 1994.

[139] P. Brigger, J. Hoeg, and M. Unser, "B-spline snakes: A flexible tool for parametric contour detection," *IEEE Transactions on Image Processing*, vol. 9, no. 9, pp. 1484–1496, 2000.

[140] S. Osher and J. A. Sethian, "Fronts propagating with curvature-dependent speed: Algorithms based on Hamilton-Jacobi formulations," *Journal of Computational Physics*, vol. 79, no. 1, pp. 12–49, 1988.

[141] G. Dantzig, *Linear Programming and Extensions.* Princeton University Press, Princeton, 1963.

[142] R. W. Hunt, *Measuring Color*, 3rd ed. Fountain Press, England, 1998.

[143] M. D. Fairchild, *Color Appearance Models*, 2nd ed. Wiley-IS&T, Chichester, UK, 2005.

[144] *Specification ICC.1:2004-10 (Profile version 4.2.0.0) Image technology colour management - Architecture, profile format, and data structure*, International Color Consortium, 2006.

[145] S. P. Lloyd, "Least squares quantization in PCM," *IEEE Transactions on Information Theory*, vol. 28, pp. 129–137, 1982.

[146] Y. Shi and W. Karl, "A fast level set method without solving PDEs," *Proceedings of IEEE International Conference on Acoustics, Speech, and Signal Processing*, 2005.

[147] Y. Shi and W. C. Karl, "A real-time algorithm for the approximation of level-set-based curve evolution," *IEEE Transactions on Image Processing*, vol. 17, no. 5, pp. 645–656, 2008.

[148] J. Malcolm, Y. Rathi, A. Yezzi, and A. Tannenbaum, "Fast approximate surface evolution in arbitrary dimension," in *Proceedings of SPIE - The International Society for Optical Engineering*, vol. 6914, 2008.

[149] B. Merriman, "Motion of multiple junctions: A level set approach," *Journal of Computational Physics*, vol. 112, no. 2, pp. 334–363, 1994.

[150] W. Stolz, O. Braun-Falco, P. Bilek, M. Landthaler, W. H. C. Burgdorf, and A. B. Cognetta, *Color Atlas of Dermatoscopy.* Blackwell Wissenschafts-Verlag, Berlin, 2002.

[151] K. Westerhoff, W. H. McCarthy, and S. W. Menzies, "Increase in the sensitivity for melanoma diagnosis by primary care physicians using skin surface microscopy," *British Journal of Dermatology*, vol. 143, no. 5, pp. 1016–1020, 2000.

[152] M. Binder, H. Kittler, A. Seeber, A. Steiner, H. Pehamberger, and K. Wolff, "Epiluminescence microscopy-based classification of pigmented skin lesions using computerized image analysis and an artificial neural network," *Melanoma research*, vol. 8, no. 3, pp. 261–266, 1998.

[153] P. Schmidt, "Segmentation of digitized dermatoscopic images by two-dimensional color clustering," *IEEE Transactions on Medical Imaging*, vol. 18, no. 2, pp. 164–171, 1999.

[154] P. Schmid-Saugeon, J. Guillod, and J. P. Thiran, "Towards a computer-aided diagnosis system for pigmented skin lesions," *Computerized Medical Imaging and Graphics*, vol. 27, no. 1, pp. 65–78, 2003.

[155] W. V. Stoecker, W. W. Li, and R. H. Moss, "Automatic detection of asymmetry in skin tumors," *Computerized Medical Imaging and Graphics*, vol. 16, no. 3, pp. 191–197, 1992.

[156] B. Erkol, R. H. Moss, R. J. Stanley, W. V. Stoecker, and E. Hvatum, "Automatic lesion boundary detection in dermoscopy images using gradient vector flow snakes," *Skin Research and Technology*, vol. 11, no. 1, pp. 17–26, 2005.

[157] T. K. Lee and E. Claridge, "Predictive power of irregular border shapes for malignant melanomas," *Skin Research and Technology*, vol. 11, no. 1, pp. 1–8, 2005.

[158] C. Grana, G. Pellacani, R. Cucchiara, and S. Seidenari, "A new algorithm for border description of polarized light surface microscopic images of pigmented skin lesions," *IEEE Transactions on Medical Imaging*, vol. 22, no. 8, pp. 959–964, 2003.

[159] J. E. Golston, R. H. Moss, and W. V. Stoecker, "Boundary detection in skin tumor images: An overall approach and a radial search algorithm," *Pattern Recognition*, vol. 23, no. 11, pp. 1235–1247, 1990.

[160] R. J. Stanley, R. H. Moss, W. V. Stoecker, and C. Aggawal, "A fuzzy-based histogram analysis technique for skin lesion discrimination in dermatology clinical images," *Computerized Medical Imaging and Graphics*, vol. 27, no. 5, pp. 387–396, 2003.

[161] T. Tommasi, E. L. Torre, and B. Caputo, "Melanoma recognition using representative and discriminative kernel classifiers," in *Springer Lecture Notes in Computer Science*, vol. 4241, 2006, pp. 1–12.

[162] T. Tanaka, S. Torii, I. Kabuta, K. Shimizu, and M. Tanaka, "Pattern classification of nevus with texture analysis," *IEEJ Transactions on Electrical and Electronic Engineering*, vol. 3, no. 1, pp. 143–150, 2008.

[163] M. Tanaka, "Dermoscopy," *The Journal of Dermatology*, vol. 33, no. 8, pp. 513–517, 2006.

[164] G. Argenziano, H. Soyer, S. Chimenti, R. Talamini, R. Corona, F. Sera, M. Binder, L. Cerroni, G. De Rosa, G. Ferrara, R. Hofmann-Wellenhof, M. Landthaler, S. Menzies, H. Pehamberger, D. Piccolo, H. Rabinovitz, R. Schiffner, S. Staibano, W. Stolz, I. Bartenjev, A. Blum, R. Braun, H. Cabo, P. Carli, V. De Giorgi, M. Fleming, J. Grichnik, C. Grin, A. Halpern, R. Johr, B. Katz, R. Kenet, H. Kittler, J. Kreusch, J. Malvehy, G. Mazzocchetti, M. Oliviero, F. Özdemir, K. Peris, R. Perotti, A. Perusquia, M. Pizzichetta, S. Puig, B. Rao, P. Rubegni, T. Saida, M. Scalvenzi, S. Seidenari, I. Stanganelli, M. Tanaka, K. Westerhoff, I. Wolf, O. Braun-Falco, H. Kerl, T. Nishikawa, K. Wolff, and A. Kopf, "Dermoscopy of pigmented skin lesions: Results of a consensus meeting via the internet," *Journal of the American Academy of Dermatology*, vol. 48, no. 5, pp. 679–693, 2003.

[165] C. Serrano and B. Acha, "Pattern analysis of dermoscopic images based on Markov random fields," *Pattern Recognition*, vol. 42, no. 6, pp. 1052–1057, 2009.

[166] D. Panjwani and G. Healey, "Results using random field models for the segmentation of color images of natural scenes," in *IEEE International Conference on Computer Vision*, 1995, pp. 714–719.

[167] Z. Kato and T. C. Pong, "A Markov random field image segmentation model for color textured images," *Image and Vision Computing*, vol. 24, no. 10, pp. 1103–1114, 2006.

[168] F. A. Tab, G. Naghdy, and A. Mertins, "Scalable multiresolution color image segmentation," *Signal Processing*, vol. 86, no. 7, pp. 1670–1687, 2006.

[169] J. Gao, J. Zhang, M. G. Fleming, I. Pollak, and A. B. Cognetta, "Segmentation of dermatoscopic images by stabilized inverse diffusion equations," in *IEEE International Conference on Image Processing*, vol. 3, 1998, pp. 823–827.

[170] S. Z. Li, *Markov Random Field Modeling in Image Analysis*. Springer-Verlag, Tokyo, 2001.

[171] Y. Xia, D. Feng, and R. Zhao, "Adaptive segmentation of textured images by using the coupled Markov random field model," *IEEE Transactions on Image Processing*, vol. 15, no. 11, pp. 3559–3566, 2006.

[172] R. L. Kashyap and R. Chellappa, "Estimation and choice of neighbors in spatial-interaction models of images." *IEEE Transactions on Information Theory*, vol. IT-29, no. 1, pp. 60–72, 1983.

[173] B. S. Manjunath, T. Simchony, and R. Chellappa, "Stochastic and deterministic networks for texture segmentation," *IEEE Transactions on Acoustics, Speech, and Signal Processing*, vol. 38, no. 6, pp. 1039–1049, 1990.

[174] B. S. Manjunath and R. Chellappa, "Unsupervised texture segmentation using Markov random field models," *IEEE Transactions on Pattern Analysis and Machine Intelligence*, vol. 13, no. 5, pp. 478–482, 1991.

[175] Y. Chen and P. Hao, "Optimal transform in perceptually uniform color space and its application in image retrieval," in *International Conference on Signal Processing Proceedings, ICSP*, vol. 2, 2004, pp. 1107–1110.

[176] B. Reitinger, A. Bornik, R. Beichel, and D. Schmalstieg, "Liver surgery planning using virtual reality," *IEEE Computer Graphics and Applications*, vol. 26, no. 6, pp. 36–47, 2006.

[177] C. Suárez, B. Acha, C. Serrano, C. Parra, and T. Gómez, "Virsspa- a virtual reality tool for surgical planning workflow," *International Journal of Computer Assisted Radiology and Surgery*, vol. 4, no. 2, pp. 133–139, 2009.

[178] S. W. Zucker, "Region growing: Childhood and adolescence," *Computer Graphics and Image Processing*, vol. 5, no. 3, pp. 382–399, 1976.

[179] G. J. Sivewright and P. J. Elliott, "Interactive region and volume growing for segmenting volumes in MR and CT images," *Medical Informatics*, vol. 19, no. 1, pp. 71–80, 1994.

[180] H. Sekiguchi, K. Sano, and T. Yokoyama, "Interactive 3-dimensional segmentation method based on region growing method," *Systems and Computers in Japan*, vol. 25, no. 1, pp. 88–97, 1994.

[181] X. Zhou, N. Kamiya, T. Kara, H. Fujita, R. Yokoyama, T. Kiryu, and H. Hoshi, "Automated recognition of human strucure from torso CT images," in *Proceedings of the Fourth IASTED International Conference on Visualization, Imaging, and Image Processing*, 2004, pp. 584–589.

[182] T. Y. Law and P. A. Heng, "Automated extraction of bronchus from 3D CT images of lung based on genetic algorithm and 3D region growing," in *Proceedings of SPIE - The International Society for Optical Engineering*, vol. 3979, 2000, pp. 906–916.

[183] R. Adams and L. Bischof, "Seeded region growing," vol. 16, no. 6, pp. 641–647, 1994.

[184] J. Dehmeshki, H. Amin, M. Valdivieso, and X. Ye, "Segmentation of pulmonary nodules in thoracic CT scans: A region growing approach," *IEEE Transactions on Medical Imaging*, vol. 27, no. 4, pp. 467–480, 2008.

[185] S. A. Hojjatoleslami and J. Kittler, "Region growing: A new approach," *IEEE Transactions on Image Processing*, vol. 7, no. 7, pp. 1079–1084, 1998.

[186] R. M. Haralick and L. G. Shapiro, "Image segmentation techniques," *Computer Vision, Graphics, & Image Processing*, vol. 29, no. 1, pp. 100–132, 1985.

[187] C. Revol-Muller, F. Peyrin, Y. Carrillon, and C. Odet, "Automated 3D region growing algorithm based on an assessment function," *Pattern Recognition Letters*, vol. 23, no. 1-3, pp. 137–150, 2002.

[188] J. K. Udupa and S. Samarasekera, "Fuzzy connectedness and object definition: Theory, algorithms, and applications in image segmentation," *Graphical Models and Image Processing*, vol. 58, no. 3, pp. 246–261, 1996.

[189] J. K. Udupa, "Multiple sclerosis lesion quantification using fuzzy-connectedness principles," *IEEE Transactions on Medical Imaging*, vol. 16, no. 5, pp. 598–609, 1997.

[190] P. K. Saha, J. K. Udupa, E. F. Conant, D. P. Chakraborty, and D. Sullivan, "Breast tissue density quantification via digitized mammograms," *IEEE Transactions on Medical Imaging*, vol. 20, no. 8, pp. 792–803, 2001.

[191] S. Luo, X. Li, and G. Zhou, "A simplified fuzzy connectedness method used for segmentation of vessel images," in *Annual International Conference of the IEEE Engineering in Medicine and Biology - Proceedings*, vol. 1, 2003, pp. 751–753.

[192] J. Tschirren, E. A. Huffman, G. McLennan, and M. Sonka, "Intrathoracic airway trees: Segmentation and airway morphology analysis from low-dose CT scans," *IEEE Transactions on Medical Imaging*, vol. 24, no. 12, pp. 1529–1539, 2005.

[193] J. K. Udupa, P. K. Saha, and R. A. Lotufo, "Relative fuzzy connectedness and object definition: Theory, algorithms, and applications in image segmentation," *IEEE Transactions on Pattern Analysis and Machine Intelligence*, vol. 24, no. 11, pp. 1485–1500, 2002.

[194] W. Jian, Y. Feng, J. L. Ma, X. P. Sun, X. Jing, and Z. M. Cui, "The segmentation and visualization of human organs based on adaptive region growing method," in *Proceedings - 8th IEEE International Conference on Computer and Information Technology Workshops, CIT Workshops 2008*, 2008, pp. 439–443.

[195] T. S. Yoo, M. J. Ackerman, W. E. Lorensen, W. Schroeder, V. Chalana, S. Aylward, D. Metaxas, and R. Whitaker, "Engineering and algorithm design for an image processing API: a technical report on ITK–the Insight Toolkit." *Studies in health technology and informatics*, vol. 85, pp. 586–592, 2002.

[196] S. Pieper, B. Lorensen, W. Schroeder, and R. Kikinis, "The NA-MIC Kit: ITK, VTK, pipelines, grids and 3D Slicer as an open platform for the medical image computing community," in *2006 3rd IEEE International Symposium on Biomedical Imaging: From Nano to Macro - Proceedings*, vol. 2006, 2006, pp. 698–701.

[197] J. K. Udupa, V. R. LeBlanc, Y. Zhuge, C. Imielinska, H. Schmidt, L. M. Currie, B. E. Hirsch, and J. Woodburn, "A framework for evaluating image segmentation algorithms," *Computerized Medical Imaging and Graphics*, vol. 30, no. 2, pp. 75–87, 2006.

[198] L. R. Dice, "Measures of the amount of ecologic association between species," *Ecology*, vol. 26, no. 3, pp. 297–302, 1945.

[199] P. Jaccard, "Étude comparative de la distribution florale dans une portion des Alpes et des Jura," *Bulletin del la Société Vaudoise des Sciences Naturelles*, vol. 37, pp. 547–579, 1901.

[200] W. E. Lorensen and H. E. Cline, "Marching cubes: A high resolution 3D surface construction algorithm." *Computer Graphics (ACM)*, vol. 21, no. 4, pp. 163–169, 1987.

[201] P. Gacto-Sánchez, D. Sicilia-Castro, T. Gómez-Cía, A. Lagares, T. Collell, C. Suárez, C. Parra, P. Infante-Cossío, and J. M. De La Higuera, "Use of a three-dimensional virtual reality model for preoperative imaging in DIEP flap breast reconstruction," *Journal of Surgical Research*, vol. 162, no. 1, pp. 140–147, 2010.

[202] P. Gacto-Sánchez, D. Sicilia-Castro, T. Gómez-Cía, A. Lagares, T. Collell, C. Suárez, C. Parra, S. Leal, P. Infante-Cossío, and J. M. De La Higuera, "Computed tomographic angiography with VirSSPA three-dimensional software for perforator navigation improves perioperative outcomes in DIEP flap breast reconstruction," *Plastic and Reconstructive Surgery*, vol. 125, no. 1, pp. 24–31, 2010.

[203] T. Gómez-Cía, P. Gacto-Sánchez, D. Sicilia, C. Suárez, B. Acha, C. Serrano, C. Parra, and J. Higuera, "The virtual reality tool VirSSPA in planning DIEP microsurgical breast reconstruction," *International Journal of Computer Assisted Radiology and Surgery*, vol. 4, no. 4, pp. 375–382, 2009.